Structural characterization of Ni-containing metalloenzymes from archaea by X-ray crystallography and transmission electron microscopy

D i s s e r t a t i o n

zur Erlangung des akademischen Grades

d o c t o r r e r u m n a t u r a l i u m

(Dr. rer. nat.)

im Fach Biologie

eingereicht an der Lebenswissenschaftlichen Fakultät der

Humboldt-Universität zu Berlin

von

Diplom-Biochemikerin Yulia Ilina

Präsidentin der Humboldt-Universität zu Berlin
Prof. Dr.-Ing. Dr. Sabine Kunst

Dekan der Lebenswissenschaftlichen Fakultät
Prof. Dr. Bernhard Grimm

Gutachter/innen
1. Prof. Dr. Holger Dobbek
2. Prof. Dr. Peter Hildebrandt
3. Prof. Dr. Petra Wendler

Tag der mündlichen Prüfung: 17.09.2019

ABSTRACT

Metals in biological systems catalyze challenging enzymatic reactions, including bond formation and cleavage, radical chemistry, atom and electron transfer. In this work, two metal-based enzyme systems from archaea, the Ni-containing CO dehydrogenase (CODH) and [NiFe] containing hydrogenase, are structurally characterized.

CODHs catalyze the reversible reduction of CO_2 to CO and in archaea this reaction is coupled to the synthesis and cleavage of acetyl-coenzyme A (acetyl-CoA). The overall reaction is catalyzed by the acetyl-CoA decarbonylase/synthase (ACDS) complex and within the complex, the chemistry of reversible carbon-carbon bond formation is accomplished by coordinated activity of five protein subcomponents, at least 33 iron-sulfur clusters, 6 cobalt- and 12 nickel-containing active sites. Despite extensive biochemical and spectroscopic characterization, as well as X-ray crystal structures of the individual components from archaeal and bacterial homologs, the structure of the intact protein complex is still unknown.

The first part of this work is dedicated to a structural investigation by transmission electron microscopy of the ACDS complex from the hyperthermophilic sulfate reducer *Archaeoglobus fulgidus* (*Af*ACDS). Purified ACDS complex could be visualized as an intact globular protein particle by negative stain and vitrification (cryo) techniques. The three-dimensional reconstruction is determined *de novo* to 29 Å-resolution by single-particle analysis. Three possible positions for the CODH subunit within the ACDS complex are suggested by rigid-body fitting.

In the second part of this study, the X-ray crystal structure of the CODH subunit of the *Af*ACDS complex is determined. The 220 kDa protein is encoded by the *cdhAB* operon, and is composed of α- and ε-subunits that form a heterodimer with ($\alpha_2\varepsilon_2$) stoichiometry (*Af*$\alpha_2\varepsilon_2$). While the overall structure of *Af*$\alpha_2\varepsilon_2$ resembles the previously reported structure of the $\alpha_2\varepsilon_2$-subunit from *Methanosarcina barkeri* (*Mb*$\alpha_2\varepsilon_2$), the naturally-occurring exchange of the Cys to Asp and Glu resulted in a depletion of the bridging iron-sulfur cluster. As revealed by sequence analysis, this structural trait is observed in different phyla of bacteria and archaea, including 31 enzymes encoded by *cdhAB* operons and 14 homologous Ni-CODH enzymes encoded by *cooS* genes. The phylogenetic analysis suggests that the cluster elimination event could result from gene transfer within the evolutionary lineage, horizontal gene transfer or independent Cys exchange. Additionally, the role of the ε-subunit was investigated by kinetics studies. CO-dependent FAD

reduction activity of *Af*$\alpha_2\varepsilon_2$ exhibited Michaelis-Menten type kinetics with k_{cat} of 186 s^{-1} and K_M of 76 µM. Same kinetic type, as well as comparable kinetic constants, was demonstrated for the *Mb*$\alpha_2\varepsilon_2$-subunit. In contrast, the ε-subunit lacking CODH-II from *Carboxydothermus hydrogenoformans* (*Ch*CODH-II) showed linear dependency between CO-dependent FAD reduction activity and flavin concentration. The data suggests that the ε-subunit provides a scaffold for the flavin binding.

The third section is dedicated to the F_{420}-reducing hydrogenase from *M. barkeri* (*Mb*FRH), which belongs to the group 3 [NiFe] hydrogenases and catalyzes the reversible redox reaction between H_2 and coenzyme F_{420}. The structure of *Mb*FRH was solved by X-ray crystallography and is similar to the structure of FRH from *Methanothermobacter marburgensis* (*Mm*FRH), revealing a spherical, dodecameric arrangement of approx. 1.2 MDa. Along with the established electron transfer chain observed in *Mm*FRH, consisting of the [NiFe] active site, four [4Fe4S] clusters and FAD, one solvent-exposed [2Fe2S] cluster is detected. This additional metal site is positioned within 7.5 Å between two adjacent electron transfer chains of two protomers and is thought to enable crosstalk between the pathways. The conserved position of the mononuclear metal site (11.5 Å from the [NiFe] active center) is occupied by a single Fe, the function of which is not yet understood. A narrow, 25-Å long hydrophobic channel is observed by xenon derivatization experiments. The position of the channel differs significantly from the canonical hydrophobic channels previously detected in other [NiFe] hydrogenases. Finally, the combined approach of X-ray crystallography and vibrational spectroscopy reveals that *Mb*FRH is isolated in the previously structurally uncharacterized Ni_a-S state. This state was characterized by the peculiar four Cys-coordinated seesaw-shaped geometry of the Ni ion with two *trans* S(Cys)-Ni-S(Cys) at 107° and 171°, short Ni–Fe distance of 2.7 Å and an open Ni coordination site.

ZUSAMMENFASSUNG

Metalloproteine in biologischen Systemen katalysieren herausfordernde enzymatische Reaktionen, darunter die Ausbildung und den Abbau chemischer Bindungen, Radikalchemie, Atom- und Elektronentransfer. In der vorliegenden Arbeit werden zwei metallbasierende Enzymsysteme aus Archaeen, nämlich Ni-haltige Kohlenmonoxid-Dehydrogenase (CODH) und [NiFe]-haltige Hydrogenase, strukturell untersucht.

CODH katalysieren die reversible Reduktion von CO_2 nach CO. In Archaeen ist diese Reaktion an die Synthese und den Abbau von Acetyl coenzyme A (Acetyl-CoA) gekoppelt, die durch ein Acetyl-CoA Decarbonylase/Synthase (ACDS) Proteinkomplex katalysiert wird. Innerhalb des ACDS-Komplexes wird die Chemie einer Kohlenstoff-Kohlenstoff-Bindung durch die Zusammenarbeit von fünf Proteinuntereinheiten, mindestens 33 Eisen-Schwefel-Zentren, 6 Cobalt und 12 Nickel-haltigen aktiven Zentren koordiniert. Trotz der umfangreichen biochemischen und spektroskopischen Charakterisierungen und des Vorhandenseins der Kristallstrukturen der Untereinheiten bakterieller und archaealer Homologe, ist die Struktur des ACDS-Komplexes unbekannt.

Im ersten Teil der Arbeit werden die Untersuchungen des ACDS-Komplexes des hyperthermophilen sulfatreduzierenden Archaebakterium *Archaeoglobus fulgidus* mittels Transmissionselektronenmikroskopie geschildert. Das gereinigte Protein zeigt sich als ein globuläres Partikel bei der Negativkontrastierung und der Kryo-Einbettung. Die 3D-Rekonstruktion mit einer Auflösung von 29 Å wird *de novo* anhand einer Einzelpartikelanalyse ermittelt. Drei mögliche Positionen für die CODH-Untereinheit werden innerhalb des ACDS-Komplexes mithilfe von rigid-body fitting vorgeschlagen.

Im zweiten Teil der Arbeit wird die Röntgenkristallstrukturanalyse der CODH-Untereinheit des ACDS Komplexes aus *A. fulgidus* geschildert. Dieses Protein ist durch ein *cdhAB*-Operon codiert und besteht aus α- und ε-Untereinheiten, die zusammen ein Heterodimer mit $\alpha_2\varepsilon_2$-Stöchiometrie bilden (*Af*$\alpha_2\varepsilon_2$). Während die Gesamtstruktur von *Af*$\alpha_2\varepsilon_2$ jener von *Methanosarcina barkeri* (*Mb*$\alpha_2\varepsilon_2$) ähnelt, führt der Austausch der koordinierenden Cys zu Asp und Glu zu einer Deletion des verbrückenden Eisen-Schwefel-Zentrums. Wie die Sequenzanalyse zeigt, wird dieses strukturelle Merkmal in verschiedenen Phyla von Bakterien und Archaeen beobachtet, darunter in 31 Enzymen, die durch *cdhAB*-Gene kodiert werden, und in 14 homologen CODH-Enzymen, die durch *cooS*-Gene kodiert werden. Die phylogenetische Analyse deutet darauf hin, dass die Cluster-Deletion durch Gentransfer innerhalb der evolutionären Linie, des horizontalen

Gentransfers oder unabhängigen Cysteinaustausches entstehen könnte. Zusätzlich wird die Rolle der ε-Untereinheit durch kinetische Studien untersucht. Die CO-abhängige FAD-Reduktionsaktivität von *Af*$\alpha_2\varepsilon_2$ folgt einer Michaelis-Menten Kinetik mit einem k_{cat} von 186 s^{-1} und K_M von 76 µM. Die *Mb*$\alpha_2\varepsilon_2$ hat ein ähnliches Michaelis-Menten Kinetik Verhalten sowie ähnliche kinetische Konstanten der FAD- und FMN-Bindung. Im Gegensatz dazu weist die CODH-II von *Carboxydothermus hydrogenoformans*, die keine ε-Untereinheit hat, eine lineare Abhängigkeit der CO-abhängigen FAD-Reduktionsaktivität innerhalb des verwendeten Konzentrationsbereiches von Flavin auf. Diese Beobachtungen sind im Einklang mit der Annahme, dass die ε-Untereinheit ein Gerüst für die Flavinbindung bereitstellt.

Der dritte Teil der Arbeit ist der F_{420}-reduzierenden Hydrogenase aus *M. barkeri* (*Mb*FRH) gewidmet, die zur Gruppe 3 der [NiFe]-Hydrogenasen gehört und die reversible Redoxreaktion zwischen H_2 und Coenzym F_{420} katalysiert. Die Struktur von *Mb*FRH wurde mit Hilfe der Röntgenkristallographie bestimmt. Sie ähnelt der Struktur von FRH aus *Methanothermobacter marburgensis* (*Mm*FRH) und ergibt eine sphärische, dodekamerische Anordnung von ca. 1.2 MDa. Zusammen mit der etablierten Elektronenübertragungskette, die in *Mm*FRH beobachtet wird und aus dem aktiven [NiFe]-Zentrum, vier [4Fe4S]-Clustern und FAD besteht, wird in *Mb*FRH auch ein [2Fe2S]-Cluster detektiert. Diese zusätzliche Metallstelle wird innerhalb von 7.5 Å zwischen zwei benachbarte Elektronentransferketten von zwei Protomeren positioniert und kann einen Elektronenübergang zwischen diesen ermöglichen. Die konservierte Position des Metalls, die 11.5 Å vom [NiFe] Aktivzentrum entfernt ist, wird von einem Fe besetzt, dessen Funktion noch nicht geklärt ist. Ein schmaler, 25 Å langer hydrophober Kanal wurde mithilfe von Xenon-Derivatisierungsexperimenten analysiert. Die Position des Kanals unterscheidet sich signifikant von den kanonischen hydrophoben Kanälen, die zuvor in anderen [NiFe]-Hydrogenasen nachgewiesen wurden. Schließlich führen die schwingungsspektroskopischen Analysen zusammen mit der Röntgenkristallographie zu dem Schluss, dass *Mb*FRH in einem bisher strukturell nicht charakterisierten, katalytisch aktiven Ni_a-S Zustand isoliert wurde. Dieser Zustand ist durch die vier Cys koordinierte "Wippe"-Geometrie des Ni-Ions mit zwei *trans* S(Cys)-Ni-S(Cys) Winkeln von 107° und 171°, einer kurzen Ni-Fe-Distanz von 2.7 Å und einer offenen Ni-Koordinationsstelle gekennzeichnet.

This research was carried out between September 2013 and December 2018 at the Humboldt-Universität zu Berlin, in the biochemistry/structural biology research group under the supervision of Prof. Holger Dobbek. Selected results of this research have been prepared for the following publications:

Die vorliegende Arbeit wurde unter der Leitung von Prof. Holger Dobbek von September 2013 bis Dezember 2018 in der Arbeitsgruppe Biochemie/Strukturbiologie an der Humboldt-Universität zu Berlin angefertigt. Im zeitlichen Rahmen dieser Dissertation wurden die Teile der erzielte Ergebnisse zur Veroffentlichung vorbereitet:

Protein structural constraints tune biocatalytic dihydrogen cycling by [NiFe] hydrogenases (manuscript submitted)
Yulia Ilina, Christian Lorent, Sagie Katz, Jae-Hun Jeoung, Seigo Shima, Marius Horch, Ingo Zebger, Holger Dobbek

Ni-containing carbon monoxide dehydrogenase revisited: crystal structure of the archaeal CODH could shed a light on the ACDS complex arrangement and an auxiliary electron acceptor (manuscript in preparation)
Yulia Ilina, Jae-Hun Jeoung, Harald Huber and Holger Dobbek

Nickel, Iron, Sulfur Sites (accepted for publication in *Met. Ions Life Sci.*).
Y. Ilina, B. M. Martins, J.-H. Jeoung and H. Dobbek.

The extended reductive acetyl-CoA pathway: ATPases in metal cluster maturation and reductive activation.
Jeoung JH, Goetzl S, Hennig SE, Fesseler J, Wörmann C, Dendra J (Ilina Y), Dobbek H.
Biol Chem. 2014 May; 395(5): 545-58

ABBREVIATIONS

A_{sp}	specific activity
ACDS complex	acetyl-CoA decarbonylase/synthase complex
ACS	acetyl-CoA synthase
*Af*ACDS/*Af*ACDS complex	ACDS complex from *Archaeoglobus fulgidus*
Af$\alpha_2\varepsilon_2$/*Af*$\alpha_2\varepsilon_2$-subunit	CODH subunit of ACDS complex from *A. fulgidus*
ATP	adenosine-5´-triphosphate
BV	benzyl viologen
c_{cs}	concentration of the catalyst site
cdhCODH	Cdh-type carbon monoxide dehydrogenase
*Ch*CODH-II	CODH II from *Carboxydothermus hydrogenoformans*
CoA	coenzyme A
CoB	coenzyme B
CODH	carbon monoxide dehydrogenase
CoM	coenzyme M
CoM-S-S-CoB	hetereodisulfude of CoM and CoB
CoFeSP	corrinoid-iron-sulfur protein
csCODH	CooS-type CODH
cryo-EM	cryo-electron microscopy
DHS	deoxyhypusine synthase
DT	sodium dithionite
*Dv*CODH	CODH from *Desulfovibrio vulgaris*
$E^{0'}$	standard redox potential at 25°C and pH 7
EPR	electron paramagnetic resonance
F_{420}	8-hydroxy-5-deazaflavin / coenzyme F_{420}
FAD/$FADH_2$	flavin adenine dinucleotide/reduced form
Fd	ferredoxin
Fe-GP	iron-guanylylpyridinol cofactor
FMN	flavin mononucleotide
FRH	F_{420}-reducing hydrogenase
FRH-A	subunit A of FRH
FRH-B	subunit B of FRH
FRH-G	subunit G of FRH
FSC	Fourier shell correlation
FT-IR	Fourier-transform infrared spectroscopy
H_4F	tetrahydrofolate
H_4MP	tetrahydromethanopterin
H_4SPT	tetrahydrosarcinapterin
Hdr	heterodisulfide reductase
Hmd	H_2-forming methylenetetrahydromethanopterin dehydrogenase
k_{cat}	turnover number
k_{eff}	specificity constant (k_{cat}/K_M)

K_M	Michaelis constant
kDa	kilodalton
*Mb*ACDS/*Mb*ACDS complex	ACDS complex from *Methanosarcina barkeri*
Mb$\alpha_2\varepsilon_2$/*Mb*$\alpha_2\varepsilon_2$-subunit	CODH subunit of ACDS complex from *M. barkeri*
*Mb*FRH	FRH from *M. barkeri*
MDa	megadalton
MF	methanofuran
MM kinetic	Michaelis-Menten kinetic
MeTr	methyltransferase
*Mm*FRH	FRH from *Methanotermobacter marburgensis*
Mo-CODH	Mo- and Cu-containing CODH
MP	methanopterin
*Mt*CODH	CODH from *Moorella thermoacetica*
MV	methyl viologen
Mvh	methanogenic F_{420}-non-reducing hydrogenase
NAD^+/NADH	nicotinamide adenine dinucleotide/reduced form
$NADP^+$/NADPH	nicotinamide adenine dinucleotide phosphate/reduced form
Ni-CODH	Ni- and Fe-containing CODH
NS	negative staining
RR spectroscopy	Resonance Raman spectroscopy
*Rr*CODH	CODH from *Rhodospirillum rubrum*
SEC	size exclusion chromatography
SPA	single particle analysis
TEM	transmission electron microscopy
TTP	thiamine pyrophosphate
U	Unit
U/mg	Unit per milligram
WL pathway	Wood-Ljungdahl pathway

TABLE OF CONTENT

1 INTRODUCTION

1.1 METALS IN BIOLOGY

Around a third of all proteins in the cells utilize metals as cofactors (*1*). Metalloenzymes catalyze diverse biochemical reactions, including photosynthesis (Mn, Cu, Fe, Zn, Mg) (*2*), carbon-carbon bond formation (Ni, Fe) (*3*), water oxidation (Mn, Ca) (*4*), molecular oxygen reduction (Fe, Cu) (*5, 6*), nitrogen fixation (Mo, Fe) (*7*), and hydrogen metabolism (Ni, Fe) (*8*). The wide catalytic range originates from the ability of transition metals to adopt several oxidation states and diverse coordination environments.

The cooperation of two such bioactive metals, Ni and Fe, contribute to a unique active site architecture that is capable of reversibly catalyzing hydrogen and carbon monoxide oxidation in [NiFe] hydrogenases and Ni- and Fe-containing CO dehydrogenases (Ni-CODH), respectively. A description of these enzymes will be discussed in further detail in the following chapters.

1.2 CO DEHYDROGENASES

CODHs catalyze a pivotal reaction in the global carbon cycle: the reversible oxidation of CO to CO_2 (Eq. 1).

$$2\,e^- + 2\,H^+ + CO_2 \rightleftharpoons CO + H_2O \qquad E^{0'} = -558\ mV \qquad (Eq.1)$$

For many aerobic and anaerobic microbes, CODH enables the use of CO as a sole energy and carbon source. Prokaryotic CO oxidation accounts for the removal of 10^8 tones of CO per year from the lower atmosphere, which maintains a CO concentration below toxic levels (*9*). Under aerobic conditions, CO is irreversibly oxidized by the Mo- and Cu-containing CODH (Mo-CODH) (*3, 10*), whereas anaerobically this reaction can be effectively reversed by oxygen-sensitive Ni-CODH (*11*). Despite catalyzing the same chemical reaction, Ni- and Mo-CODHs are encoded by different operons (*12*) and share no structural similarity. The following work focuses on the anaerobic Ni-CODH system.

1.2.1 CLASSIFICATION OF Ni-CONTAINING DEHYDROGENASES

Ni-CODHs have been found in many physiologically and phylogenetically diverse microorganisms both in bacteria (e.g. hydrogenogens, phototrophs, acetogens etc.*)* and archaea (e.g. methanogens, sulfate reducers) (*13*). Analysis of the available prokaryotic genomes revealed that 6% of sequenced archaeal and bacterial genomes contain at least

one CODH gene (*14*). According to the classification proposed by Lindahl *et al.* (*15*), the Ni-CODH family can be divided into four major classes (Fig. 1).

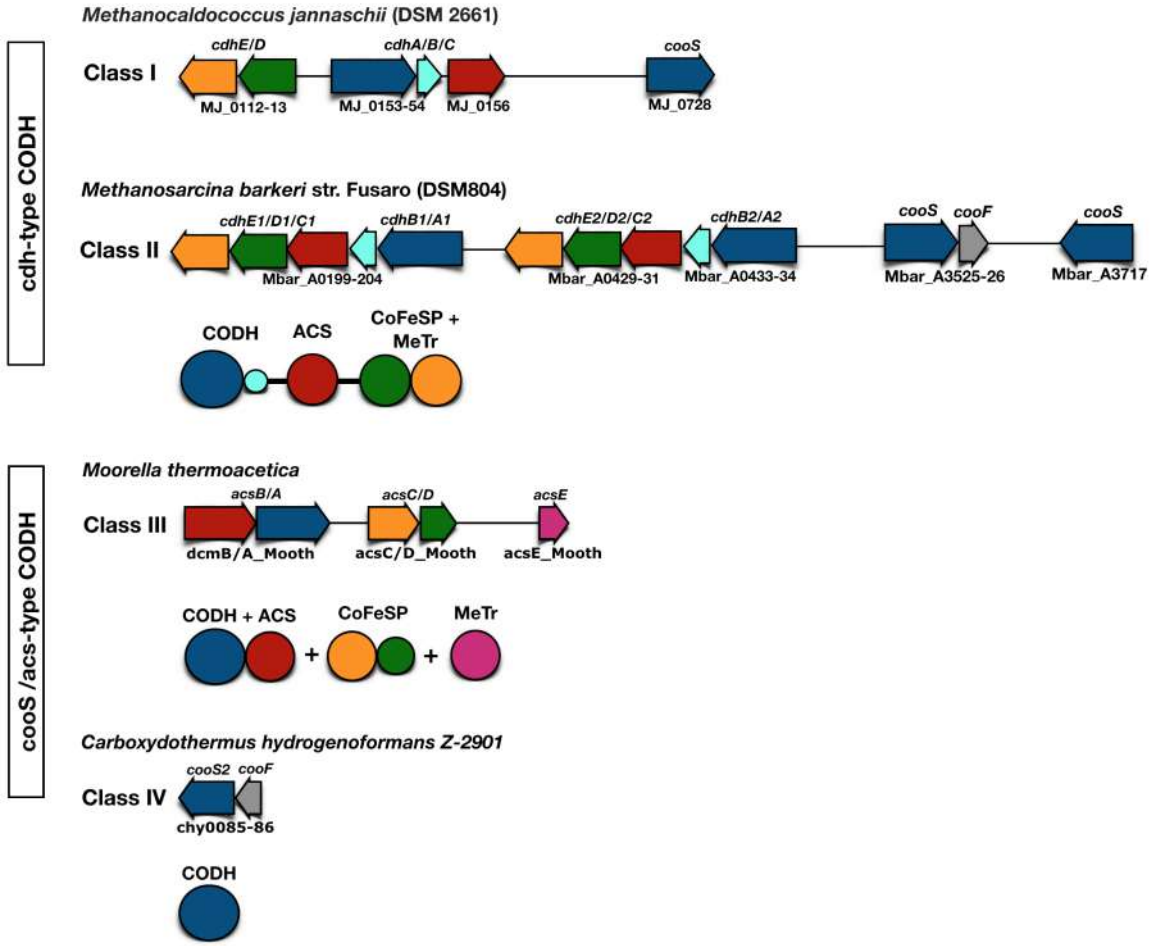

Figure 1. Ni-CODH classification. Ni-CODH gene clusters are shown as arrows. Homologous genes (arrows) and corresponding proteins (circles) are depicted in the same colors: CODH and α-subunit in blue, ACS and ß-subunit in red, large subunit of CoFeSP and γ-subunit in orange, small subunit of CoFeSP and δ-subunit in green, MeTr in magenta, and ferredoxin CooF in gray. In archaea CODH forms a tight protein complex with ACS, CoFeSP and MeTr (class I and II), whereas in bacteria CODH undergoes a complex formation with ACS (class III) or exists as a monofunctional homodimer (class IV). Gene and UniProt entry names are written above and below the gene clusters respectively.

Class I and II are found in obligate autotrophic and acetoclastic methanogens, respectively, where they catalyze (reversible in case of Class II) acetyl-CoA synthesis. Ni-CODHs of both classes are components of a ca. 2.0 MDa multisubunit protein complex: acetyl-CoA decarbonylase/synthase (ACDS) (*16, 17*). The ACDS complex is composed of five subunits: α, ε, ß, δ and γ, encoded by the genes organized into a *cdh* operon, corresponding to the *cdhA*, *cdhB*, *cdhC*, *cdhD* and *cdhE* genes, respectively. The Ni-CODH is comprised of the α- (CdhA) and ε- (CdhB) subunits, which form a

heterodimer with $\alpha_2\varepsilon_2$-subunit composition (*18*). The δ- (CdhD) and γ- (CdhE) subunits, which are homologs of the small and large subunits of the bacterial corrinoid-iron-sulfur protein (CoFeSP), catalyze the activation and reversible methyl (CH_3) group transfer between a cobalamine cofactor and tetrahydromethanopterin (H_4MPT) (*17, 19*). Lastly, the ß-subunit, which is a homolog of the bacterial acetyl-CoA synthase (ACS), catalyzes reversible acetyl-coenzyme A (acetyl-CoA) synthesis from the activated CH_3-group, provided by the δ- and γ-subunits, coenzyme A (CoA) and CO, provided by the $\alpha_2\varepsilon_2$-subunit (*19*).

Class III Ni-CODH enzymes form a heterodimer with ACS with a $CODH_2$-ACS_2 subunit composition and are found in homoacetogens, such as *Moorella thermoacetica* (*Mt*CODH) (*20*). Two subunits of the bacterial CoFeSP and MeTr form a tight heterodimeric protein complex with $CoFeSP_2$-$MeTr_2$ composition and catalyze the transfer of the CH_3-group from tetrahydrofolate (H_4F) to a cobalamin cofactor and finally to the active site of ACS (*21*). Similar to Class I and II enzymes, $CODH_2$/ACS_2, together with $CoFeSP_2$-$MeTr_2$, catalyze acetyl-CoA synthesis, but unlike the ACDS complex undergo transient interactions during catalysis and do not form a stable protein complex.

Class IV is represented by the monofunctional Ni-CODH homodimer, which has been studied in *Carboxydothermus hydrogenoformans* (*Ch*CODH) *(22)* and *Rhodospirillum rubrum* (*Rr*CODH) (*23*). Ni-CODHs of class IV are encoded by *cooS* gene and catalyze the reversible oxidation of CO to CO_2. Class IV Ni-CODH are often clustered with ferredoxin, encoded by *cooF* gene, and together they are involved in CO-dependent H_2 evolution, coupling the oxidation of CO to CO_2 (E^0 = -0.52 mV) with the reduction of protons to H_2 (E^0 = -0.41 mV) (*24, 25*). During this process, the electrons from CO oxidation are transferred from Ni-CODH to the membrane-associated CO-activated hydrogenase with CooF as an electron mediator (*24, 25*).

Based on the location within *cdh* (class I and II) or *coo* (class III and IV) operons, Ni-CODHs are referred to as cdhCODH or csCODH, respectively.

1.2.2 MULTIPLE OCCURANCE OF *cdh* AND *coo* OPERONS

Except for some rare examples in Firmicutes (*26*), Chloroflexi and Deltaproteobacteria (3.3.5), the cdhCODHs occur exclusively in archaea, whereas csCODHs are present in both archaea and bacteria (Fig. 1) (*13*). As suggested by phenotypic analyses, csCODHs are not required for growth of *Methanosarcina aceivorans* C2 strain, but are still expressed along with cdhCODHs in the presence of CO, methanol and acetate (*27*).

Mutants lacking two *cooS* orthologs (*cooS1F* and *cooS2*) grew slower on CO when compared to the wild type (*27*). These experiments support a role for csCODHs in archaea during the carboxidotrophic growth.

Many methanogens contain more than one cdhCODH isoform (*28-30*). Different *cdh* isogens of one organism share, on average, over 80% amino acid sequence identity, as observed in *Methanosarcina barkeri* (ca. 86%), *M. acetivorans* (ca. 83%) and *Methanosarcina mazei* (ca. 87%). Quantitative analysis of the *cdhA*-RNA isolates of *M. mazei* suggested that different isoforms are associated with distinct metabolic roles, namely with either acetyl-CoA cleavage or autotrophic carbon fixation required for acetyl-CoA synthesis (*31*). Consistent with this assumption, the expression of the *cdhA* genes can be regulated on the transcriptional level depending on the identity of the substrate, as demonstrated in *Methanosarcina thermophila* (*32*) and *M. acetivorans* (*28*). However, in *M. acetivorans*, both cdhCODH isoforms (Cdh1 and Cdh2) complement each other, as indicated by qualitative comparison of growth between strains lacking one of the *cdh* loci (*28*). Despite significant differences in growth rates, one CdhA isoform is sufficient for both acetoclastic or carboxydothripic growth.

1.2.3 AUTOTROPHIC CARBON FIXATION

Ni-CODH is a critical enzyme in the reductive acetyl-CoA (Wood-Ljungdahl) pathway, which is one of six pathways used by prokaryotes for carbon fixation (*33, 34*) and believed to be ancient in origin (*35*). The Wood-Ljungdahl (WL) pathway consists of two branches, termed methyl and carbonyl branches, which are dedicated to progressively reducing two CO_2 molecules to methyl and CO respectively (Fig. 2). The carbonyl branch is conserved among bacteria and archaea and is represented by Ni-CODH and ACS proteins (*36*). The enzymes of the methyl branch synthesize folate-derived one-carbon carriers (H_4F in bacteria (and some halophiles (*37*)) and H_4MPT in archaea) and enable the transfer of the methyl-group to the ACS active site.

In bacteria, the initial step of the methyl branch is CO_2 reduction to formate, which is subsequently bound to H_4F. In the following steps, formyl is progressively reduced to methyl, which is finally transferred by MeTr to Co^{1+}-cobalamin cofactor of CoFeSP. The latter interacts directly with ACS and provides the CH_3-group for acetyl-CoA synthesis. In archaea, CO_2 binds to methanofuran (MF), yielding formyl-MF as a product. In the next step, the formyl group is transferred to H_4MPT and is reduced by five electrons to methyl-H_4MPT. Similar to bacteria, the CH_3-group is transferred to the corrinoid-iron-

sulfur protein (γ-subunit) from methyl-H_4MPT by the methyl transferase (δ-subunit) of the ACDS complex. In the carbonyl branch, CODH catalyzes the reversible reduction of CO_2 to CO, which is further condensed with CoA and CH_3-group, generated by CoFeSP/MeTr in the methyl branch, yielding acetyl-CoA as a final product.

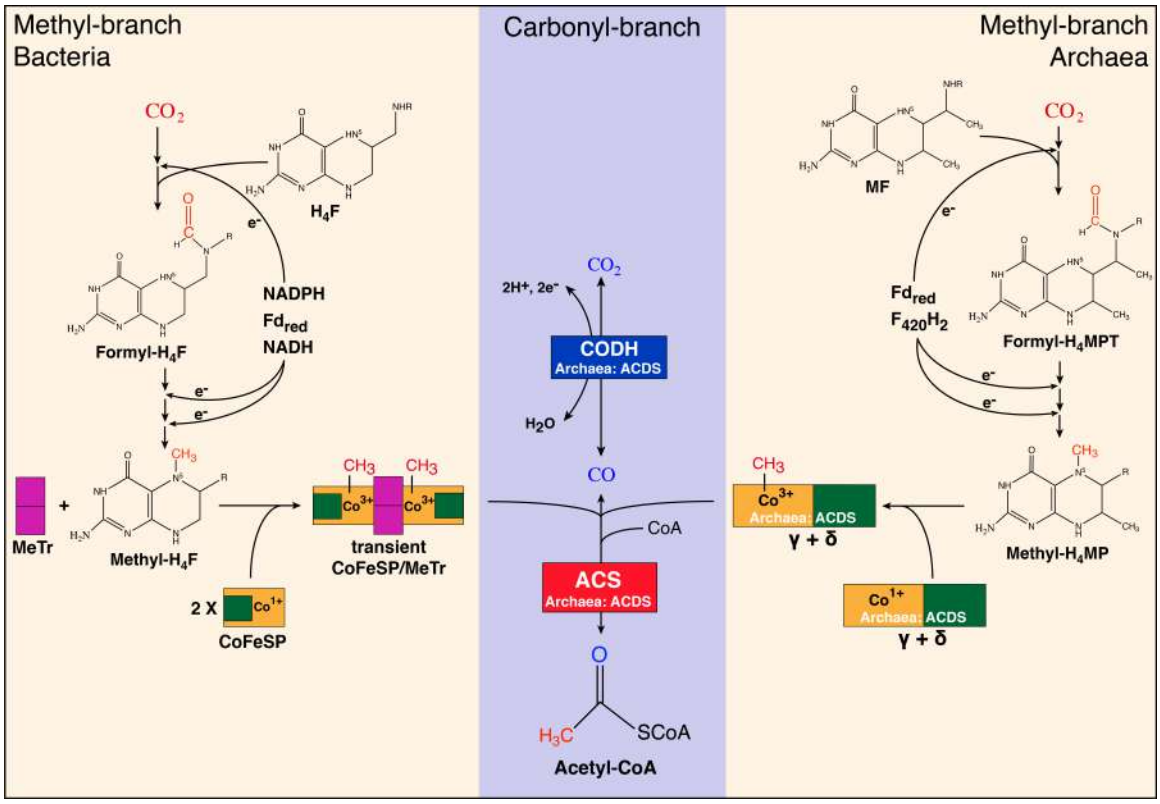

Figure 2. Methyl (yellow) and carbonyl (blue) branches of Wood-Ljungdahl pathway in bacteria and archaea. Selected proteins of the WL pathway are represented as boxes and colored as following: large CoFeSP- and γ-subunits in yellow; small CoFeSP- and δ-subunits in green; bacterial MeTr in magenta; ACS in red; CODH in blue. Fd_{red} stands for reduced ferredoxin. The figure is adapted from Adam *et al.* (*33*) and Sousa *et al*. (*34*).

Majority of the methyl branch enzymes are unrelated across both domains, sharing, on average, less then 12% sequence identity (e.g. when comparing 5,10-Methylene-H_4F reductase and 5,10-Methylene-H_4-MPT reductase; 5,10-Methenyl-H_4F cyclohydrolase/dehydrogenase and 5,10-Methenyl-H_4-MPT cyclohydrolase/5,10-Methylene-H_4-MPT dehydrogenase) (*36*). The electron carriers, such as 8-hydroxy-5-deazaflavin (coenzyme F_{420}) in archaea and NADPH/NADH in bacteria, used in CO_2-to-methyl reduction differ significantly between the two methyl branches (*36*). This indicates that both methyl branches evolved independently in archaea and bacteria, while acetogenesis, represented by the carbonyl branch, is conserved and could have been

acquired by vertical gene transfer (*36*). The ancient origin of the carbonyl branch is also supported by the presence of sulfur-rich transition-metal catalytic sites.

1.2.4 STRUCTURAL COMPARISON OF cdhCODH AND csCODH

Both cs- and cdhCODHs have been structurally characterized, revealing substantial similarities in the protein fold (sharing on average ca. 25% sequence identity) and cofactor composition.

Until now, one archaeal cdhCODH crystal structure from *M. barkeri* (*Mb*$\alpha_2\varepsilon_2$) has been solved (*18*), and four csCODHs from *C. hydrogenoformans* (*Ch*CODH-II) (*22*), *R. rubrum* (*Rr*CODH) (*23*), *Desulfovibrio vulgaris* (*Dv*CODH) (*35*) and *M. thermoacetica* (*Mt*CODH) (*20*) have been structurally characterized.

Both types of Ni-CODHs form a dimer with *C2* symmetry (Fig. 3A and B) containing five and nine metal clusters in csCODH and cdhCODH, respectively. The metal clusters are located within electron transfer distance to its nearest neighbor, enabling the intramolecular electron commute between the active site and the external electron acceptor (Fig. 3C and D) (*18, 36*). While csCODH is a homodimer, cdhCODH is a heterodimer with αε-protomer. The core structures of the csCODH-monomer and αε-protomer consist of two Rossmann fold domains and one N-terminal helix bundle domain (Fig. 3E and F). The latter contains the Cys ligands for the coordination of the two iron-sulfur clusters, termed cluster B and D, whereas the Ni,Fe-containing active site, termed cluster C, is positioned at the interface between two Rossmann fold domains, each providing five Cys and one His ligands for the cluster C coordination. The αε-protomer is composed of three additional structural elements: the C-terminal domain, which consists of several short α-helices and two ß-hairpins, the multi-helical [FeS] domain, which contains the coordinating Cys for two additional [4Fe4S] clusters, termed cluster E and F, and the 19 kDa ε-subunit. The position of the C-terminal domain coincides with the docking site of ACS in the bifunctional $CODH_2$-ACS_2 complex of class III (*18, 20*). In bacteria, this interaction is facilitated via the N-terminal domain of the ACS, which is completely depleted in its Cdh-homolog (ß-subunit) (*37*). Thus, it is rather unlikely that the C-terminal domain of the α-subunit provides a binding site for the ß-subunit within the ACDS complex. The ε-subunit adopts a Rossmann fold and belongs to the deoxyhypusine synthase (DHS)-like NAD^+/FAD-binding superfamily domain (*18*). This suggests that the ε-subunit could provide a scaffold for an accessory cofactor, such as flavin or thiamine (*38*). The potential role of the ε-subunit will be discussed in (3.3.7).

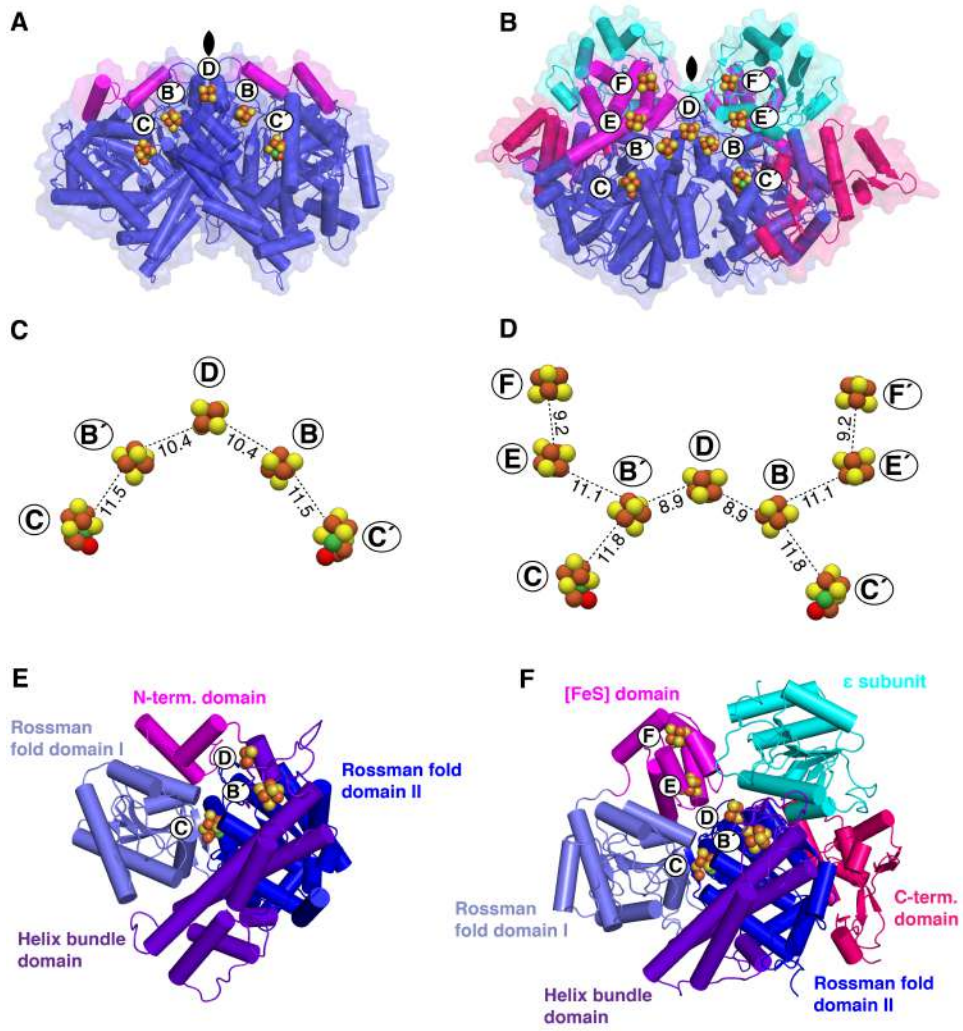

Figure 3. Structural comparison between csCODH and cdhCODH. (A) Protein structures of the *Ch*CODH-II homodimer (PDB entry: 3B53 (*39*)) and (B) *Mb*$\alpha_2\varepsilon_2$ heterodimer (PDB entry: 3CF4 (*18*)). Conserved elements of the protein core are depicted in blue. Convergent structural elements are shown in magenta, cyan and red. The electron transfer chain in (C) *Ch*CODH-II and (D) *Mb*$\alpha_2\varepsilon_2$. Distances are shown in Å. Domain composition of (E) *Ch*CODH-II monomer and (F) *Mb*$\alpha_2\varepsilon_2$ protomer. The protein backbone is shown as ribbons, metal clusters are shown as spheres (orange for Fe, yellow for S, green for Ni, red for oxygen).

The architecture of the active site together with its first and second coordination spheres are highly similar in cdh- and csCODHs (Fig. 4A and B). The structure of the active site is a heteronuclear pseudocubane [Ni3Fe4S] unit bridged to an exogenous Fe atom (*exo*-Fe), also referred to as the "dangling" iron or ferrous component II (FCII) in csCODHs (*18, 20, 22, 23, 35*). All three Fe atoms of the [Ni3Fe4S] unit are tetrahedrally coordinated, whereas the coordination of the *exo*-Fe differs from the Fe atoms of the Ni-containing subsite. Three labile sulfur atoms (denoted as μ_3-S), one Ni atom and three Fe atoms of the [Ni3Fe4S] unit approximate a conventional [4Fe4S] cluster, whereas *exo*-Fe is asymmetrically coordinated by one Cys and His, one μ_3-S and hydroxyl ligand

(observed in the absence of substrate). The Ni ion has a distorted T-shape coordination geometry and is ligated by two μ_3-S and one Cys, exposing a fourth coordination site for substrate binding. In the absence of the substrate, e.g. CO or CO_2, the Ni ion weakly interacts with the hydroxyl-ligand of the *exo*-Fe, which completes the square-planar coordination of Ni (*39*). Recent atomic-resolution structures of the substrate-bound cluster C (*39, 40*) (and substrate derivates (*40-42*)) of the csCODHs provided insight into the reaction mechanism of substrate binding to the cluster C. The structures suggested that the initial substrate docking occurs on the open coordination site of the Ni (*39-43*). The carbon atom of e.g. CO_2 or CO adopts a η^1 geometry, completing the square-planar coordination of Ni (*40-43*) (Fig. 4C). Independent of substrate choice (CO_2 (*39, 40*) or substrate derivates such as NCO^- (*40*), CN^- (*42*) or n-butylisocyanate (*41*)), ligand binding lead to a negligible structural rearrangement.

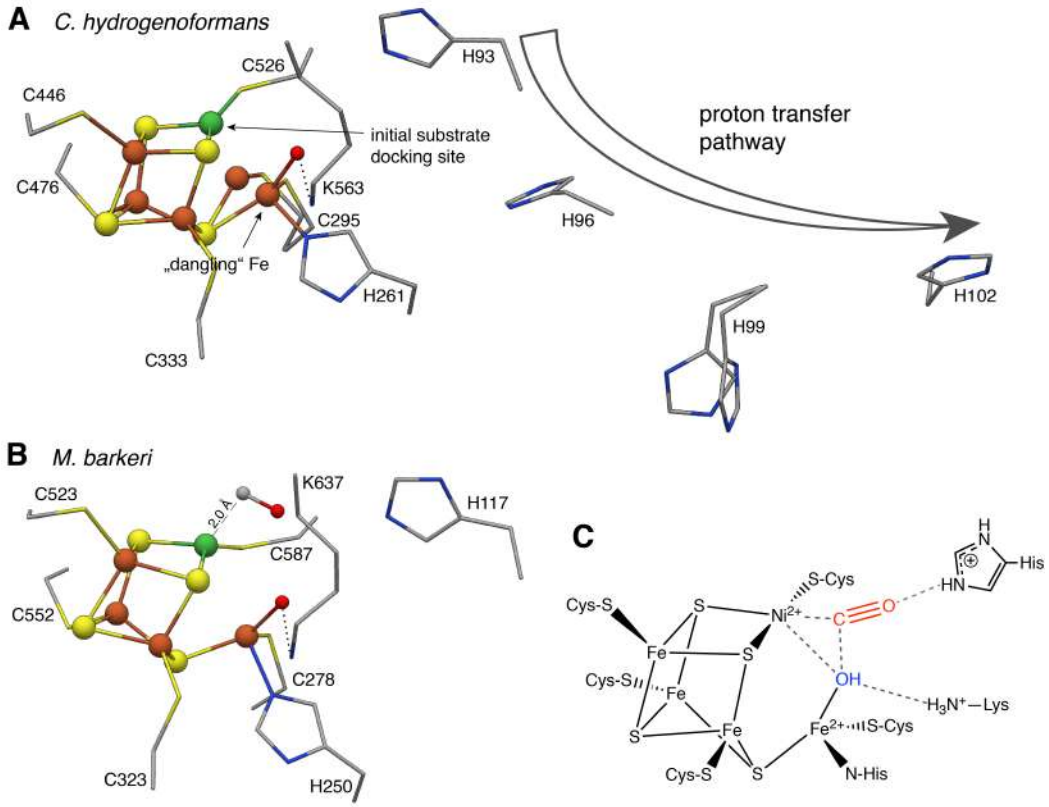

Figure 4. Structure of the cluster C in csCODH and cdhCODH. (A) Crystal structure of the cluster C of *Ch*CODH-II and its proton transfer network. (B) Crystal structure of the cluster C of *Mb*$\alpha_2\varepsilon_2$-subunit. (C) Electrostatic stabilization and stabilization of the transient intermediate via hydrogen bonding of conserved histidine and lysine upon CO binding. Metals are shown as spheres (orange for Fe, yellow for S, green for N, red for O), residues are shown as sticks.

A crystal structure of *Mb*$\alpha_2\varepsilon_2$ contains a two-atom ligand (refined as CO) ca. 2 Å above

the cluster C, binding to the terminal Ni atom at Ni-C-O angle of 102° (Fig. 4B) (*18*). Chemistry of transition metal carbonyl formation is characterized by two complementing bonding mechanisms, such as σ-bonding and π-backbonding (*44*). This results in a strong bond and linear CO-to-metal arrangement and contradicts the bending Ni-CO geometry, which was additionally disproved by the recent complementary crystallographic and Resonance Raman (RR) studies of the CN^- inhibited *Ch*CODH-II (*42*), which is often used as a CO analog. As proposed by Ciaccafava *et al.* (*42*), substrate could initially bind to Ni in a distorted tetrahedral geometry, lowering the activation barrier for CO oxidation, but rapidly rearranges on the sub-minute time scale to the stable square-planar Ni-CN coordination geometry, triggering the loss of the *exo*-Fe-bound hydroxyl ligand. Thus, it would be impossible to trap the initial CO binding step in the crystal, as suggested by Gong *et al.* (*18*).

Along with the high conservation of the residues in the first coordination sphere, two amino acids of the second coordination sphere, Lys (K563 in *Ch*CODH-II; K637 in *Mb*$\alpha_2\varepsilon_2$) and His (H93 in *Ch*CODH-II; H117 in *Mb*$\alpha_2\varepsilon_2$), which are 5 Å away from the Ni atom, are conserved among Ni-CODHs and could participate in catalysis (Fig. 4C) (*39*). Hydrogen bonding between His and a Ni-bound substrate could stabilize transient intermediates, whereas the ε-amino group of Lys could deprotonate the *exo*-Fe-bound hydroxyl ligand. From mutagenesis studies, the exchange of both His and Lys to Ala in *Mt*CODH completely abolished the CO oxidation activity (*45*). The result is explained by a disruption of the proton transfer network, which is conserved in both cs- and cdhCODHs (in *Ch*CODH-II: His93 → His96 → His99 → His102 (Fig. 4A); in *Mb*$\alpha_2\varepsilon_2$: His117 → His120 → His123 → Asp126/His127). Additionally, both charged amino acids could also help to stabilize the substrate-protein complex by electrostatic interactions.

Although the structure and active site coordination spheres of cs- and cdhCODHs are almost identical, they differ in the rate of their catalytic activities. The specific activity for CO oxidation is 13828 U/mg for *Ch*CODH-II (*46*) and 216 U/mg or less in *Mb*$\alpha_2\varepsilon_2$ or Cdh-homologues (*47-49*). The apparent K_M values for CO was estimated as 18 µM (*46*) and 5 mM (*47*) for *Ch*CODH-II and *Mb*$\alpha_2\varepsilon_2$ respectively. These striking differences can reflect the distinct physiological roles both enzymes play *in vivo*. Although both organisms can utilize CO as the sole carbon and energy source (*50-52*), in *M. barkeri* and other methanogens, *Mb*$\alpha_2\varepsilon_2$ (as part of ACDS complex) could primarily participate in carbonylation or decarbonylation reactions linked to acetate metabolism (*47*), and not

scavenge environmental CO as in the case of csCODHs. This hypothesis is consistent with the extremely slow growth of *Methanosarcina* str. on CO, which was only 1% of that observed with other substrates (*52*) and significant protein upregulation, yielding more then 10% of the total cellular protein content of acetate-grown cells (*48*).

1.2.5 ACETYL-CoA DECARBONYLASE/SYNTHASE COMPLEX

As discussed in chapter 1.2.1, the composition of the ACDS complex is highly conserved throughout the archaea domain (*17, 53*). ACDS consists of five different subunits, denoted α, ß, γ, δ, and ε. Only the structure of $\alpha_2\varepsilon_2$-subunit has been solved by X-ray crystallography at 2.0 Å resolution (Fig. 3B) (*18*). The structures of proteins homologous to the ß-, γ- and δ-subunits are available from *M. thermoacetica* (*21*) and *C. hydrogenoformans* (Fig. 5) *(54)*.

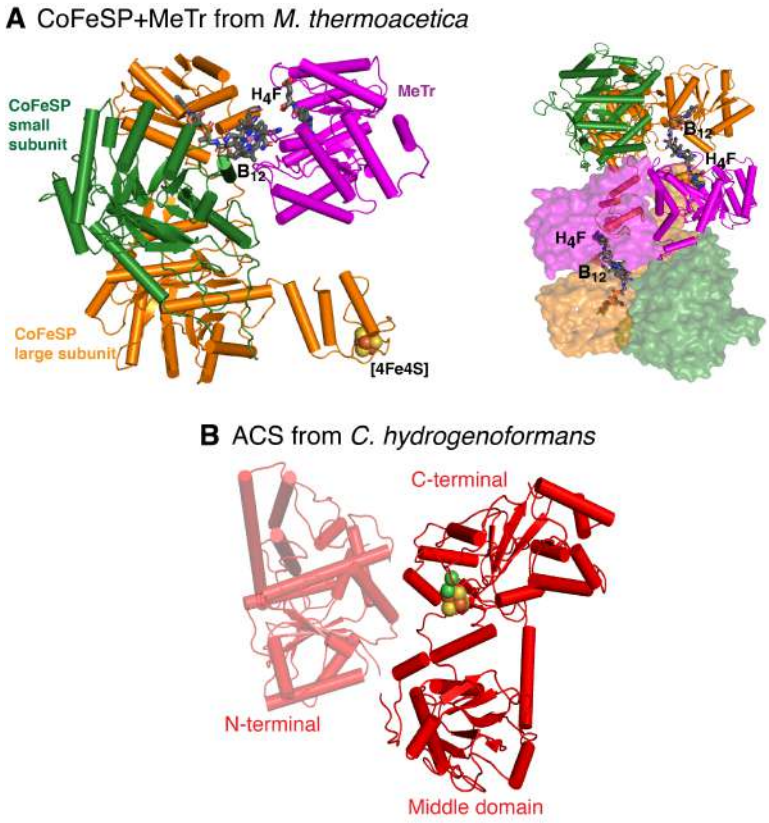

Figure 5. Crystal structures of the ß-, γ- and δ-subunits homologs from bacteria. (A) Crystal structure of the substrate-bound $CoFeSP_2$-$MeTr_2$ complex (right) and its protomer (left) from *M. thermoacetica* solved at 3.5 Å resolution (PDB: 4DJE (*21*)). The large CoFeSP subunit contains one cobalamin prosthetic group (B_{12}) and one [4Fe4S] cluster. MeTr binds one H_4F. (B) Crystal structure of the monomeric ACS from *C. hydrogenoformans* (PDB: 1RU3 (*54*)). The N-terminal domain, depleted in ß-subunit, is shown with 50% transparency. The protein backbone is shown as ribbons*;* H_4F or B_{12} cofactors are shown as sticks in gray. Metals are shown as spheres (orange for Fe, yellow for S, green for N, red for O).

The size and the stoichiometric arrangement of the complex are debated in the literature. Based on the estimated molecular weight of the ACDS complex, possible subunit arrangements are: an octamer of pentamers $(\alpha_2\varepsilon_2)_4$-$ß_8$-$(\delta\gamma)_8$ or hexamer of pentamers $(\alpha_2\varepsilon_2)_3$-$ß_6$-$(\delta\gamma)_6$ (*17, 55*). Proteolytic digestion with chymotrypsin or treatment with a strong cationic detergent can separate the complex into three subcomponents (*19*): $\alpha_2\varepsilon_2$ (approx. 220 kDa), truncated ß-subunit (approx. 50 kDa) and δγ-subunit (approx. 110 kDa). Three distinct catalytic activities were measured for these three protein subcomponents, confirming the correlation between bacterial homologues suggested by sequence analysis. The CO:acceptor oxidoreductase activity (Eq. 2) was assigned to the $\alpha_2\varepsilon_2$-subunit and the Co-ß-methylcobamide:tetrahydropteridine methyltransferase activity (Eq. 3) was catalyzed by the δγ-subunit (*19*). Acetyl-CoA synthesis activity was lost upon ACDS complex degradation, however the ß-subunit could still catalyze acetyl transfer between acetyl-CoA and 3′-dephospho-CoA (Eq. 4) (*19*).

$$\alpha_2\varepsilon_{2_{ACDS}} + CO_2 + 2e^- + 2H^+ \rightleftarrows \alpha_2\varepsilon_{2_{ACDS}} - CO + H_2O \qquad \text{(Eq. 2)}$$

$$\delta\gamma_{ACDS}(Co^{1+}) + CH_3H_4SPT^1 + H^+ \rightleftarrows \delta\gamma_{ACDS}(Co^{3+}) - CH_3 + H_4SPT \qquad \text{(Eq. 3)}$$

$$ß_{ACDS} + \text{acetyl} - \text{CoA} \rightleftarrows ß_{ACDS} - \text{acetyl} + \text{CoA} \qquad \text{(Eq. 4)}$$

In bacteria, three structural modules, namely large and small subunits of CoFeSP and MeTr, catalyze activation and CH_3-group transfer from H_4F to cobalamin-bound Co^{1+} and subsequently to the proximal Ni of the ACS active site (*15*). The structure of the substrate-free $CoFeSP_2$-$MeTr_2$ complex structure has been solved to 2.38 Å (Fig. 5A) (*21*). In ACDS complex, a similar reaction is catalyzed by only two subunits: δ and γ (*19*). Sequence and structure prediction suggest that the δ-subunit is similar to the small CoFeSP subunit and is responsible for methyl transfer between the methyl-H_4MPT to a cobinamide-bound Co^{1+} (*34*). Similar to known methyltransferases, the δ-subunit has a TIM-barrel fold (*34*). The γ-subunit is related to the large subunit of the bacterial CoFeSP, and thus could be responsible for binding the corrinoid cofactor and [4Fe4S] cluster (*34*).

The ACS crystal structure, a ß-subunit homolog in ACDS complex, is known from *C.*

[1] H_4SPT tetrahydrosarcinapterin

hydrogenoformans as monomer (Fig. 5B) (*22, 54*) and from *M. thermoacetica* as heterotetramer together with CODH (*20*). The middle and C-terminal domains of the bacterial ACS are homologous to the ß-subunit, whereas the N-terminal domain is absent.

1.3 HYDROGENASES

1.3.1 HYDROGENASES CLASSIFICATION

Hydrogenases are metalloenzymes that catalyze the reversible oxidation of molecular hydrogen (*8*). Hydrogenases are commonly found in archaea and bacteria (*56*), but examples of eukaryotic hydrogenases in protozoa, within hydrogenosomes (*57*), and in green algae, within chloroplasts (*58*), have been identified. Approx. 450 hydrogenase sequences are available, revealing a diversity with respect to electron donors and acceptors (*59*), physiological role (*60*), location within the cell, and size and architecture of the active site (*8, 56*). Extensive phylogenetic analysis of all non-redundant putative hydrogenase sequences have revealed eight major lineages (*60*), which could be grouped into three classes based on the metal content of the active site, namely [NiFe] (including the [NiFeSe] subclass (*61*)), [FeFe] (*62*) and [Fe] hydrogenases (Tab.1) (*63*).

Hydrogenases are highly efficient enzymes. Many purified hydrogenases *in vitro* are bidirectional and can catalyze both hydrogen uptake and hydrogen evolution, depending on the redox potential of the substrates (*8, 56*). *In vivo,* the direction of hydrogen metabolism is linked with the physiological role of the enzyme. *In vivo,* [FeFe] hydrogenases are tuned towards hydrogen evolution, whereas [NiFe] hydrogenases are biased towards hydrogen uptake (*64*). The activities for hydrogen metabolism of hydrogenases from all three classes are summarized in Table 2.

Table 1. Hydrogenase classification (adapted from (*60*)).

[NiFe] hydrogenase			
Group	Proposed selected function		Selected organism
Group 1	Membrane-bound H_2-uptake:	Electron generation for sulfate, fumarate, nitrate, aerobic and oxygen-tolerant anaerobic respiration	*D. vulgaris* *D. baculatum* *M. mazei*
Group 2	Cytosolic H_2-uptake:	Hydrogenase gene expression regulation by H_2 sensing; Electron input for aerobic respiration and H_2 recycling	*R. eutropha* *R. capsulatus*
Group 3	Cytosolic bidirectional H_2-oxidation and evolution:	Generation of the reducing equivalents; Coupling F_{420}-reduction with H_2 oxidation; Coupling NADPH oxidation with H_2 evolution; H_2 electron bifurcation to heterodisulphide and ferredoxin reduction; Methylviologen reduction	*M. marburgensis* *M. barkeri*
Group 4	Membrane-bound H_2-evolution:	Energy conversion via chemiosmosis Complex formation with Ni-CODH for anaerobic CO respiration using H+ as terminal electron acceptors; coupling ferredoxin oxidation to H_2 evolution (H^+/Na^+ translocation)	*C. hydrogenoformans* *R. rubrum* *M. barkeri*
[FeFe] hydrogenase			
Group A	H_2-oxidation and evolution	Coupling ferredoxin/formate oxidation with H_2 evolution; H_2 electron bifurcation to ferredoxin and $NAD(P)^+$	*C. pasteurianum* *D. desulfuricans*
Group B	Coupling ferredoxin oxidation with H_2 evolution		Uncharacterized
Group C	H_2 sensing: regulation of kinase / phosphatases genes expression		*T. saccharolyticum*
[Fe] hydrogenase			
Coupling H_2 oxidation with 5,10-methenyltetrahydromethanopt reduction			*M. jannaschii*

Table 2. Turnover number for hydrogen evolution and uptake for the three hydrogenase classes. The activities are defined as the number of hydrogen molecules generated or consumed per second by one catalytic site. Some values were corrected for protein concentration.

	[NiFe]	[NiFeSe]	[FeFe]	[Fe]
H_2 evolution	660[1]	500[5]	9000[6] 6000[7] 8700[9]	950[12]
H_2 uptake	760[2] 530[3] 9300[4]	135[5]	71000[10] 29000[11] 42000[9]	

[1]*D. gigas* (*65*); [2]*D .fructosovorans (66);* [3]*M. thermoautotrophicum* (*67*); [4]*M. barkeri (68);* [5]*D. baculatus (69)* [6]*D. desulfuricans (70);* [7]*C. pasteurianum (64);* [9]*D. vulgaris* str. Hildenborough (*64*); [10]*D. desulfuricans (66);* [11]*C. pasteurianum (66);* [12]*M. marburgensis (63)*.

1.3.1.1 THE [NiFe] HYDROGENASE CLASS

[NiFe] hydrogenases can be divided into four distinct groups based on physiological function and genetic relationship (Tab. 1) (*8, 71*). All [NiFe] hydrogenases catalyze the reversible heterolytic cleavage of H_2 to protons and electrons (Eq. 5).

$$H_2 \leftrightarrow [H^+ + H^-] \leftrightarrow 2H^+ + 2e^- \qquad E^{0'} = -414 \text{ mV} \qquad \text{(Eq.5)}$$

These enzymes are involved in a variety of the cellular processes in bacteria and archaea, such as energy generation by oxidation of molecular hydrogen, balancing the concentrations of reducing equivalents and the redox potential of the cell, regulation of gene transcription by hydrogen sensing, and establishing the proton motif force for ATP synthesis (*8, 60*). So far, no members of the [NiFe] hydrogenase class have been found in eukaryotes (*56*). The structure of the active site is highly conserved among [NiFe] hydrogenases, which contains a heterometalic Ni and Fe catalytic center. The active site is coordinated by four cysteinyl thiolates and three non-protein ligands: CO and two CN^- moieties (Fig. 6) (*8*), which were identified by Fourier-transform infrared (FT-IR) spectroscopy (*72*). In case of the [NiFeSe] hydrogenases, one Ni-ligating cysteine is replaced by a selenocysteine (*73, 74*).

The low spin Fe^{2+} does not change oxidation state during catalysis. Upon binding of the bridging (oxo-based/hydroxo- or hydride) ligand, Fe ion expands its coordination geometry from square pyramidal to octahedral (*8*). Ni is observed at three oxidation states (Ni^{1+}, Ni^{2+}, Ni^{3+}) throughout the catalytic cycle and switches between different coordination geometries (*8, 71*). In the absence of bridging ligand, Ni adopts a pseudo-tetrahedral geometry and upon binding of the oxo/hydroxo or hydride ligand, Ni adopts a pseudo-square pyramidal geometry.

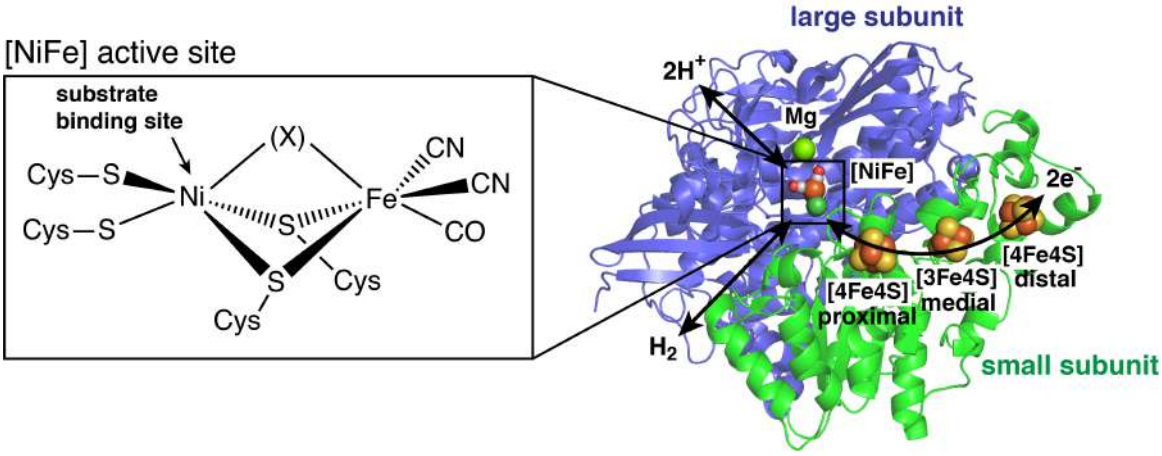

Figure 6. Crystal structure of [NiFe] hydrogenase from *D. vulgaris* str. Miyazaki (PDB entry: 1WUL (*75*)). [NiFe] active site is shown in the left inset. (X) indicates the bridging ligand: hydride or oxo-ligands in the active or inactive states, respectively. Protein backbone is shown in ribbons (blue and green for large and small subunits, respectively). Metal clusters are shown as spheres (Fe in orange, S in yellow, Ni in green). Arrows indicate the hydrophobic substrate channel (H_2), proton (H^+) and electron ($2e^-$) transfer network.

In solution, most [NiFe] hydrogenases are heterodimers, comprising two subunits (Fig. 6), but tetrameric (*76*) and dodecameric (*77*) arrangements have also been observed (Fig. 10). A striking feature of some members of the [NiFe] hydrogenase family, including some membrane-bound, regulatory, $NAD(P)^+$-reducing and [NiFeSe] hydrogenases, is the retention of catalytic activity in the presence of oxygen (*8, 78*). The mechanism of oxygen tolerance is not conserved among different oxygen-tolerant species and is not yet understood. For example, the oxygen tolerance of H_2-sensing regulatory hydrogenase in *Ralstonia eutropha* is hypothesized to originate from modulation of the protein matrix by narrowing the substrate channel (*79*). In *E. coli*, it is hypothesized that the six-cysteine coordinated medial [3Fe4S] cluster with an unusually high potential (approx. 190 mV) confers oxygen-tolerance by supplying two electrons for rapid reactivation of the active site upon oxygen exposure (*80*).

1.3.1.2 THE [FeFe] HYDROGENASE CLASS

Similar to [NiFe] hydrogenases, [FeFe] hydrogenases catalyze reversible conversion of H_2 to protons and electrons (*62*). These enzymes are found in anaerobic bacteria (e.g. *Clostridia*), anaerobic eukaryotes, fungi and green algae (*64*), but absent in archaea. The architecture of the [FeFe] hydrogenase active site, termed H-cluster, resembles the active site of the [NiFe] hydrogenases and is composed of a di-iron metal center coordinated each by a CO and CN^- ligand (Fig. 7) (*62, 64*). Furthermore, the two Fe atoms, termed proximal (Fe_p) and distal (Fe_d), are bridged by a dithiomethylamine group (-S-CH_2-NH-CH_2-S-) and a carbonyl ligand. Fe_p is linked to the conventional [4Fe4S] cluster via a cysteinyl residue, is octahedrally coordinated (*81*) and maintains its oxidation (1^+) state throughout the catalytic cycle. Similar to the Ni ion in [NiFe] hydrogenases, Fe_d is redox active ($2^+ \leftrightarrow 1^+$) and changes its coordination geometry from square pyramidal to octahedral upon substrate binding (*81*).

Unlike [NiFe] hydrogenases, [FeFe] hydrogenases operate under strictly anoxic conditions and are completely deactivated and denatured upon trace oxygen exposure (*82*).

1.3.1.3 THE [FE] HYDROGENASE CLASS

The [Fe] hydrogenases, also known as H_2-forming methylenetetrahydromethanopterin (methenyl-H_4MPT^+) dehydrogenases or Hmd, are restricted to some hydrogenotrophic methanogens and adopt the role of F_{420}-reducing hydrogenase under low Ni concentrations (*83*). [Fe] hydrogenases catalyze the reversible reduction of N^5,N^{10}-methenyl-H_4MPT^+ with H_2 to N^5, N^{10}-methylene-H_4MPT and protons by transferring a hydride ion to the C14a carbon (Fig. 8A). N^5, N^{10}-methylene-H_4MPT is involved in a reaction cascade leading to $CO_2 \rightarrow CH_4$ reduction (*34, 84*). The activity of the [Fe] hydrogenases is substrate-specific.

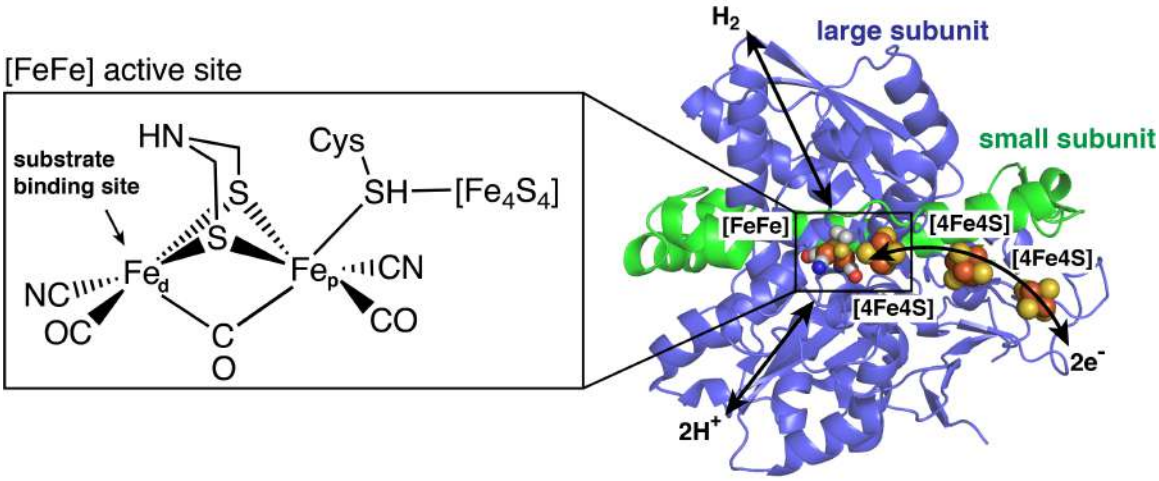

Figure 7. Crystal structure of [FeFe] hydrogenase from *D. vulgaris* str. Hildenborough (PBD entry: 1HFE (*85*)). [FeFe] active site is shown in the left inset. Protein backbone is shown in ribbons (blue and green for large and small subunits, respectively). Metal clusters are shown as spheres (Fe in orange, S in yellow, Ni in green). Arrows indicate the hydrophobic substrate channel (H_2), proton (H^+) and electron ($2e^-$) transfer pathways.

The [Fe] hydrogenase active site contains a unique iron-guanylylpyridinol cofactor, denoted as Fe-GP, in which a single Fe ion is coordinated by two *cis*-carbonyl groups, one cysteinyl thiolate as well as an acyl-carbon and sp^2 hybridized nitrogen atom from the pyridinol moiety (Fig. 8B) (*63*). Substrate binding to the open coordination site on the Fe completes its square pyramidal coordination sphere.

All three hydrogenase classes are phylogenetically unrelated and differ in their overall structure (*56*). While active sites of both [NiFe] and [FeFe] enzymes are buried deep inside the protein scaffold, the Fe-GP cofactor of the [Fe] hydrogenase is solvent-exposed (*8*). Alternations of the active sites result in differences within the catalytic cycles (*8*). In the following chapter, several structural features and the catalytic cycle of [NiFe] hydrogenases will be discussed in further detail.

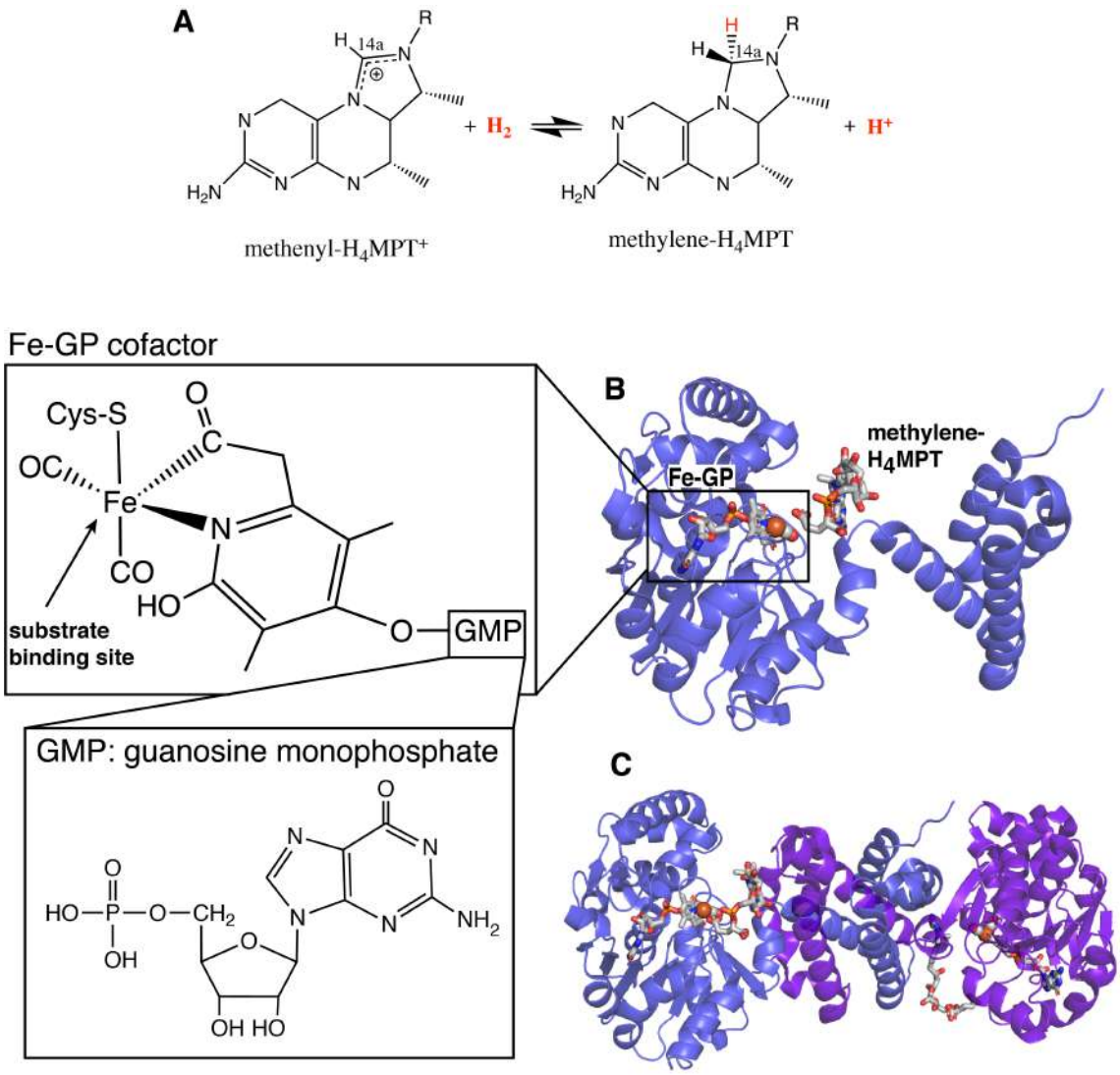

Figure 8. Crystal structure of [Fe] hydrogenase (Hmd) from *M. jannaschii* (PDB entry: 3H65 (*86*)). (A) Reduction of methenyl-H_4MPT^+ to methylene-H_4MPT with H_2 catalyzed by Hmd. (B) Hmd monomer with bound methylene-H_4MPT. Active site of the Hmd is shown in the left inset. (C) Structure of the Hmd homodimer. Protein backbone is shown in ribbons. Metal clusters are shown as spheres (Fe in orange, S in yellow, Ni in green). Methylene-H_4MPT and Fe-GP cofactors are shown as sticks.

1.3.2 [NiFe] HYDROGENASES

1.3.2.1 PROTEIN ARCHITECTURE

The core of all [NiFe] hydrogenases consists of two subunits, denoted as the large and small subunit (Fig. 6). The overall structural fold of these two subunits is very similar among distinct groups of [NiFe] hydrogenase class. The large has an approx. size of 60 kDa and harbors the [NiFe] active site and one bivalent ion bound approx. 15 Å from the active site (Fig. 9A).

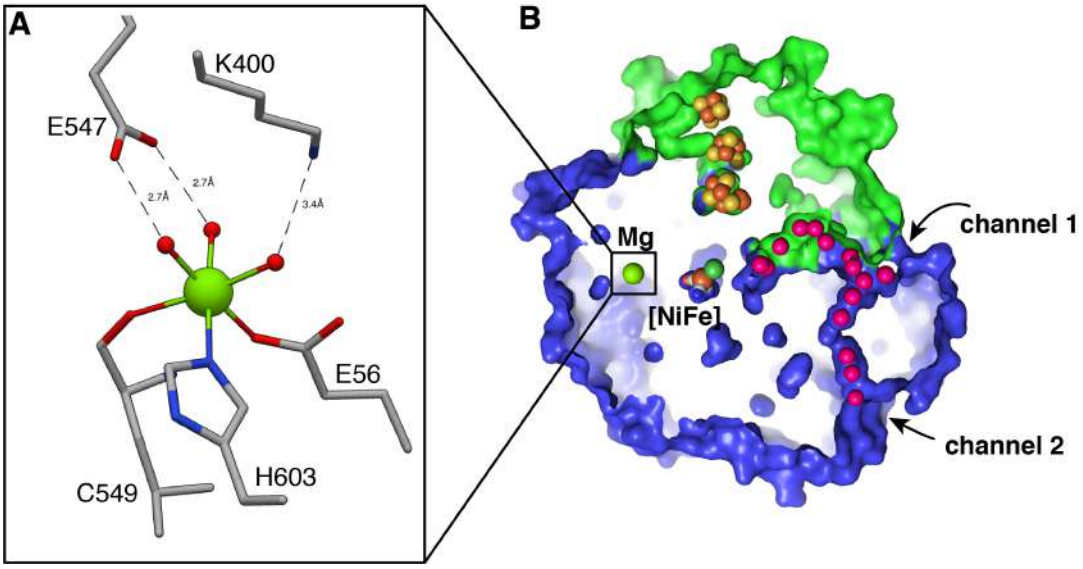

Figure 9. Mononuclear metal site and hydrophobic channel in [NiFe] hydrogenase in *R. eutropha* (PDB entry: 5D51 *(87)*). (A) Coordination of a single Mg ion. (B) Two major hydrophobic channels were observed using Kr-pressurized crystals. Large and small hydrogenase subunits are shown as surfaces in blue and green, respectively. Protein residues are shown as sticks in gray. Metals and krypton molecules are depicted as spheres (Fe in orange, S in yellow, Kr in magenta, Ni and Mg in dark and light green, respectively).

The X-ray analysis revealed that the position of this ion is exposed to the solvent and is occupied by either Mg^{2+}, Ca^{2+} or Fe^{2+}, which all are octahedrally coordinated by a consensus motif: C-terminal His, Glu, oxygen atom of the peptide bond and three water molecules (Tab. 3) (*71*). The role of this bivalent ion is unclear. It was suggested that the metal ion plays a stabilizing role during the maturation process of the large subunit, as the C-terminus of [NiFe] hydrogenases is cleaved at the coordinating His (*88*). In another hypothesis, the bivalent ion could participate in a secondary proton transfer pathway (e.g. His552 → Glu34 → Glu62 in *D. vulgaris* Miyazaki F) (*89*).

The [NiFe] active center is buried approx. 25 Å beneath the protein surface, and substrate must travel through the hydrophobic channel to reach the catalytic center. A crystallographic analysis of Kr (*87*) and Xe binding (*90*), together with molecular dynamics simulations of H_2 diffusion (*90*), revealed two main hydrophobic tunnels (Fig. 9B). The first tunnel is approx. 30 Å long and is positioned at the interface of the large and the small subunits (channel 1; Fig. 9B), whereas the second tunnel cuts through the large subunit and has a length of approx. 50 Å (channel 2; Fig. 9B). This tunnel network is present in most of the reported [NiFe] hydrogenases.

Table 3. Coordinating residues of the various mononuclear metal ions in the proximity of the [NiFe] active site. The coordinating residues to various mononuclear, bivalent metal ions in group 1 and group 3 [NiFe] hydrogenases. The large subunit (LS) of group 1 [NiFe] hydrogenases is homologous to the FRH-A subunit of archaeal F_{420}-reducing group 3 [NiFe] hydrogenases.

		Metal-coordinating residues			Water-interacting residues		
[NiFe] group 3	*M. barkeri* MS	H438 FRH-A	M399 FRH-A	E44 FRH-A	H105 FRH-G	E259 FRH-A	Fe^{2+}
	M. methanothermobacter	His386 FRH-A	A347 FRH-A	E44 FRH-A	T248 FRH-G	E229 FRH-A	
[NiFe] group 1	*D. fructosovorans*	H549 LS	L495 LS	E53 LS	K372 LS	E334 LS	Mg^{2+}
	E. coli	H582 LS	C528 LS	E57 LS	K399 LS	E347 LS	
	M. thermolithotrophicus	H448 LS	L395 LS	E42 LS	K273 LS	E264 LS	Ca^{2+}
[NiFeSe] group 1	*D. baculatum*	H498 LS	I444 LS	E51 LS	K321 LS	E285 LS	Fe^{2+}
	D. vulgaris Hildenborough	H495 LS	I441 LS	E56 LS	K317 LS	E282 LS	

The small subunit has a molecular weight of approx. 30 kDa and contains a chain of iron-sulfur clusters that facilitates electron transfer between the [NiFe] active site and the terminal electron acceptor. Based on the distance to the catalytic center, the clusters are denoted as proximal, medial and distal (Fig. 6). In various organisms, different compositions, coordination motifs and midpoint potentials were observed for the iron-sulfur clusters (Tab. 4).

Table 4. Composition, coordinationmorif and midpoint potentials of the distinct iron-sulfur clusters in [NiFe] hydrogenases (modified according to (*77*) and (*80*)).

		Proximal	Medial	Distal
A. vinosum	Type	[4Fe4S]	[3Fe4S]	[4Fe4S]
	Ligands	Cys_4	Cys_3	Cys_3His_1
	E (mV)	87	68	-78
R. eutropha	Type	[4Fe3S]	[3Fe4S]	[4Fe4S]
	Ligands	Cys_5	Cys_3	Cys_3His_1
	E (mV)	-60	25	-180
D. gigas	Type	[4Fe4S]	[4Fe4S]	[4Fe4S]
	Ligands	Cys_4	Cys_3	Cys_3His_1
	E (mV)	-290	-35	-340

Table 4 (cont.)

D. vulgaris	Type	[4Fe4S]	[3Fe4S]	[4Fe4S]
	Ligands	Cys_4	Cys_3	Cys_3His_1
	E (mV)	-300	-70	-300
M. marburgensis (F_{420}-reducing)	Type	[4Fe4S]	[4Fe4S]	[4Fe4S]
	Ligands	Cys_3Asp_1	Cys_4	Cys_4
	E (mV)	-400	-400	-400
E. coli (oxygen-tolerant Hyd-1)	Type	[4Fe3S]	[3Fe4S]	[4Fe4S]
	Ligands	Cys_6	Cys_3	Cys_3His_1
	E (mV)	230	190	n.d.

1.3.2.2 PHYSIOLOGICAL DIVERSITY OF [NiFe] HYDROGENASES

The minimal catalytic core in most [NiFe] hydrogenases consists of large and small subunits (*8*). However, many [NiFe] hydrogenases contain additional functional units or interact with other enzymes (*56*). The conformational variety allows the hydrogenases to expand the range of their physiological roles. The dodecameric F_{420}-reducing hydrogenases (FRH-ABG) comprise three subunits, termed FRH-A, FRH-B and FRH-G, whereas FRH-A and FRH-G are homologous to the large and small subunits of the group 1 [NiFe] hydrogeneses respectively (*77*). The additional FRH-B subunit contains a [4Fe4S] cluster and FAD and can reversibly reduce coenzyme F_{420} (Fig. 10A) (*77*). The NAD^+-reducing soluble hydrogenase (SH) is a heterotetramer in which two subunits, HoxH and HoxY, function as hydrogenase (Fig. 10B) (*91*). The remaining subcomplex of HoxF and HoxY functions as a diaphorase and facilitates the conversion between NAD^+ and NADH (Fig. 10B) (*91*). Regulatory hydrogenases binds histidine protein kinase and regulates the expression of hydrogenase genes (*8*). Methanogenic F_{420}-non-reducing hydrogenase, MvhAGD, can form a complex with heterodisulfide reductase (HdrABC). The electrons generated during hydrogen oxidation by MvhAGD are used to reduce ferredoxin (Fd) and hetereodisulfude of coenzyme M and B (CoM-S-S-CoB) (Fig. 10C) (*92*). The mechanism of this reaction implies a flavin-based electron bifurcation process.

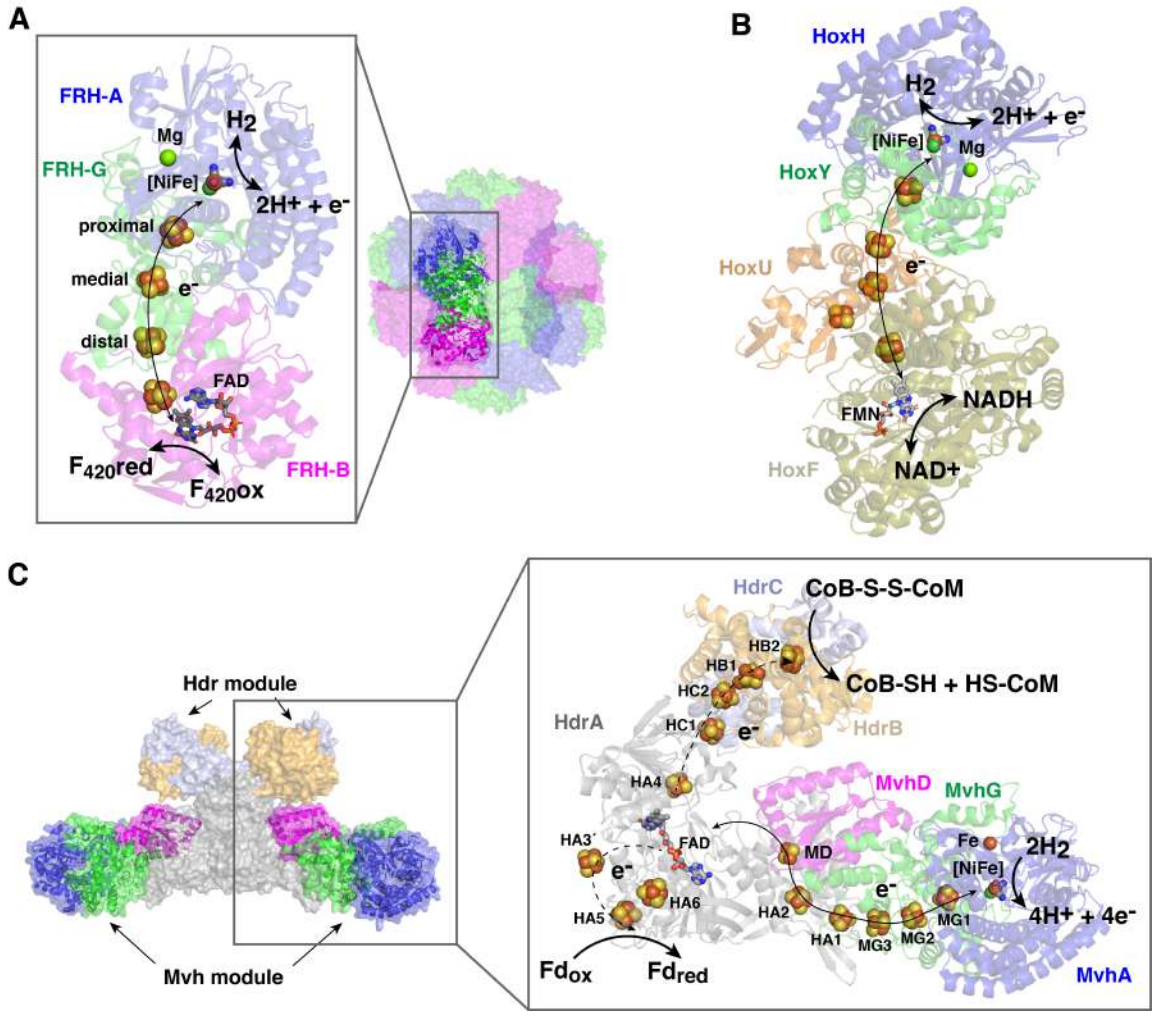

Figure 10. Diversity of the physiological roles of [NiFe] hydrogenases. (A) Structure and ET pathway of FRH-ABG protomer from *M. marburgensis* (PDB entry: 4OMF (*77*)). Protein backbone is shown as ribbons (FRH-A subunit in blue, FRH-G subunit in green, FRH-B in magenta) (left inset). Structure of the FRH-ABG oligomer is represented as surfaces (right). (B) Structure and ET pathway of the NAD^+- reducing SH from *H. thermoluteolus* (PDB entry: 5XF9 (*91*)). Hydrogenase subunits (HoxH in blue and HoxY in green) and diaphorase subunits (HoxU in orange and HoxF in olive) are shown as ribbons. (C) Structure and ET pathway for HdrABC-MvhAGD complex from *M. thermolithotrophicus* (PDB entry: 5ODR (*92*)). Overall structure of HdrABC-MvhAGD complex is represented as surface for Hdr and surface/ribbons for Mvh (left). Hydrogenase subunits (MvhA in blue, MvhG in green and MvhD in magenta) and heterodisulfide reductase subunits (HdrA in gray, HdrB in sand yellow and HdrC in pale blue) are shown as ribbons (right inset). Arrow indicates the ET pathway. Metals are depicted as spheres (Fe in orange, S in yellow, Ni and Mg in dark and light green, respectively).

1.3.2.3 REACTION MECHANISM OF [NiFe] HYDROGENASES

The oxidized, inactive state is characterized by a bridging ligand observed between the metal ions of the [NiFe] active site, as revealed by crystallographic analysis (*75, 93*). Two

inactive states have been identified, Ni-A and Ni-B, that differ from each in the reactivation time under reducing conditions and the nature of the bridging ligand (Fig. 11) (*8, 71*). Ni-B is reactivated within a minute, whereas the enzymes in Ni-A state need approx. 1 hour of reactivation time as demonstrated in *Desulfovibrio* sp. (*75*). Another feature of the inactive state is the oxygenation of one of the Ni-coordinating sulfur cysteines (*75, 94*). The identity of the bridging ligand of the Ni-A state is still unknown. Crystal structures of the Ni-A states suggested OH^-, OOH^- (*93*) or sulfur atom (*95, 96*) as the bridging ligand, from which OH^- ligand best accommodates the recent electron paramagnetic resonance (EPR) spectroscopic and discrete Fourier transform (DFT) simulation data (*97*). The assignment of the bridging ligand for the Ni-B state is less ambiguous, and is assigned to OH^- ligand by crystallographic (*75*) and electron nuclear double resonance (ENDOR) spectroscopic analysis (*98*). During the inactive state, Ni is in the 3^+ oxidation state and has a distorted square-pyramidal coordination (*71*). Both inactive states can be generated upon oxygen exposure or using chemical oxidants, such as 2,6-dichlorophenolindophenol or potassium hexacyanoferrate (III) (*99*).

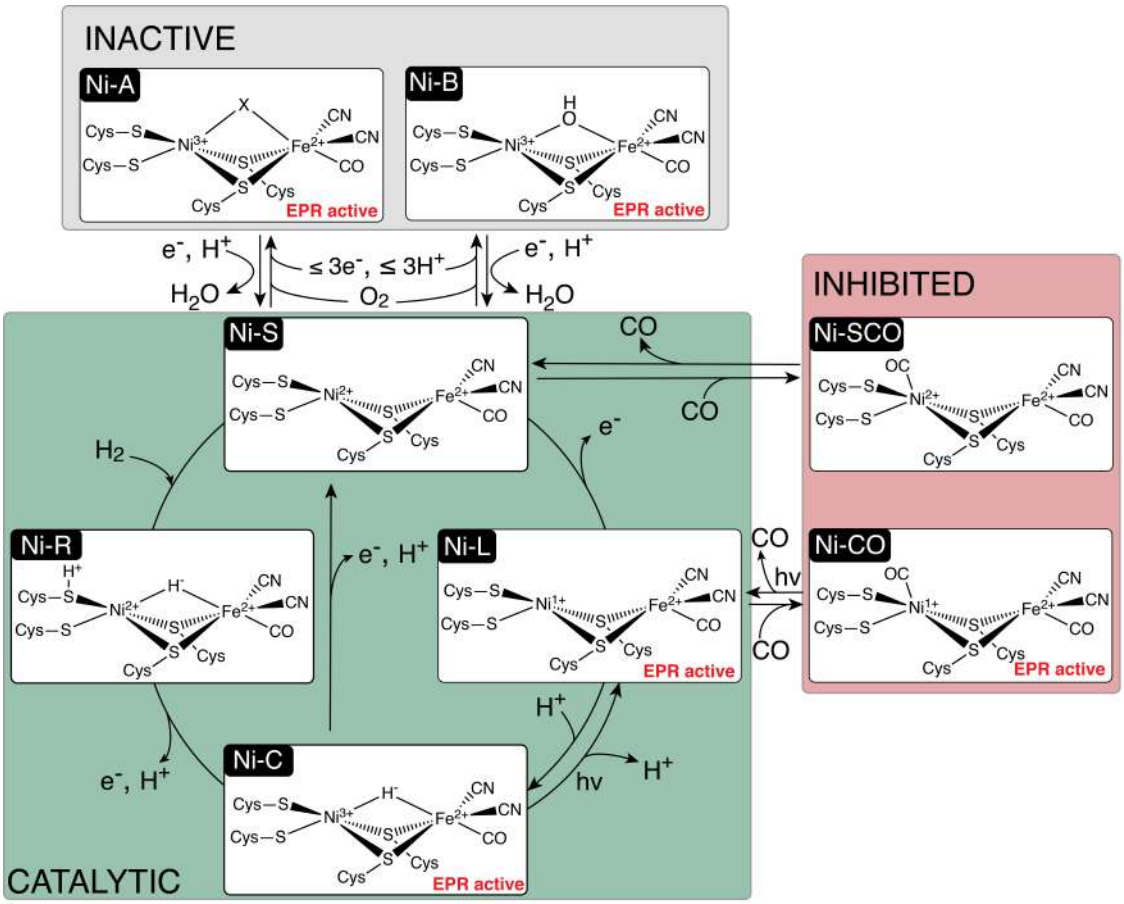

Figure 11. Reaction mechanism of [NiFe] hydrogenases (modified according to (*8*)).

Reduction of the Ni-A and Ni-B states removes the bridging ligand between Ni and Fe and the active site is converted into the catalytically-active EPR-silent Ni-S state (Fig. 11). The absence of the bridging ligand and an unusual four-cysteine Ni-coordination geometry (referred as "seesaw"-coordination) with an open site was confirmed by EPR, Mössbauer and IR spectroscopies (*8, 100-102*). The Ni-S state can be inhibited upon incubation with CO. The resulting EPR-silent light-sensitive state, denoted Ni-SCO, was solved by X-ray crystallography, revealing the extrinsic CO binding to the Ni atom with angles of 130 to 160° (*103*). The Ni-SCO state can be reversed to Ni-S state upon illumination at cryogenic temperatures. These findings indicate that Ni could provide an initial binding site for hydrogen.

In the next step of the catalytic cycle, hydrogen binds to the Ni atom in the Ni-S state and is subsequently heterolytically split. The resultant Ni-R state is characterized by a bridging hydride ligand between low spin Ni^{2+} and Fe^{2+} atoms and one protonated cysteine residue (Fig. 11) (*89*). At least three distinct pH-dependent Ni-R states were identified by FT-IR spectroscopy, each containing different protonation sites in the first coordination sphere (*8*). The X-ray structure of the fully-reduced state was solved at 0.89 Å (*89*).

The loss of one proton and one electron results in a paramagnetic intermediate Ni-C state, for which the hydride bridge is still present between the Ni and Fe (Fig. 11). Upon light elimination, Ni-C is converted to Ni-L, in which the hydride bridge is lost and the Ni atom is in the 1^+ oxidation state (Fig. 11). This process is reversible at ambient temperature in the dark (*104*). Recent results from FT-IR spectroscopy suggest that Ni-L state is part of the catalytic cycle and occurs as an intermediate between Ni-C and Ni-S conversion at 130-198 K (*105*). Partial (up to 18%) conversion between the Ni-C and Ni-S states is also observed upon light irradiation at 198 K under H_2 or N_2 atmosphere or under N_2 atmosphere at 198 K in the dark (*105*).

Incubation of the enzyme in the Ni-L state generates a paramagnetic inhibited state, denoted Ni-CO (Fig. 11). This state is reversible and converts back to the Ni-L upon illumination.

Based on the available X-ray structures, few conformational changes in the protein scaffold were observed throughout the catalytic cycle. The most apparent changes concern the Ni-Fe distances, which became shortened with progressive reduction (2.57 Å for Ni-R state (*89*) compared to 2.8 – 3.2 Å for the oxidized states (*75, 93*)).

1.4 AIM OF STUDY

Natural metalloenzymes function under mild conditions and demonstrate high catalytic activity and substrate specificity for a wide range of chemical reactions, including bond formation, redox and radical chemistry. The aim of this study is to structurally investigate two enzyme systems, which facilitate catalysis using transition metals. The first is represented by a member of the reductive acetyl-CoA pathway, acetyl-CoA decarbonylase/synthase (ACDS) complex, and one of its subunits, Ni-containing CO dehydrogenase (CODH). The most significant feature of the ACDS complex is its ability to form and break a carbon-carbon bond via Ni, Fe and Co-containing active sites. CODH uses Ni and Fe cofactors to consume CO_2 as a feed stock and reversibly converts it into energy-bearing products such as CO. The second system is represented by the [NiFe] hydrogenase, a central enzyme in hydrogen metabolism and valuable potential energy carrier in zero-emission fuel. Structural characterization of these enzyme systems can provide valuable information for the design of efficient organometallic catalysts without the use of precious metals, such as rhodium, palladium, iridium, platinum *etc*., which are routinely used industrially for carbon-carbon bond formation and H_2-based energy systems.

2 MATERIALS AND METHODS

2.1 CHEMICALS AND ENZYMES

All chemicals were of analytical grade or higher and purchased from AppliChem (Darmstadt, Germany), Biorad (München, Germany), Merck (Darmstadt, Germany), Roth (Karlsruhe, Germany) and BD Bioscience. Pure gases (N_2, H_2 and CO) and gas mixtures (N_2/H_2 (95% / 5%) and N_2/CO_2 (80% / 20%)) were purchased from Air Liquide.

α-Chymotrypsin from bovine pancreas and DNAse-I were purchased from Merck (Darmstadt, Germany).

2.2 OTHER MATERIALS

Chromatography resins and columns were purchased from GE Healthcare. High pressure resistant bottles for the anaerobic cultivation of archaea were obtained from Duran (Mainz, Germany). Grids for transmission electron microscopy were purchased from Quantifoil Micro Tools (Jena, Germany).

2.3 ANOXIC WORK

All experiments were conducted in anaerobic glove boxes (model B; Coy Laboratory Products or in-house construction) unless stated otherwise. Coy glove boxes were equipped with Pd catalysts to remove trace oxygen and kept under an atmosphere of 5% H_2 and 95% N_2. Anoxic buffer solutions were prepared using Schlenk line technique in sealed vessels (butyl or natural rubber septum) by consecutive evacuation and purging with N_2.

2.4 MICROBIOLOGY

Methanosarcina strains were grown on acetate- or methanol- containing media, employing batch cultivation technique. Procedures and guidelines regarding the anaerobic cultivation techniques were acquired by personal correspondence with Dr. Klaus Fiebig (Freie Universität Berlin), Prof. Dr. Rolf Thauer (Max Planck Institute for Terrestrial Microbiology, Marburg) and Dr. Seigo Shima (Max Planck Institute for Terrestrial Microbiology, Marburg).

2.4.1 ARCHAEAL STRAINS

The source for acetate-grown *Methanosarcina barkeri* str. Fusaro (DSM804) was kindly provided as an actively growing cell culture by Dr. Klaus Fiebig. Methanol (MeOH)-grown *Methanosarcina barkeri* MS (DSM800) was purchased from the DSMZ (German

Collection of Microorganisms and Cell Cultures) as an actively growing cell culture. Lactate-grown *Archaeoglobus fulgidus* VC-16 (DSM4304) was obtained from Dr. Harald Huber (Universität Regensburg) as a flash-frozen cell pellet.

2.4.2 CULTURE MEDIUM

Sterile media were prepared anaerobically in an atmosphere that contained N_2/CO_2 (4:1 ratio). All gases were passed through an autoclaved glass olive tightly packed with glass wool.

Reagents (except for methanol (MeOH) and sodium sulfide (Na_2S) solution) (Tab. 5) were solubilized with ddH_2O and mixed well by agitation. Media were dispensed into cultivation vessels (DURAN®-Protect bottles) to a maximum half-volume capacity in order to avoid overpressure-related explosions during autoclaving or by gas evolution from organisms during growth. The media were made anaerobic by purging with N_2/CO_2 (4:1 ratio) for ca. 30 min. Subsequently, bottles with anaerobic media were sealed with butyl rubber stoppers secured by screw collars and sterilized using the RG fast cooling module (Varioklav 135S, Langensebold, Deutschland). Autoclaved media were cooled to ca. 37°C and freshly purged with N_2/CO_2 (4:1 ratio) gas mixture for ca. 30 min or until the precipitates were dissolved. There were no precipitates observed in MeOH-containing media, thus purging was not performed. The precipitates in the acetate-containing media prepared in small volumes (equal or less than 500 mL) dissolved overnight at 37°C without additional mixing. The final pH of the media was 6.7 – 6.8. Finally, the supplements (Na_2S for Medium A and Na_2S + MeOH for Medium M; see Tab. 5) were added to the sterile media via syringe next to a lit Bunsen burner. The properly prepared medium was a vivid yellow color and contained minimal to no precipitation.

Table 5. Composition of the growth medium with acetate (medium A) and MeOH (medium M) as substrate.

	Medium A	Medium M
0.5 M Bis-Tris, pH 6.8	–	100 mL
NH_4Cl	0.5 g	
$MgSO_4$ x 7 H_2O	0.5 g	
$FeSO_4$ x 7 H_2O	2 mg	
$CaCl_2$ x 2 H_2O	0.25 g	
NaCl	2.25 g	
$NaHCO_3$	0.85 g	
K_2HPO_4	0.348 g	
KH_2PO_4	0.227 g	
yeast extract	2 g	
casitone	2 g	
trace element solution	1 mL	
200 × vitamin solution	5 mL	
1 g/L resazurin solution	0.5 mL	
L-Cysteine-HCl x H_2O	0.157 g	
Na-acetate x 3H_2O	13.6 g	–
dd H_2O	to 1000 mL	
STERILISATION		
200 mM Na_2S solution	6.8 mL	
MeOH	–	10 mL

2.4.3 SUPPLEMENTS

2.4.3.1 TRACE ELEMENT SOLUTION

$FeCl_2$ was dissolved in 6.8 mL 12 M (37%) HCl and subsequently diluted in ca. 50 mL of water. Remaining salts (Tab. 6) were added to the initial $FeCl_2$ solution and dissolved. The solution was diluted to a final volume of 1000 ml.

Table 6. Composition of the trace element solution (SL-10 DSMZ).

37% HCl	6.8 mL
$FeCl_2$ x 4 H_2O	1.5 g
$ZnCl_2$	70 mg
$MnCl_2$ x 4 H_2O	100 mg
H_3BO_3	6 mg
$CoCl_2$ x 6 H_2O	190 mg
$CuCl_2$ x 2 H_2O	2 mg
$NiCl_2$ x 6 H_2O	24 mg
Na_2MoO_4 x 2 H_2O	36 mg
ddH_2O	to 1000 mL

2.4.3.2 VITAMIN SOLUTION

All reagents for the vitamin solution (Tab. 7) were solubilized in ddH_2O, sterile-filtered with a 0.2 µm polyvinylidene fluoride membrane, aliquoted into 45 mL fractions and stored at -20°C.

Table 7. Composition of the vitamin solution.

Biotin	2 mg
Folic acid	2 mg
Pyridoxine-HCl	10 mg
Thiamine-HCl	5 mg
Riboflavin	5 mg
Nicotinic acid	5 mg
D-Ca-pantothenate	5 mg
Vitamin B12	0.1 mg
p-Aminobenzoic acid	5 mg
Lipoic acid	5 mg
ddH_2O	500 mL

2.4.3.3 SODIUM SULFIDE SOLUTION

Hydrated Na_2S crystals were rinsed with ddH_2O and dried with paper cloth prior to weighting. The 200 mM Na_2S stock solution was made anaerobic by purging with 100% N_2 for ca. 30 min. Finally, the solution was sterilized by autoclaving in a sealed flask as described above for culture media.

2.4.3.4 RESAZURIN SOLUTION

50 mg of resazurin was dissolved in 50 mL ddH_2O to obtain the 1 g/L stock solution and stored at room temperature.

2.4.4 INOCULATION

Active culture of *Methanosarcina* sp. was inoculated using a sterile male-to-male Luer lock connector next to a lit Bunsen burner. All surfaces were rinsed with ethanol and flame-sterilized using standard aseptic technique. The medium was maintained at 37°C prior inoculation in order to prevent an extensive lag phase. The cells were inoculated into the fresh media with an inoculum to growth medium ratio of 1:10 (for 0.1 mL, 0.25 mL, 0.5 mL and 1 L media) or 1: 28 (for 7 L media).

2.4.5 CELL GROWTH

Methanosarcina cells grew in anoxic media A or M (Tab. 5) at 37°C without agitation. The cell mass sufficient for a single protein purification (ca. 10 g) was obtained from a 14 L culture (two 7 L culture media in 15 L bottles) for acetate- and 4 L culture (four 1 L culture media in 2 L bottles) for MeOH-grown *M. barkeri*. Cells were harvested in the late logarithmic phase of growth by anaerobic centrifugation for 15 – 20 min at 3500 × *g* and washed with 50 mM MOPS, pH 7.2, 150 mM NaCl, 5 – 10% (w/v) glycerol for acetate-grown cells or 25 mM Na-HEPES, pH 7.5, 150 mM NaCl 5 – 10% (w/v) glycerol for MeOH-grown cells. Finally, cell material was flash frozen in liquid nitrogen (lN_2) and stored at -80°C. *Methanosarcina* culture (0.25 L or 0.5 L) could rest at room temperature for a maximum of 3 months and be revived by reinoculation into fresh medium. The gas production of the culture followed with a delay of 1 to 4 weeks. The revived cell culture was repeatedly reinoculated three to five times before it could be propagated as an inoculum for the large-scale cell cultivation.

2.4.6 ANALYTICAL METHODS

Growth of *Methanosarcina* sp. was monitored by measuring the total gas production over time. The excess gas was removed with 20 mL or 60 mL syringes until the cultivation flask became isobaric with ambient atmospheric pressure.

During the exponential growth phase, the gas production was measured twice per day for the MeOH-grown *Methanosarcina*, and for acetate-grown cultures, the pressure was measured every second day.

2.5 PROTEIN PURIFICATION

2.5.1 ACDS COMPLEX FROM *M. barkeri* (*Mb*ACDS)

10 g frozen cells (*M. barkeri* str. Fusaro) were resuspended in ca. 50 mL of 50 mM MOPS pH 7.2 with 150 mM NaCl and 5% (w/v) glycerol (buffer A). The cell suspension was sonicated (Bandelin Sonoplus 2200) for 15 mins (5 × 5 cycles, 50% amplitude) in a rosette cooling cell on ice. Shortly after sonication, a spatula tip-full of DNAse was added to the disrupted cell suspension, which was then dispensed into polycarbonate tubes with screw-cap assemblies and centrifuged at 120 000 g for 45 min at 12°C. The supernatant was applied at a flow rate of 3.5 mL/min to a Sepharose 4B-CL column (50 mm × 870 mm in XK 50 column), equilibrated in buffer A containing 2 mM Na-dithionite (DT). *Mb*ACDS complex was eluted between 850 and 1100 mL as single peak, concentrated to ca. 7 mg/mL using a pressure concentrator (Amicon, 500 kDa MWCO), and frozen and stored in lN_2 (-196°C).

2.5.2 ACDS COMPLEX FROM *A. fulgidus* (*Af*ACDS)

10 g frozen cells (*A. fulgidus* VC-16) were resuspended with a brush in ca. 50 mL of 25 mM Na-HEPES pH 7.5 containing 150 mM $(NH_4)_2SO_4$ and 5% (w/v) glycerol (buffer B1). The cells were sonicated and centrifuged as in (1.5.1). The soluble crude extract was fractionated in buffer B1 supplemented with 2 mM DT (buffer B2) as in (2.5.1). The *Af*ACDS complex peak eluted between 700 and 1000 mL and was assayed for CO-dependent MV reducing activity (2.6.3). Protein fractions correlated with reducing activity were collected and loaded at 1 mL/min on a Source 30Q column (ca. 20 mL) equilibrated in buffer B2. After washing the column with 4 to 5 CV of buffer B2, *Af*ACDS complex was recovered by a linear gradient elution of 0 – 500 mM NaCl in a buffer containing 25 mM Na-HEPES, pH 7.5, 5% (w/v) glycerol and 2 mM DT. The protein peak eluted at 350 mM NaCl was concentrated using the pressure concentrator

(Amicon, 500 kDa MWCO). The ACDS complex was aliquoted (ca. 250 µL), frozen and stored in lN_2. Finally, the aliquots (with a total volume of ca. 500 µl) were thawed and applied to a Sepharose 6B-CL (26 mm × 640 mm in XK 26 column) equilibrated with 25 mM Na-HEPES pH 7.5 with either 150 mM $(NH_4)_2SO_4$ or 100 mM NaCl. Protein fractions corresponding to a high-molecular weight and containing stoichiometric subunit composition as determined by SDS-PAGE were collected and immediately prepared for negative stain or cryogenic electron microscopy (cryo-EM) analysis (2.9).

2.5.3 $\alpha_2\varepsilon_2$-SUBUNITS FROM *M. barkeri* (*Mb*$\alpha_2\varepsilon_2$) AND *A. fulgidus* (*Af*$\alpha_2\varepsilon_2$)

Purified *Mb*ACDS was diluted with 50 mM Tris-HCl pH 7.5 to a final concentration of 3 – 4 mg/mL (ca. 4 mL total volume) and treated with α-chymotrypsin (*Mb*ACDS to α-chymotrypsin final concentration ratio of 30:1) for 1 hour at room temperature or over night at 4°C. After chymotrypsin incubation, the mixture was applied to an anion-exchange column (Source 30Q). The protein was eluted at a flow rate of 1 mL/min with a linear gradient of 0 – 1 M NaCl in 50 mM Tris-HCl, pH 7.5. Brown-colored fractions contained *Mb*$\alpha_2\varepsilon_2$-subunit and eluted at 350 mM NaCl. The *Mb*$\alpha_2\varepsilon_2$-containing fraction was subsequently loaded on a Superdex200 Hiload (16 mm × 540 mm in XK 16 column) at 0.5 mL/min equilibrated in 50 mM Tris, pH 7.5, 150 mM NaCl. A single protein peak with an absorption at 410 nm eluted at ca. 66 mL. The fractions were collected and concentrated to approx. 7 mg/mL (Amicon, 50 kDa MWCO), frozen and stored in lN_2.
Af$\alpha_2\varepsilon_2$-subunit was purified in a similar procedure as described for *Mb*$\alpha_2\varepsilon_2$.

2.5.4 F_{420}-REDUCING HYDROGENASE FROM *M. barkeri (Mb*FRH)

10 g of frozen cells (*M. barkeri* MS) were resuspended in ca. 50 mL of 25 mM Na-HEPES pH 7.5 containing 150 mM NaCl, 5 – 7.5% (w/v) glycerol (buffer C). The soluble crude extract was prepared as described for *Mb*ACDS complex (2.5.1) and concentrated to a volume of 20 mL with the pressure concentrator (Amicon, 500 kDa MWCO). Concentrated protein was applied at 2 mL/min to a Sepharose 6B-CL column (1.5.2) equilibrated in buffer C and monitored at 280 and 410 nm. 10 mL-volume fractions were collected, and analyzed for reduction activity. Fractions with the highest rate of H_2-dependent reduction of oxidized methyl viologen (MV) were pooled and concentrated to approx. 7 mg/mL. The sample was frozen in aliquots in lN_2 (as above).

2.5.5 CODH-II FROM *C. hydrogenoformans* (*Ch*CODH-II)

Heterologously expressed and purified *Ch*CODH-II was kindly provided by Dr. Jae-Hun

Jeoung (Strukturbiologie/Biochemie, Humboldt Universität zu Berlin).

2.6 PROTEIN CHARACTRIZATION

2.6.1 PROTEIN CONCENTRATION AND PURITY

The protein concentration was quantified using a Direct Detect infrared spectrometer (Merck Millipore, Danvers, USA). The purity of the protein samples was determined by discontinuous sodium dodecyl sulfate polyacrylamide gel electrophoresis (SDS-PAGE) as described by Laemmli (*106*) (Tab. 8).

Table 8. SDS-PAGE components.

12% resolving gel	375 mM Tris-HCl, pH 8.8 12% (v/v) acrylamide 0.1% (w/v) SDS 0.08% (v/v) N,N,N',N'-tetramethylethylenediamine (TEMED) 0.05% (w/v) ammoniumpersulfate (APS)
5 % stacking gel	125 mM Tris-HCl, pH 6.8 5% (v/v) acrylamide 0.1% (w/v) SDS 0.08% (v/v) TEMED 0.05% (w/v) APS
5-fold loading dye	200 mM Tris-HCl, pH 6.8 8%(w/v) SDS 0.5% (w/v) bromophenol blue 40%(v/v) glycerol 400 mM DTT
10-fold running buffer	144 g 86% (v/w) glycerol 30 g Tris base 10 g SDS ad 1000 ml dH_2O
staining solution	0.025% (w/v) Coomassie brilliant blue G-250 10% (v/v) acetic acid
destaining solution	10% (v/v) acetic acid

The sample was mixed with loading dye, denatured by boiling and loaded on the gel. The gel was run at 175 V for 1.5 hours and was subsequently stained and destained with the

corresponding solutions.

2.6.2 UV-VIS SPECTROSCOPY

UV-Vis spectra were recorded with an Agilent 8453 photodiode array spectrophotometer (Agilent Technologies, Santa Clara, California). Spectra were reordered in black-walled quartz cuvettes with a 1 cm path length.

2.6.3 CO-/H_2-DEPENDENT METHYL VIOLOGEN REDUCTION

CO- and H_2-dependent methyl viologen (MV) reduction activity was assayed using CO and H_2 as electron donor, respectively. The procedure was previously described by Svetlitchnyi *et al.* (*46*). 1 mL CO- or H_2-saturated buffer containing 50 mM Na-HEPES, pH 7.5, 100 mM NaCl, and 20 mM MV was aliquoted in a screw-cap quartz cuvette and sealed with a silicon septum. The cuvette was flushed with N_2 prior usage. Reactions were initiated by injecting protein with a gas-tight Hamilton syringe and monitored by the increase in absorbance at 578 nm using an Agilent 8453 spectrophotometer with the kinetic mode. One unit (U) of CO- or H_2-oxidation activity is defined as the reduction of 2 µmoL of MV per minute, which is equivalent to 1 µmoL of CO- or H_2-oxidation per minute. The CO- or H_2-dependent reduction activity is calculated from following equation (Eq. 6):

$$\frac{U}{mL} = \left(\frac{\Delta A}{2 \times \varepsilon_{578} \times d}\right) \times D \qquad \text{(Eq. 6)}$$

where ΔA is the initial slope of absorption change at 578 nm per minute; ε_{578} = 9.7 $mM^{-1}cm^{-1}$ is the molar extinction coefficient of MV at 578 nm; d = 1 cm is the path length of the cuvette and D is the total dilution factor of enzyme.

2.6.4 MICHAELIS-MENTEN KINETICS

The kinetic data was recorded with Agilent 8453 spectrophotometer. To determine the Michaelis-Menten (MM) parameters (K_M and V_{max}) for FAD and FMN time-dependent increase of the absorbance at 304 nm was monitored at various flavin concentrations at 37°C in CO-saturated buffer D (50 mM Na-HEPES pH 7.5, 150 mM NaCl). Eight data points were collected for FAD and FMN ranging from 0 to 1 M. Gas-tight quartz cuvettes and syringes were used for the assays. The reaction was initiated by injecting 10 µL of the enzyme (corresponding to a final concentration (c_p) of 1.3 µg/mL for *Ch*CODH-II, 0.9 µg/mL for *Mb*$a_2\varepsilon_2$-subunit, 2.0 µg/mL for *Af*$a_2\varepsilon_2$-subunit, and 4.3 µg/mL for *Mb*ACDS

complex) into 1 mL of reaction buffer. Each enzyme was stoichiometrically reduced with freshly-prepared DT for at least 30 min prior to injection. The initial rates (Δ_i) were obtained by linear regression fitting of the initial portions of each experimental recording at varying flavin concentrations. Specific activity (A_{sp}) was calculated using the equation 7 (Eq. 7):

$$A_{\mathrm{sp}} = \frac{\Delta_{\mathrm{i}}}{\varepsilon_{340} \times c_{\mathrm{p}}} \qquad \text{(Eq. 7)}$$

with A_{sp} in U/mg, Δ_i in min^{-1} and c_p in mg/mL. The molar extinction coefficients at 304 nm (ε_{304}) of FAD (642 $M^{-1} cm^{-1}$) and FMN (1068 $M^{-1} cm^{-1}$) were determined at 37°C in CO-depleted buffer D based on the Beer-Lambert law (Fig. S1). The K_M and V_{max} values for FAD and FMN were determined by fitting a hyperbolic curve of A_{sp} against flavin concentrations using the MM equation by GraphPad Prism 8 (graphpad.com) for each sample. The measurements were repeated in triplicate.

The turnover number (k_{cat}) was calculated using the equation 8 (Eq. 8):

$$k_{\mathrm{cat}} = \frac{V_{\mathrm{max}}}{c_{\mathrm{cs}}} \qquad \text{(Eq. 8)}$$

with k_{cat} in s^{-1}, V_{max} in U/mg, c_{cs} (catalyst site concentration) in g/mol. The c_{cs} for *Af*$a_2\varepsilon_2$- and *Mb*$a_2\varepsilon_2$-subunits were approximated to 110 kg/mol. The c_{cs} for minimal structural unit of *Mb*ACDS (αεßδγ) was approximated to 260 kg/mol.

The specificity constant (k_{eff}) was calculated using the equation 9 (Eq. 9):

$$k_{\mathrm{eff}} = \frac{k_{\mathrm{cat}}}{K_{\mathrm{M}}} \qquad \text{(Eq. 9)}$$

with k_{eff} in $s^{-1}\mu M^{-1}$, with k_{cat} in s^{-1} and with K_M in µM.

2.7 X-RAY CRYSTALLOGRAPHY

All proteins were crystallized at 18°C in an anoxic glove box. Initial crystallization screening was carried out using the siting-drop vapour diffusion method in 96-well plates (Swiss 96-well MRC-Plate, Jena Bioscience) against the following commercial screens: JCSG, ProPlex, Structure Screen 1 & 2, Morpheus (Molecular Dimensions, UK) and PEG/Ion HT (Hampton Research, USA). Drops (1 µL) were set up with the Oryx Nano crystallization robot (Douglas Instruments, UK) with a protein to reservoir solution ratio of 1:1. Suitable crystallization conditions were subsequently optimized by hanging-drop (using a drop size of 4 µL with reservoir solution of 600 µL) and sitting-drop (drop size of 3 µL with reservoir solution of 200 µL) vapour diffusion in 24- (Greiner Bio-One, Germany) and 48-well plates (Swissci 48-well MRC Maxi Optimization plate, Molecular Dimensions, UK), respectively.

2.7.1 CRYSTALLIZATION

2.7.1.1 *Mb*$\alpha_2\varepsilon_2$-SUBUNIT

The *Mb*$a_2\varepsilon_2$-subunit was crystallized by sitting-drop vapour diffusion in 0.1 M phosphate/citrate buffer, pH 4.2 – 4.8, 20 – 40% (v/v) ethanol, 5% (w/v) PEG 1000. 1.5 µL of 8 mg/mL protein sample was mixed with 1.5 µL of reservoir solution. Crystals appeared within 7 days and were flash cooled in lN_2 using 15% (v/v) 2,3-butanediol as a cryoprotectant.

2.7.1.2 *Af*$\alpha_2\varepsilon_2$-SUBUNIT

Crystals were grown by sitting-drop vapour diffusion in 0.1 M N-cyclohexyl-3-aminopropanesulfonic acid (CAPS), 40% 2-Methyl-2,4-pentanediol (MPD), 5 mM DT. 1 µL of 8 mg/mL protein was mixed with 1 µL of reservoir solution. A single crystal appeared within 18 days and was harvested as in (2.7.1.1).

2.7.1.3 *Mb*FRH

Prior crystallization of hydrogenase-enriched sample, sample buffer was exchanged into 50 mM Tris-HCl, pH 7.5 with 100 – 150 mM NaCl using sephadex-G25. Crystals were grown by hanging-drop vapour diffusion in 0.1 M Tris-HCl, pH 7.8 – 8.5, 15 – 40% (v/v) MPD. 2.0 µL of 7 mg/mL protein was mixed with 2.0 µL of reservoir solution. Crystals appeared within 2 to 4 days and were harvested as in (2.7.1.1).

2.7.2 CRYSTAL HANDLING

2.7.2.1 XENON AND CO DERIVATIZATION

*Mb*FRH crystals were exposed to 20 – 30 bar of Xe pressure for 15 min using a pressurized chamber at BESSY-II (Helmholtz-Zentrum Berlin, Germany) (*107*). Crystal mounting and transfer into the pressurized chamber was done under oxic conditions.

For CO derivatization, hydrogenase crystals were transferred to a 48-well sitting drop crystallization plate filled with 10 µL of reservoir solution per well and covered with scotch tape to prevent dehydration. The plate was placed inside a custom gas-tight screw box (Plexiglas, dimensions 15 cm × 15 cm × 5 cm) and incubated with 100% CO under 1.5 bar for 30 h in the dark. Crystals were harvested as in (2.7.1.1).

2.7.2.2 MV-MEDIATED REDUCTION WITH H_2

*Mb*FRH crystals were transferred into 10 µL of reservoir solution containing 10 mM oxidized MV as a redox mediator and incubated with 100% H_2 at 1.5 bar for 48 hours in a custom gas-tight screw box as in (2.7.2.1). Crystals were harvested as in (2.7.1.1).

2.7.3 DATA COLLECTION AND PROCESSING

Native (λ = 0.918 Å) and anomalous (λ = 1.732 Å; λ = 1.900 Å) X-ray diffraction data were collected at 100 K at beam lines of BL 14.1/14.2 at BESSY-II. To confirm the positions of Fe ions, an anomalous dataset was collected at the K-absorption edge of Fe (λ = 1.732 Å) for the calculation of an anomalous Fourier difference map. To reveal the positions of S and Xe atoms, data were collected at a wavelength of 1.900 Å.

Diffraction datasets were integrated and scaled with X-ray Detector Software (XDS via the GUI XDSAPP) (*108*). Initial phasing for all structures was performed by molecular replacement with Phaser (*109*), using available crystal structures of *Mm*FRH (PDB entry: 4OMF (*77*)) and *Mb*$\alpha_2\varepsilon_2$ (PDB entry: 3CF4 (*18*)) as search models. Iterative cycles of model building and refinement were performed with Coot (*110*). Positional, temperature factor and occupancy refinements were carried out with PHENIX (*111*) or REFMAC5 (*112*).

Initially the ligand-free models were refined in PHENIX (*111*). Subsequently, metal ligands ([4Fe4S] clusters, cluster C [Ni4Fe4S] for *Mb*$\alpha_2\varepsilon_2$- and *Af*$\alpha_2\varepsilon_2$-subunits, and [NiFe]-active site $NiFe(CN)_2(CO)$ for *Mb*FRH) were modeled and subjected to restrained refinement, during which the atomic positions, individual temperature factors and occupancies were adjusted. Chemical restraints such as bond lengths and bond angles

were generated with REFMAC5 (*112*).

The F_o-F_c omit electron density observed between the Ni and Fe atoms of the cluster C in the *Af*$\alpha_2\varepsilon_2$-subunit was refined as two alternative models of either CO_2 or Ni-bound CO with exogenous Fe-bound hydroxyl group. The ligand binding geometry was compared to the previously-reported CO_2-bound and cyanide-inhibited cluster C of *Ch*CODH-II homologs (PDB entries: 3B52 (*39*) and 5FLE (*42*), respectively).

Similarly, the observed F_o-F_c electron density above the Ni atom of in the CO-derivatized *Mb*FRH crystal structure was modeled as Ni-bound CO. The CO binding geometry was compared to the previously reported CO-inhibited NiFe hydrogenase structures from *D. vulgaris* (PDB entries: 1UBH, 1UBJ, 1UBK, 1UBL, 1UBM, 1UBO, 1UBR, 1UBT, 1UBU (*103*)) .

Data and final refinement statistics are reported in Table S1 – S3. All figures were prepared using Pymol and Chimera (*113*).

2.7.4 ACCESSION NUMBERS

The coordinates of the as-isolated, xenon and CO-derivatized *Mb*FRH structures have been deposited to the PDB under accession codes 6QGR, 6QII and 6QGT respectively.

2.8 EPR, IR AND RR SPECTROSCOPY

EPR, IR and RR measurements were conducted by Christian Lohrent (Institut für Chemie, Technische Universität Berlin).

2.9 TRANSMISSION ELECTRON MICROSCOPY

2.9.1 SPECIMEN PREPARATION

Samples were prepared using two different methods. In the first method, ca. 400 µL of 7 – 8 mg/mL ACDS-containing fractions collected from the Source 30Q column (denoted as "bound" in Fig. 13B) were applied at a flow rate of 1 – 2 mL/min to a Sepharose 6B-CL column equilibrated in 25 mM Na-HEPES pH 7.5 with either 150 mM $(NH_4)_2SO_4$ (buffer C) or 100 mM NaCl (buffer D). High-molecular weight fractions were collected and analyzed by SDS-PAGE. Fractions with stoichiometric subunit compositions were used immediately for negative stain (NS) electron microscopy (EM) or for unstained cryo-EM. In the second method, approx. 200 µL of ACDS-containing fraction, obtained after Source 30Q, were subjected to density gradient centrifugation. The protein sample was centrifuged in a 10 – 50% glycerol gradient in a SW 60 Ti rotor at 45 000 × *g* (21 000 rpm) for 16 hours at 12°C. The gradient was prepared in buffers C or D with or without reducing agent (with a maximal concentration of 2 mM DT) in a

total volume of 4 mL. After centrifugation, the gradient was harvested in 3 – 4 drop size fractions (approx. 50 µL) by puncturing the bottom of the centrifugation tube with the needle. The brown-colored fraction sedimented at ca. 40% (v/v) glycerol and was buffer exchanged with 1 mL PD-10 desalting columns to reduce the glycerol concentration. The final ACDS sample was subjected to SDS-PAGE analysis to verify stoichiometric subunit compositions and then used immediately for negative stain EM or unstained cryo-EM.

2.9.2 GRID PREPARATION

For NS EM, 5 µL of freshly prepared ACDS complex (0.02 – 0.05 mg/mL) was adsorbed to a glow-discharged carbon-coated 300 mesh copper/rhodium R2/4 grid (Quantifoil Micro Tools GmbH) and incubated for 1 min. The excess buffer was then removed with blotting paper (Whatman; type 4) and stained with 5 µL of 2% (w/v) uranyl acetate. The stain was immediately removed with blotting paper (Whatman; type 4) and reapplied to the grid. This procedure was repeated 5 – 7 times. In the final step, the excess stain was removed as described above, air-dried for 2 – 5 mins and subsequently imaged.

For unstained cryo-EM, carbon-coated 400 mesh copper R1.2/1.3 grids (Quantifoil Micro Tools GmbH) were washed in chloroform and thoroughly dried prior to glow discharging. 3.5 µL of freshly prepared ACDS complex (0.05 – 0.1 mg/mL) were applied to a glow-discharged grid, incubated for 45 s, blotted for 2 – 4 s and plunge-frozen in liquid ethane using a Vitrobot (FEI) under aerobic conditions.

2.9.3 DATA COLLECTION

The following data were collected at the Max Plank Institute for molecular genetics (MPI, Berlin, Germany) in the research group of Dr. Thorsten Mielke, at the Institute of Cancer Research (ICR, London, UK) in the research group of Dr. Edward Morris, and at the Central European Institute of Technology in the research group of Dr. Jiří Nováček (CEITEC, Brno, Czech Republic).

NS data were acquired on a Philips Tecnai T12 electron microscope equipped with a LaB_6 filament and operated at an acceleration voltage of 120 keV (MPI, Berlin). Images were acquired at a nominal magnification of 42 000 x with a defocus range between -1.0 and -4.5 µm. The pixel size of the unbinned images was 2.65 Å/pix at the specimen level. Automatic data collection was performed using program Leginon (*114*). Cryo-EM micrographs were collected at -178°C on a FEI Tecnai TF20 electron microscope (ICR, London) operated at 200 keV and recorded at a 63 000 × magnification, resulting in a pixel size of 1.73 Å/pix at specimen level. The final data set consisted of 162

micrographs. The first set of cryo-EM movies (set 1) were collected at lN_2 temperature on a FEI Tecnai G2 Polara Microscope (MPI, Berlin) operating at 300 keV and equipped with a K2 Summit direct electron detector (Gatan) at nominal magnification of 31 000 x and a defocus range of -1.0 to -2.5 µm, resulting in an unbinned pixel size of 0.625 Å/pix at the specimen level. Twenty-five movie frames were recorded under low dose conditions with a total dose of ~25 e^{-} $Å^{-2}$. Data were collected automatically using Leginon (*114*). A second set of cryo-EM movies (set 2) were collected at lN_2 temperature on a FEI Titan Krios electron microscope with a Falcon II direct electron detector operating at 300 keV (CEITEC, Brno). Data were collected at 59 000 x magnification with a defocus range of -1.5 to -2.5 µm resulting in an unbinned pixel size of 1.38 Å/pix at the specimen level. Thirty-two movie frames were recorded during a total exposure time of 2 s with a corresponding dose of ~55 e^{-} $Å^{-2}$.

2.9.4 IMAGE PROCESSING

Images were processed using RELION 2.0 (*115*), IMAGIC (*116*) and EMAN2.12 (*117*). CTF parameters were estimated using CTFFIND4 (*118*), and micrographs were selected based on the quality of their power spectra. Movie stacks were corrected for beam-induced motion using 25 (set 1) or 30 (set 2) image frames with MotionCorr (*119*).

Negatively stained particles were located semi-automatically using RELION (*120*) or BOXER (EMAN2 software package (*117*)). For particle picking in RELION, a small subset of ca. 2000 particles were selected manually and subjected to reference-free 2D classification. Resultant 2D class averages were low-pass filtered to 20 Å and used as templates for automated particle picking with angular sampling of 10° and a picking threshold of 0.4. A total of ca. 80 000 particles were extracted at a 250 pix (unbinned; 2.56 Å/pix) or 168 pix (binned; 3.93 Å/pix) frame size. The binned particle stack was subjected to reference-free 2D classification with RELION and EMAN2 independently. For *ab initio* 3D model generation, fourteen representative 2D class averages generated in RELION with defined structural features observed independently in both RELION and EMAN2 were selected and imported into IMAGIC. The initial 3D model was generated with *C*1 symmetry by angular reconstruction (using random start-up). The correlation between forward projections of the 3D reconstruction and the associated 2D class averages were monitored. The generated 3D reconstruction was further refined by iterative application of projection-matching algorithms until convergence with the initial 3D volume reference. Finally, the resulting 3D volume was imported into RELION and

further subjected to 3D classification against a stack of 80 000 particles. Particles that corresponded to the highest quality 3D class averages were selected, unbinned and used in the final 3D auto-refinement. The resulting low-resolution 3D model was employed for subsequent cryo-EM data processing.

The cryo-EM data were processed as follows. First, particles were located manually in RELION and extracted at a 136 pix (binned, 4.92 Å/pix), 268 pix (binned, 2.48 Å/pix) or 240 pix (binned; 2.76 Å/pix) frame size from the individual micrographs or movie frames (set 1 and 2), respectively. The resulting particle stacks were individually subjected to reference-free 2D classification. 3D classification using the 3D reconstruction from negative stain as a reference was performed on the cleaned particle stacks. Misaligned particles were removed. Finally, binned and unbinned particles that contributed to the 3D class averages with highest protein integrity were selected and used in the final refinement. Additionally, particles extracted from the movie frames of set 1 and 2 were scaled, subsequently merged and also subjected to the 3D model generation described above. Average resolutions were calculated using the FSC 0.143 criterion.

3 RESULTS AND DISCUSSION

3.1 CULTIVATION OF *M. barkeri*

M. barkeri str. Fusaro and *M. barkeri* MS grew on sodium acetate and MeOH as the sole energy and carbon source respectively under batch-type cultivation conditions. The optimal growth of both *Methanosarcina* strains was observed in slightly modified culture medium previously described by Hippe *et al*. (*121*). The cell growth was monitored by measuring gas production. Consistent with previous observations (*122, 123*), MeOH is used at a rate 2.5 times higher than acetate (Fig. 12). The cell growth was suspended due to acidification (pH drop to 5.5) or alkalinization (pH increase to 8.0) of the media during cultivation on MeOH or acetate, respectively.

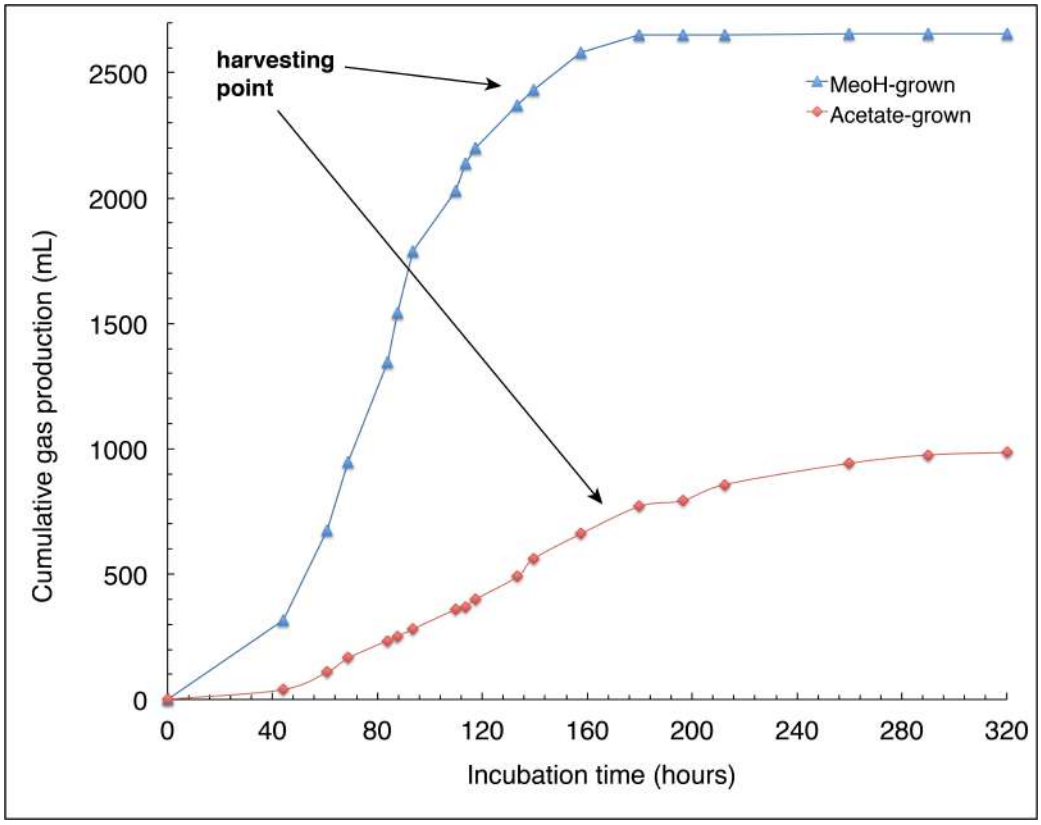

Figure 12. Cumulative gas production during growth of *M. barkeri* on acetate and MeOH. *Methanosarcina* cells grown in 500 mL cultures on 250 mM MeOH (blue line) and 100 mM acetate (red line) as substrate. Cells were harvested in late exponential phase as indicated by arrows.

Cells were harvested under anoxic conditions during late exponential phase, which was observed after 5 – 6 days for MeOH- and after 7 – 8 days for acetate-grown *Methanosarcina,* respectively. The cell yield was 2.5 g wet cell pellet per 1 L MeOH-

media and 0.7 g wet cell pellet per 1 L acetate-media.

Independent of the substrate, two cell phenotypes were observed during cultivation: film and cell packages. The difference in morphology did not affect cell growth and lead to a comparable quality of isolated protein, and thus this observation remained to be investigated.

To ensure the purity of the cell culture, small aliquots of the cell suspension were investigated microscopically once a month. Due to the observed shape (cuboidal arrangement of eight cocci), size and the lack of the flagellar motility (*124*), *Methanosarcina* could be easily distinguished from typical bacterial contaminations (e.g. *E. coli*, *Clostridia* sp.) (Fig. S2). Any contaminated cultures were discarded. Due to the cell size and lack of agitation during the growths, *Methanosarcina* cells settled to the bottom of the cultivation bottle within couple of hours after inoculation. In the event of contamination, the media retained an observable turbidity, due to the inability of the light bacterial contaminants to sediment. The culture turbidity was also used as an additional criterium for purity control for the archaeal cell cultures.

3.2 STRUCTURAL INVESTIGATION OF ACDS COMPLEX

Both ACDS complexes from *M. barkeri* (*Mb*ACDS) and *A. fulgidus* (*Af*ACDS) were targets for structural investigation by transmission electron microscopy (TEM). The most promising results were obtained for *Af*ACDS complex and will be discussed in the following chapters.

3.2.1 PROTEIN PURIFICATION

The *Af*ACDS complex was purified in a three-step procedure: 1) size exclusion chromatography (SEC) of the soluble crude cell extract on a preparative Sepharose 4B-CL column, 2) anion exchange chromatography (AEC) of the *Af*ACDS-enriched fraction on a Source 30Q column and 3) SEC of the bound protein fraction on a preparative Sepharose 6B-CL column (Fig. 13). The elution profiles were monitored at 410 nm to identify proteins containing iron-sulfur cluster. Initial SEC revealed three broad protein peaks. Activity assays were used to identify the fractions containing ACDS complex, using the oxidoreductase activity to couple CO oxidation to reduction of oxidized MV. Fraction 2, eluted between 650 mL and 1050 mL (Fig. 13A), was able to reduce MV in the presence of CO (approx. 10 U/mg) and was further subjected to AEC (Source 30Q). The *Af*ACDS-containing fraction (termed "bound"; Fig. 13B) was recovered by gradient elution with NaCl. The recovered fraction demonstrated higher CO-dependent MV reducing activity (approx. 15 fold) as compared to the flow through.

Finally, SEC (Sepharose 6B-CL) of the *Af*ACDS-containing fraction from AEC (Source 30Q) revealed a peak around 135 mL with a preceding sharp peak and a following substantial tail indicating the presence of high molecular weight aggregates in the void volume (approx. 110 mL) and low molecular weight protein components respectively (Fig. 13B). The final ACDS fraction was collected around the peak of 135 mL ± 25 mL for further biochemical and structural studies. SDS-PAGE of the purified *Af*ACDS complex revealed five different protein bands, four of which corresponded to the expected molecular weight of α (89 kDa), ß (72 kDa), δ (50 kDa) and γ (49 kDa) subunits of the previously isolated *Af*ACDS complex *(55)*. Peptide mass fingerprinting (PMF) was used to unambiguously identify the polypeptides as the subunits of ACDS complex. The visualization of the ε-subunit by SDS-PAGE, which was later detected by X-ray analysis, was likely hindered due to a low protein concentration and Coomassie stain sensitivity. The isolated ACDS complex was approx. 95% pure and the overall purification yield was 0.1 mg protein per 1 g wet cell paste.

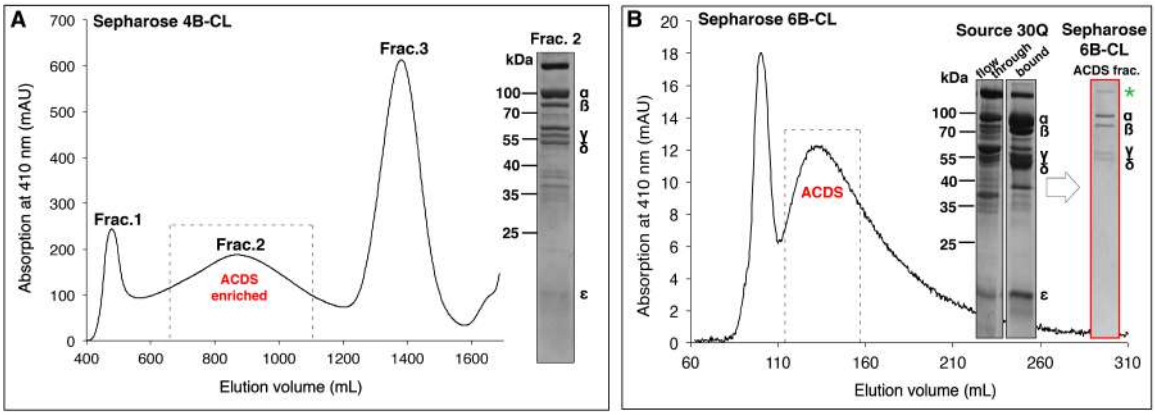

Figure 13. Purification of *Af*ACDS. (A) First SEC with Sepharose 4B-CL. Protein content of the ACDS-enriched fraction (Frac. 2) was analyzed by 12% SDS-PAGE (right inset). (B) Second SEC with Sepharose 6B-CL. The protein purity of the final SEC and the preceding step (AEC on Source 30Q) was analyzed by 12% SDS-PAGE (right inset). Samples for SDS-PAGE were prepared according to the procedure of Laemmli (*106*) prior to gel electrophoresis. Elution profiles of A and B were recorded at 410 nm (black solid line). The dash lines indicate the *Af*ACDS containing fractions collected at different stages of purification. Protein band marked with "*" (Fig. 13B, right inset) indicates the uncharacterized protein, which was always co-purified with *Af*ACDS complex.

For a complete product analysis, the high molecular weight protein (ca. 120 kDa) that co-purified with the *Af*ACDS complex (Fig. 13B, inset) was identified by PMF as an uncharacterized protein of unknown function (UniProt entry O29316), which is highly abundant in Archaeoglobales (p-blast).

The UV-VIS absorption spectra revealed two absorption maxima around 320 nm and 410 nm, indicating the presence of [FeS] clusters in purified *Af*ACDS complex (Fig. S3).

3.2.2 VIZUALIZATION OF THE ACDS COMPLEX BY ELECTRON MICROSCOPY

Purified *Af*ACDS complex was visualized by negative stain (NS) electron microscopy (EM) using 2% uranyl acetate stain on carbon-coated copper/rhodium grids (Fig. 14A), as well as by cryogenic EM (cryo-EM) as a vitrified-hydrated sample on carbon-coated copper grids (Fig. 14B). As visualized by both techniques, isolated *Af*ACDS complex was observed to be a homogenously globular particle without preferred orientations. On average, 80 or 40 particles were imaged per one NS and one cryo-EM micrograph, respectively.

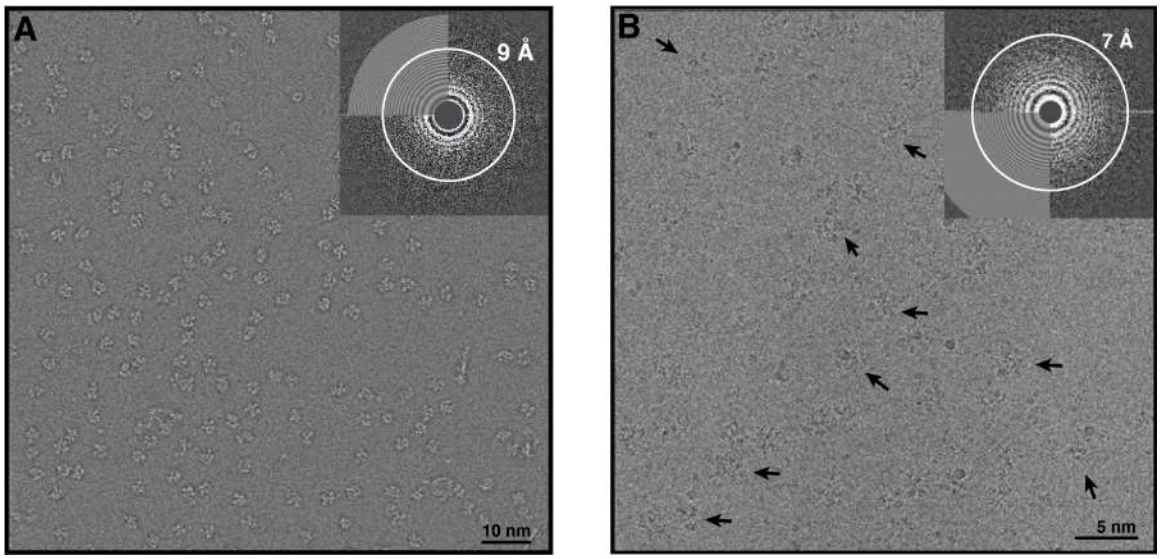

Figure 14. Visualization of ACDS complex by TEM. Negatively stained and band-passed micrograph (A) and cryo-electron image (B) of the purified *Af*ACDS complex were imaged at -3.0 µm and -2.0 µm defocus respectively. Corresponding power spectra are shown in insets. Arrows indicate the location of the intact ACDS complex.

3.2.3 SAMPLE STABILITY DURING NEGATIVE STAINING AND CRYOGENIC VITRIFICATION

Despite the oxygen sensitivity of the sample, no visual difference in particle appearance was observed between the micrographs that were prepared under aerobic or anaerobic conditions. Significant protein heterogeneity was identified in both the frozen-hydrated state and the negatively stained sample. Integrity of the purified *Af*ACDS complex was highly dependent on the freezing conditions (Fig. S4A) and the methods used for protein concentration (Fig. S4B). High molecular weight protein aggregates were detected in up to 20% of collected micrographs (Fig. S4C). Imaging of the fully assembled enzyme complex was also highly dependent upon ice thickness. Intact *Af*ACDS complex was not observed within thin ice regions and only smaller protein components, which correspond to individual complex subunits, were identified (Fig. S4D; 3.2.7).

The heterogeneity of the particles was presumed to be related to sample stability. Sample instability could originate from the negative staining procedure or vitrification (*125-128*), or the heterogeneity could be reflective of the protein solution state under our chosen conditions. Standard negative staining protocols often produce artifacts induced by stain-protein interactions (*129, 130*). Binding of the uranyl ions to the protein could trigger sample aggregation (*131*) and the specimen dehydration could contribute to particle instability and its subsequent decomposition (*129, 130, 132*). However, slight modification of the standard staining procedure, such as repetitive (up to 10) quick short

stain application, resulted in multiple evenly-distributed stain layers that masked small protein debris (Fig. 14A). When same sample was stained with one application of 5 µL uranyl acetate for 45 sec, the subcomplex components could be observed (Fig. S4A).

An additional common artifact is sample flattening (*132*). Therefore, the negatively-stained images may not reflect the particle shape in solution or *in vivo*. In contrast, vitrification methods for cryo-EM present much fewer artifacts by preserving the macromolecules in a closer-to-native hydrated conditions (*127, 133*). However, protein denaturation in vitrified samples has been observed as a function of the particle location on the grid, at the air-water interface (*128, 134*), from radiation damage (*135*) or due to rigorous blotting with filter paper (*136*).

The heterogeneity of the complexes observed by TEM was reminiscent of the elution profile of the complex from the final SEC step, which revealed the tendency of the *Af*ACDS protein to aggregate (ca. 25% of the total protein eluted in the void volume) and decompose (indicated by the peak tail containing low molecular weight compounds) (Fig. 13B). The results of the chromatographic analysis suggest that the optimal purification conditions required for the stability of the isolated *Af*ACDS complex in solution have not yet been found.

Several crosslinking attempts with glutaraldehyde to stabilize the *Af*ACDS complex were unsuccessful. Cross linker concentrations below 0.08% (v/v) had no apparent effect on the complex stability, neither affecting visual particle integrity nor leading to higher data quality and higher resolution of the three-dimensional reconstruction. Concentrations of glutaraldehyde above 0.1% (v/v) resulted in intramolecular crosslinking, leading to protein aggregation (using 0.05 – 2 mg/mL *Af*ACDS). The method of gradient fixation (*137*) also did not improve the complex stability.

3.2.4 DATA PROCESSING: NEGATIVE STAINING

3.2.4.1 REFERENCE-FREE 2D CLASSIFICATION

From a total of 2880 negatively stained micrographs, ca. 1000 micrographs within the defocus range of -1 to -3 µm were selected for further processing based on the overall image quality (e.g. no major protein aggregates, even staining, Thon ring isotropy). A total of ca. 80 000 particles were picked from these 1000 micrographs and further subjected to reference-free 2D classification in RELION (*115*). Twenty-five to thirty cycles of iterative 2D classification were used in order to yield a final data set of approx. 40 000 single particles into twenty-four 2D class averages (Fig. 15A). 2D classes with

similar features were observed when same data set was independently processed with EMAN2 (Fig. 15B) (*117*). The consistency of the classification results between the two processing strategies supports the observed classes.

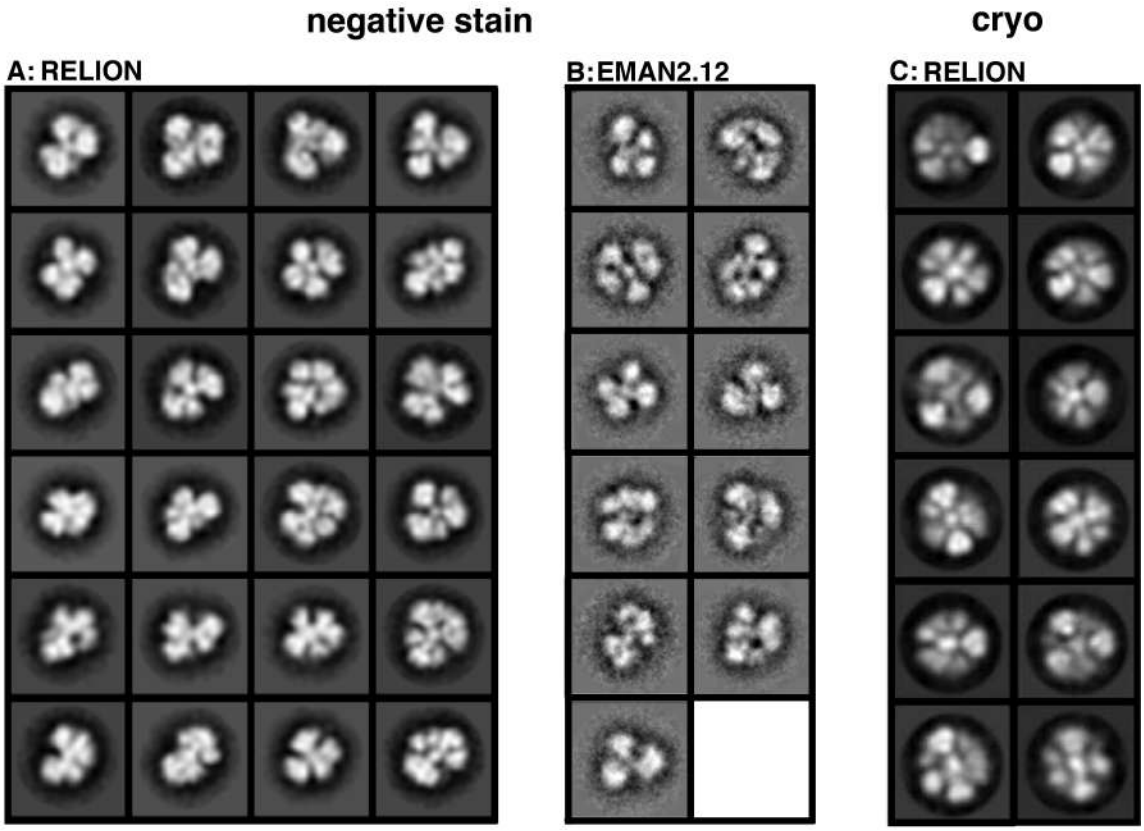

Figure 15. Reference-free 2D classification of the negatively stained and vitrified *Af*ACDS complex. Representative 2D class averages were obtained by reference-free 2D classification of the negatively stained data set of 40 000 particles and cryo-EM data set of 12 000 particles performed independently with RELION (A, C) and EMAN2 (B).

3.2.4.2 *Ab initio* 3D RECONSTRUCTION

The three-dimensional structure of the *Af*ACDS complex was determined to 29 Å by single-particles analysis (*138-140*). The initial 3D model was created in IMAGIC (*116*) from the fourteen highest quality 2D class averages of negative stained particles (Fig. 16A) using angular reconstitution (*141*). The model was further refined by an iterative projection matching procedure (Fig. 16B) (*142*). The final resolution of the density map was 34 Å, as estimated by Fourier Shell Correlation (FSC) with a cutoff value of 0.143 (*143*) (data not shown). The forward projections of the initial reconstruction corresponded well to the associated 2D classes (Fig. 16A). The initial reference may only need to resemble the true structure, thus some disagreements between 2D class averages and reprojections were tolerated. Eigenimages of the unaligned data set of 40 000 particles

exhibited 3-fold, 4-fold and 5-fold symmetry (Fig. S5), however the reconstructions with highest correlation between 2D class averages and reprojections were achieved without imposed symmetry (*C1*).

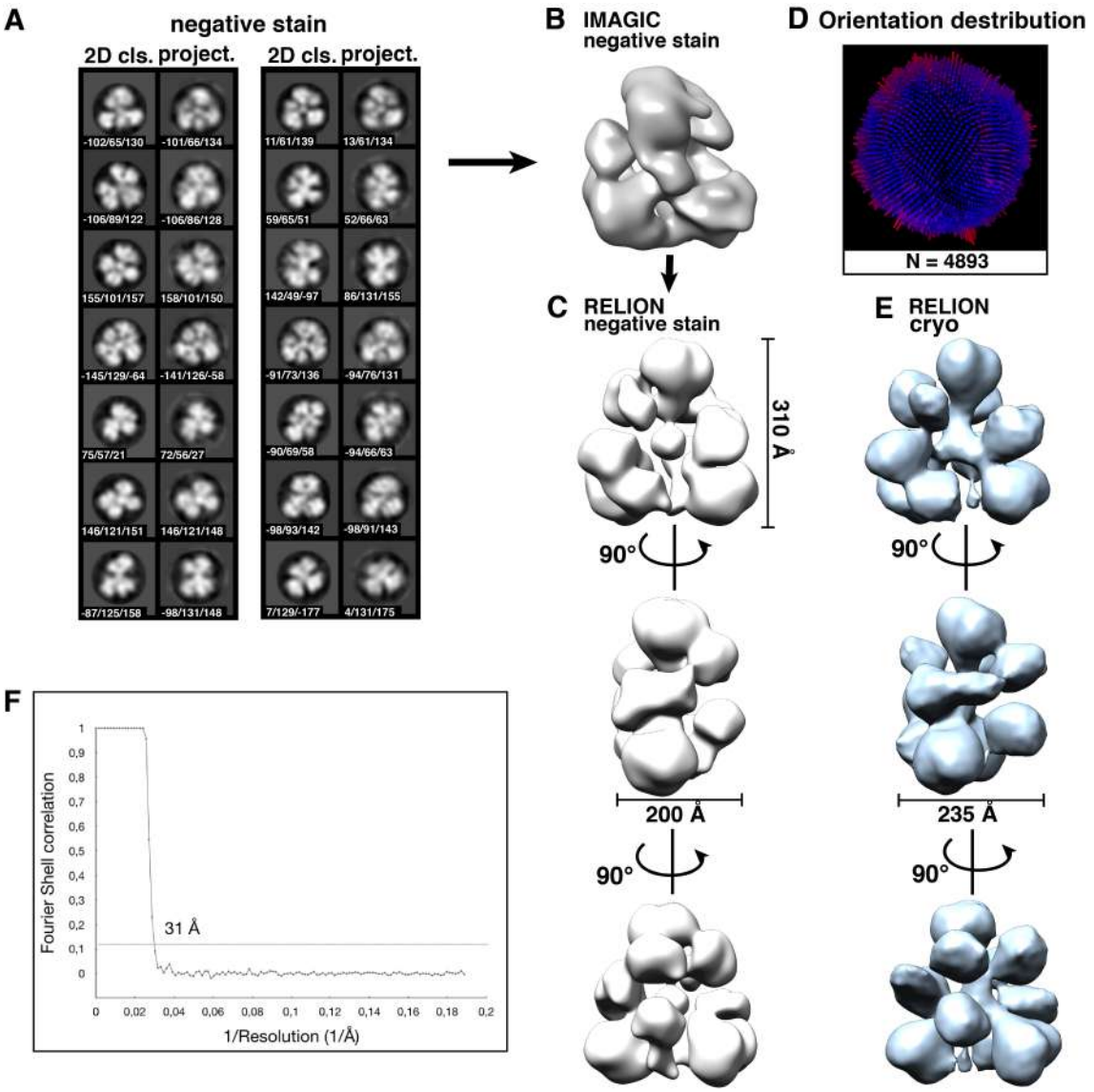

Figure 16. *Ab initio* 3D reconstruction. (A) Representative NS 2D class averages and corresponding reprojections of the initial 3D reconstruction after final refinement in IMAGIC (*116*). Numbers represent the assigned Euler angles. (B) Initial 3D reconstruction without imposed symmetry (*C*1) after angular refinement in IMAGIC (*116*). (C) Different views of the NS density map reconstructed from ca. 5000 sorted particles after 3D classification of the entire particle set (80 000 particles) in RELION (*115*). (D) Euler angle distribution for the final 3D reconstruction from 4893 negatively stained particles. (E) Different views of the cryo 3D reconstruction generated from ca. 6500 sorted particles with NS map as reference in RELION (*115*). (F) FSC curves with a cutoff value of 0.143 indicated the estimated resolution of 31 Å from the refinement of the cryo-3D reconstruction.

In attempt to reduce heterogeneity and improve the resolution, the initial 3D reconstruction (Fig. 16B) was used as a reference for 3D classification in RELION (*115*), during which 80 000 particles were split into 5 classes (Fig. S6). Each 3D class contained similar numbers of particles (ca. 15 000 ± 2000) but each class average differed in overall appearance. The distinction between "good" and "bad" classes was distinguished by applying available structure-related information, since no reference structure has been reported so far. The ACDS complex consists of three distinct catalytic blocks (CODH, ACS and CoFeSP+MeTr), each carrying out a partial reaction of the reversible acetyl-CoA synthesis (*19*) and present in equimolar amount as demonstrated by SDS-PAGE (Fig. 13B). The CODH subunit is represented by $\alpha_2\varepsilon_2$-heterodimer with *C*2 symmetry (*18*) (1.2.5), which could potentially restrict the symmetry-related interaction with other subunits. Thus, some degree of symmetry for the entire ACDS complex is expected. Based on the estimated molecular weight of the ACDS complex (*17, 55*) and the results of proteolytic digestion (*19*), possible subunits arrangements are as follows: an octamer of pentamers $(\alpha_2\varepsilon_2)_4$-$ß_8$-$(\delta\gamma)_8$ or hexamer of the pentamers $(\alpha_2\varepsilon_2)_3$-$ß_6$-$(\delta\gamma)_6$. These arrangements would contain 3-fold or 4-fold symmetry, which agree with the eigenimage analysis of the unaligned particles (Fig. S5) and to the initial assumption of the intrinsic symmetry of the ACDS complex.

Given the symmetry criteria, particles in class 3A (Fig. S6) were selected and further classified using the same initial 3D NS model as a reference (Fig. 16B). During this step, 16 000 particles were split into 3 classes with roughly similar particle numbers. Visual evaluation of the obtained 3D reconstructions lead to the rejection of 67% of particles, comprising classes 1B and 2B (Fig. S6). The remaining 3D reconstruction (class 3B) was low-pass filtered to 50 Å and 3D auto-refined with the corresponding subset of ca. 5000 particles and post-processed in RELION (*115*). The resulting 3D map has dimensions of 300 Å × 270 Å × 200 Å and the volume of ca. 4.5×10^3 Å^3 (Fig. 16C). The final resolution of the density map was 29 Å based on the FSC 0.143 criterion (*143*) (data not shown). The map had a high degree of angular coverage with minor orientation preferences (Fig. 16D). The efficiency of the particle orientation distribution (E_{od}) was 0.65 as calculated by cryoEF (*144*). The calculated point spread function (PSF) had a roughly spherical shape (with a mean resolution of 35 ± 6 Å), indicating uniform coverage of Fourier space. Together, these results indicate that the particles were not preferably oriented on the support film and that most views of the specimen have been imaged.

3.2.5 DATA PROCESSING: CRYO-EM

3.2.5.1 REFERENCE-FREE 2D CLASSIFICATION

Three independent data sets were collected on vitrified protein samples. Cryo-electron micrographs were inspected manually prior to processing. A subset of micrographs that contained isotropic Thon rings extending beyond 8 – 9 Å were selected. Intact particles of the expected size range (ca. 300 – 350 Å) and morphology were manually picked in RELION (*115*). A total of ca. 12 000 (Tecnai TF20 at 200 keV), 24 000 (Tecnai Polara with K2 Summit at 300 keV) and 120 000 particles (Titan Krios with Falcon II at 300 keV) were picked from 162, 550 and 2300 sorted micrographs respectively. Reference-free 2D classification of each independently processed data set contained classes that were similar to the other cryo- (Fig. 15C) and NS class averages (Fig. 15A,B). However, the overall quality of the classes was rather noisy. Compared to the NS data, much fewer reasonable 2D class averages resulted from vitrified particle alignment. Macromolecules prepared by vitrification typically adopt random orientations in the amorphous ice layer, theoretically resulting in more particle projections, while the NS technique tends to induce preferred particle orientations on the carbon film (*145*). However, low signal-to-noise ratio (SNR) of the vitrified sample images (*140*) can hinder the correct image alignment and classification, thus diminishing the number of reasonable 2D classes. The signal recorded from a single cryo-electron micrograph contains on average approx. 90% noise (*146*), which can be diminished upon alignment and averaging over many single particle projections with similar structural features and orientation (*147*). Alignment becomes more difficult with an increase of the noise component, since the SNR of the cross-correlation function used for alignment of noisy single-particle images is directly proportional to the SNR of the images (*148*). Among many factors, ice quality, buffer components and ice thickness can influence SNR. The CTF corrected images of vitrified ACDS complex had, on average, Thon rings that did not oscillate beyond 6 Å (Fig. S7). In contrast, micrographs of vitrified ribosomal complex conducted under similar experimental conditions contained power spectra with average Thon rings oscillating beyond 3 Å (personal communication with Justus Loerke, research group of Prof. Spahn, Charité, Berlin). The signal attenuation of vitrified ACDS micrographs suggests that ACDS complex could be embedded within thick ice.

Poor 2D averaging could result from conformational or compositional sample heterogeneity. Normally, such heterogeneity can be successfully resolved by

classification of sufficiently large datasets (ten to hundred thousands particles), which is routinely performed for ribosomes (*149-151*). However, classification of ca. 144 000 particles (merged data) still resulted in very noisy 2D classes (data not shown), whereas reasonable class averages were obtained by classifying the smallest data set (12 000 particles) (Fig. 15C). These data suggest that the resolution was not limited by particle number, but instead by a feature of the sample, such as subunit heterogeneity or insufficient SNR from e.g. thick ice imaging.

3.2.5.2 3D CLASSIFICATION

Typically, 3D reconstruction of vitrified biological samples utilizes a similar computational reconstruction procedure as described for negatively stained particles. Angular reconstitution with noisy 2D class averages (Fig. 15C) and subsequent refinement by projection matching (*142*) resulted in a very noisy 3D map with poor angular coverage and bad correlation between back projections and associated 2D classes (data not shown).

As discussed in (3.2.5.1), conformational or compositional heterogeneity could contribute to poor classification. Sorting the heterogeneous data into homogeneous subsets would yield more accurate 3D classification, since some structural differences cannot be detected at the 2D level due to the complex protein geometry. To test this approach, cryo-EM data sets were subjected to the 3D classification in RELION (*115*) (individually and merged) using the low-resolution 3D reconstruction (low-pass filtered to 50 Å) from the negatively stained ACDS complex as a reference (Fig. 16C). Depending on the size of the particle stack, three (from 12 000 particles), five (from 24 000 particles) or eight (from 120 000/144 000 particles) classes were generated. Using the same evaluation strategy during 3D classification of the NS data (3.2.4.2), the 3D volumes generated from the cryo data were visually evaluated for reasonable structural features and symmetry. Selected classes were either subjected to further 3D classification to increase the homogeneity of the particle population or 3D auto-refined. All resultant 3D maps strongly resembled the overall topology of the NS reference and had similar dimensions. One of the representative 3D reconstructions was generated from 6500 particles by iterative 3D classification of the initial data set comprising 120 000 particles (Fig. 16E). This 3D reconstruction has a dimensions of 300 Å × 270 Å × 235 Å and the volume enclosed by the surface of approx. 4.9 $\times 10^3$ Å^3 (Fig. 16E). Compared to the dimensions of the NS 3D reconstruction (Fig. 16C), one of the axes is 35 Å longer, possibly indicating sample

flattening of the former. The final resolution of the density map was 31 Å based on the FSC cutoff of 0.143 (Fig. 16F).

Refinement of the NS reference map against cryo-EM data sets of up to 144 000 particles did not improve the resolution, but strongly resembled the initial 3D reference. As already described above, this observation could be the result of very low SNR of the vitrified images. As shown in (*152*), images that consist of pure noise will align to any reference, yielding a 3D reconstruction that reproduces the initial reference ("Einstein from noise"). It is a fair assumption that particles with very a low signal-to-noise ratio could show similar behavior. The other problem could arise from an incorrect initial 3D model. Due to the innate heterogeneity of most biological samples, more then one "true" 3D structure can be assigned to one macromolecular complex. Especially in the case of *de novo* modeling, it is difficult to differentiate between projections from different directions and projections of different 3D structures. It is thus possible that the projections of different structures can be mistakenly combined into one set and used for 3D model generation. Incorrect starting reference could persist during refinement, since most refinement algorithms (e.g. projection matching (*142*)) are local optimizers converging to the nearest local minimum. At this point it is not clear how well the initial 3D reconstruction matches the structure of true protein, since no structure of the ACDS complex is available. One of the most important features of the initial 3D reference is the reliable assignment of Euler angles to the projection images. This procedure can be simplified when Euler angles of projections are specified by experimental set up. Techniques such as random conical tilt (RCT) (*153*), orthogonal tilt reconstruction (OTR) (*154*), and tomography (*155*) attain the relative angular information from multiple imaging of the same particles under several predefined angles.

3.2.6 FITTING OF CODH SUBUNIT

Assuming the accuracy of the obtained 3D reconstruction, fitting individual subunits into the map was challenging, given the resolution. Subunit structures are available from the archaeal and bacterial homologues (*18, 20, 21, 54, 156-158*), but a 3D reconstruction of at least 9 Å resolution is needed to visualize secondary structure elements, such as α-helices. Unlike ß-, δ- and γ-subunits, which are sensitive to partial degradation (*19*), α- and ε-subunits form tight heterotetrameric complexes ($\alpha_2\varepsilon_2$). The complex structure was solved to 1.9 Å resolution by X-ray crystallography from *A. fulgidus* (this work; 3.3) and to 2.0 Å (*18*) resolution from *M. barkeri*. This heterodimer is likely to maintain a rigid

form within the ACDS complex. Rigid-body fitting in Chimera suggested three possible positions for the *Af*$\alpha_2\varepsilon_2$-subunit, separated by ca. 120° from each other (Fig. 17). Reprocessing the data with an imposed 3-fold symmetry (*C3*) was unsuccessful, indicating that the ACDS complex may be pseudo- or asymmetric.

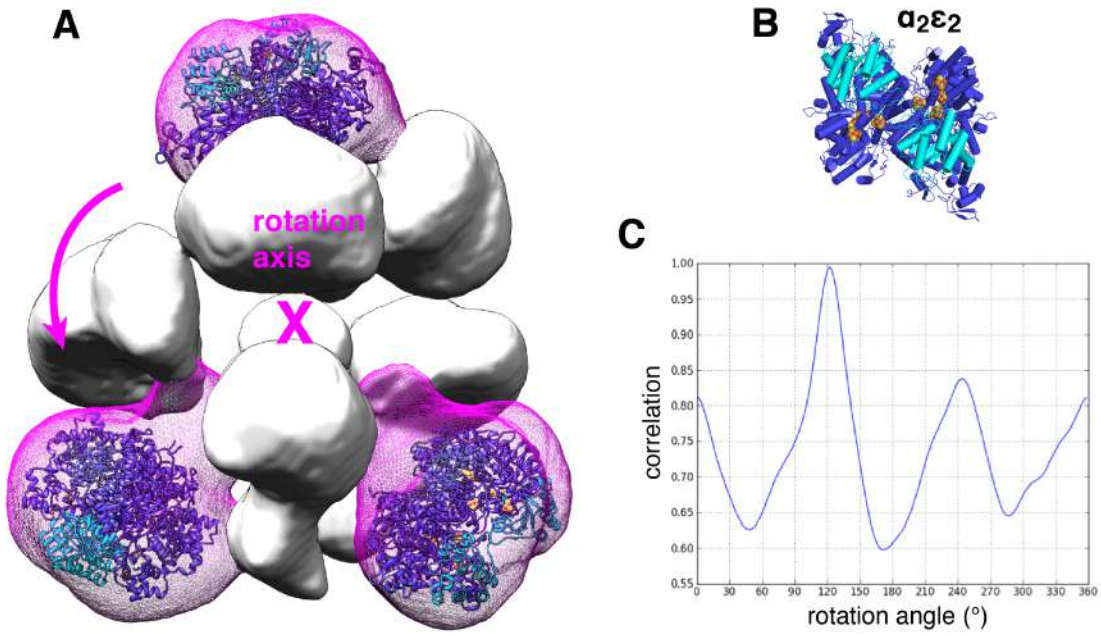

Figure 17. Rigid-body fitting on the *Af*$\alpha_2\varepsilon_2$-subunit. (A) Three possible positions for *Af*$\alpha_2\varepsilon_2$-subunits (pink mesh) were identified by rigid-body fitting in Chimera (*113*). (B) X-ray crystal structure of the *Af*$\alpha_2\varepsilon_2$-subunit at 1.9 Å resolution (3.3). NS 3D reconstruction of the *Af*ACDS complex is shown as surface in white; backbone of α- (blue) and ε- (cyan) subunits are shown as cylinders. Metal clusters are shown as spheres (yellow for S; orange for Fe; green for Ni). (C) Correlation of the NS 3D reconstruction with itself after symmetry transformation along the defined rotation axis calculated in Chimera. The highest correlation is observed at 0°, 120° and 240° of rotation, reflecting the 3-fold symmetry.

3.2.7 INVESTIGATION OF THIN ICE REGIONS

As shown in Figure S4, imaging of the intact protein particles was only possible within thick ice regions, whereas particles of smaller size were identified within thin ice regions. To investigate the nature of these particles, twenty seven movie frames with power spectra oscillating beyond 4 Å were selected and processed as described previously in RELION (*115*) (3.2.4) (Fig. 18A). After several cycles of 2D classification of the manually-selected subset of 500 particles, the resulting 2D class averages were used as templates for the automatic picking. The resulting stack of ca. 6000 particles were split

into fifty class averages by iterative reference-free 2D classification. Most averages were very noisy, whereas twelve 2D classes have a well-defined butterfly shape with 2-fold symmetry and appeared to represent different projection views of the same particle (Fig. 18B). Twelve 2D averages were used as an anchor set to generate the initial 3D reference by angular reconstitution in IMAGIC (Fig. 18C) (*116, 141*). The final 3D reconstruction was obtained after standard unsupervised 3D classification (Fig. 18D) and refinement of the initial reference in RELION. The highest quality 3D reconstruction comprised ca. 2000 (Fig. 18D; red framed) particles and was solved to a resolution of 11 Å (FSC cutoff of 0.143) (Fig. 18E). The butterfly shape strongly resembles the previously-solved crystal structure of the *Mb*$\alpha_2\varepsilon_2$-subunit (*18*), which could be fit into the 3D reconstruction with a high level of confidence (Fig. 18E).

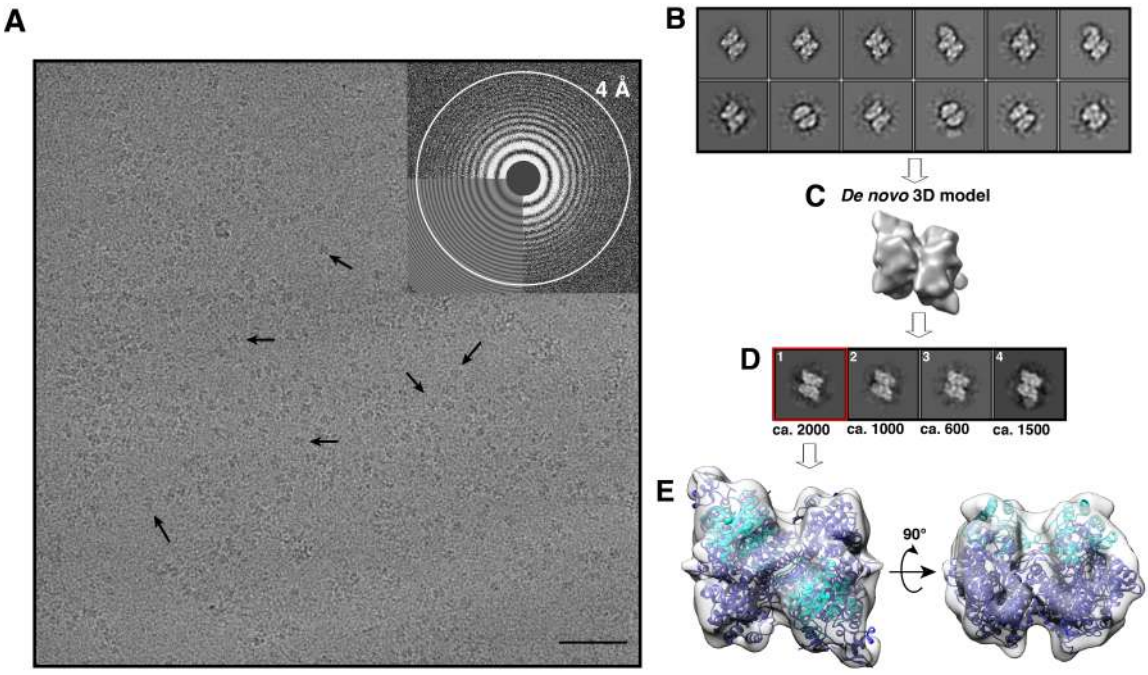

Figure 18. *Ab initio* 3D reconstruction of the *Af*$\alpha_2\varepsilon_2$-subunit. (A) Representative cryo-electron micrograph of the thin ice region imaged at -2.0 µm defocus with corresponding power spectrum (inset). The scale bar is 50 nm. Arrows indicate the particle positions (B) Representative 2D class averages generated in RELION (*115*). (C) Initial 3D reconstruction of $\alpha_2\varepsilon_2$-subunit without imposed symmetry (C1) after angular refinement in IMAGIC (*116*) (D) 3D classification of ca. 6000 particles in RELION (*115*) with initial 3D reconstruction as a reference. The particles of class 1 (red frame) were used in the final refinement (E) Rigid body fitting of the $\alpha_2\varepsilon_2$ crystal structure into the refined 3D map.

3.3 STRUCTURAL INVESTIGATION OF *Af*$\alpha_2\varepsilon_2$-SUBUNIT

3.3.1 PROTEIN PURIFICATION

The *Af*$\alpha_2\varepsilon_2$-subunit was isolated by proteolytic digestion of the purified *Af*ACDS complex with α-chymotrypsin based on the protocol previously described by Grahame *et al.* (*19*). First, $\alpha_2\varepsilon_2$-subunit was separated from the protein digestion mixture by AEC (Source 30Q) and eluted at 350 mM NaCl. Second, the eluted protein was analyzed by SEC using a Sepharose 6B-CL column. One major brown-colored protein peak eluted at 70 mL, corresponding to a molecular weight of ca. 200 kDa (Fig. 19). SDS-PAGE analysis confirmed the successful isolation of the *Af*$\alpha_2\varepsilon_2$-subunit (Fig. 19; inset). On average, the *Af*$\alpha_2\varepsilon_2$-containing fraction was over 85% pure.

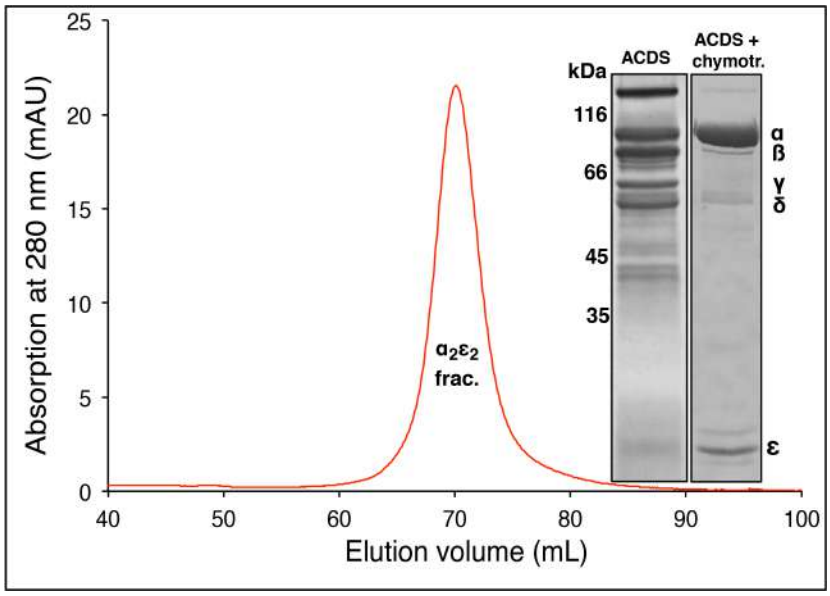

Figure 19. Purification of the *Af*$\alpha_2\varepsilon_2$-subunit. SEC of the α-chymotrypsin-digested *Af*ACDS-containing sample shows only one major symmetric peak eluted at 70 mL. The protein content of the undigested *Af*ACDS complex and isolated *Af*$\alpha_2\varepsilon_2$-subunit ($\alpha_2\varepsilon_2$ frac.) were analyzed by 12% SDS-PAGE (inset).

Unlike Grahame´s results (*19*), where incubation with the protease disintegrated the purified ACDS complex into three stable protein subcomplexes, namely $\alpha_2\varepsilon_2$-, ß- and δγ-subunits, α-chymotrypsin cleaved ß-, δ- and γ-subunits into multiple short peptides even after 20 mins of incubation, and α and ε subunits remained intact after 24 hours of incubation with protease (Fig. 19 inset SDS-PAGE and later confirmed by crystal structure analysis; 3.3).

For comparison in kinetics studies, *Mb*$\alpha_2\varepsilon_2$-subunit was isolated according to the same protocol described for *Af*$\alpha_2\varepsilon_2$-subunit. With the exception of a much higher yield, the

purification results of *Mb*$\alpha_2\varepsilon_2$-subunit (Fig. S8) and *Mb*ACDS complex (Fig. S9) were comparable with the ones described for *Af*$\alpha_2\varepsilon_2$-subunit and *Af*ACDS complex, respectively.

3.3.2 PRODUCTS OF *cdhAB* GENES

Genome of *A. fulgidus* contains two operons encoding two distinct $\alpha_2\varepsilon_2$-subunits, designated *cdhA1B1* (UniProt gene annotation: AF_1100 – 1101) and *cdhA2B2* (UniProt gene annotation: AF_2397 – 2398) (*159*), where *cdhA* and *cdhB* encode α- (CdhA) and ε- (CdhB) subunits, respectively (Fig. 20). The corresponding subunits in each operon share over 95% sequence identity. The 1.92 Å-resolution electron density map is of sufficient resolution to assign amino acid side chains *de novo* (e.g. the imidazole side chain of His198 and hydroxymethyl group of Ser201; three-carbon aliphatic chain with guanidinium group of Arg260 and isobutyl group of Leu263 in CdhA1 and CdhA2, respectively; Arg88 and the methyl group of Ala79 in CdhB1 and CdhB2, respectively) (Fig. S10). Furthermore, short insertions in the CdhA1 and CdhB1, such as Phe391 – Phe392 and Lys8 – Pro13, respectively, are additionally identified. Thus, the *Af*$\alpha_2\varepsilon_2$-subunit structure described in this work is undoubtedly identified as a product of the *cdhA1B1* operon, through sequencing by crystallography.

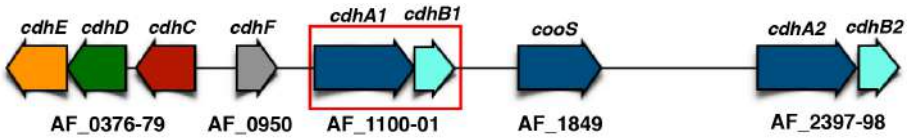

Figure 20. *Af*ACDS operon organization. UniProt annotations are indicated below the genes. The isolated, characterized and crystallized *Af*$\alpha_2\varepsilon_2$-subunit is a product of *cdhA1B1* operon (red frame). Gene descriptions can be found in (1.2.1).

Notably, N-terminal sequencing of the ε subunit of the previously-isolated *Af*ACDS complex matched the product of *cdhB2* gene (*55*), suggesting that *Af*ACDS is encoded in the *cdhA2B2* and *cdhEDC* operons. It is possible that both *cdhA1B1 and cdhA2B2* operons are transcribed when lactate is used as a substrate.

3.3.3 CRYSTALLIZATION AND STRUCTURE SOLUTION

A dark-brown single crystal of *Af*$\alpha_2\varepsilon_2$-subunit formed after two weeks in a condition containing 0.1 M CAPS and 40% (v/v) MPD, in which 8 mg/mL protein solution was reduced with 5 mM DT prior to crystallization. The data set with a maximum resolution of 1.92 Å was collected at 0.9184 Å. The crystal had a monoclinic space group *C*2 with a

unit cell dimensions of a= 99 Å, b = 109 Å and c= 95 Å, beta = 119° (Tab. S1).

The crystal structure of *Af*$\alpha_2\varepsilon_2$-subunit was solved by molecular replacement using the homologous structure of *Mb*$\alpha_2\varepsilon_2$-subunit as a search model (PDB entry: 3CF4) (*18*), with which it shares 47% sequence identity and 98% sequence coverage. Each asymmetric unit contains one α- and one ε-subunits. The oligomer arrangement of $\alpha_2\varepsilon_2$ heterodimer is revealed across the crystallographic two-fold axis between two adjacent αε heterodimers. The α- and ε-subunits are composed of 802 and 184 residues, respectively, of which the N-terminal 30 and 13 residues, respectively, are not resolved in the electron density map. Both N-terminal portions contain several chymotrypsin restriction sites and could be degraded during the enzyme preparation. Data collection and refinement statistics are reported in Table S1.

3.3.4 CRYSTAL STRUCTURE

3.3.4.1 OVERALL STRUCTURE AND SUBUNIT COMPOSITION

The overall envelope of the *Af*$\alpha_2\varepsilon_2$-subunit resembles the shape of a butterfly (Fig. 21A). The fold and subunit arrangement of *Af*$\alpha_2\varepsilon_2$-subunit is almost identical to the previously-reported *Mb*$\alpha_2\varepsilon_2$ structure (r.m.s.d of 1.173 Å by Cα-atoms) (Fig. 21B) (*18*). The structure of the α-subunit can be subdivided into five distinct domains: two central Rossmann fold elements (domains II and IV), two α-helical domains (domains I and III) and one domain (domain V) comprising several α-helices and two ß-hairpins elements (Fig. 21C). Together, domains II and IV contain the four conserved cysteines (Cys271; Cys310; Cys512; Cys541; Cys576) and the histidine residue (His243) for the coordination of the active site (cluster C). Domain I harbors one [4Fe4S] cluster (cluster B), coordinated by conserved cysteine residues (Cys68; Cys71; Cys76; Cys86). Unlike domains I, II and IV, which are also present in other csCODHs, domains III and V are only observed in the cdhCODHs (*15*). Domain III binds two additional cysteine-coordinated [4Fe4S] clusters, termed cluster E (Cys415; Cys444; Cys447; Cys450) and cluster F (Cys405; Cys408; Cys411; Cys454). The role of domain V is presently unknown. The ε-subunit is exclusively found in cdhCODHs and, similar to domains II and IV of the α-subunit, adopts a Rossmann-fold. The central core consists of a five-stranded parallel ß-sheet that is flanked by four- and two-helix bundles. The possible role of the ε-subunit in archaea will be discussed in (3.3.7).

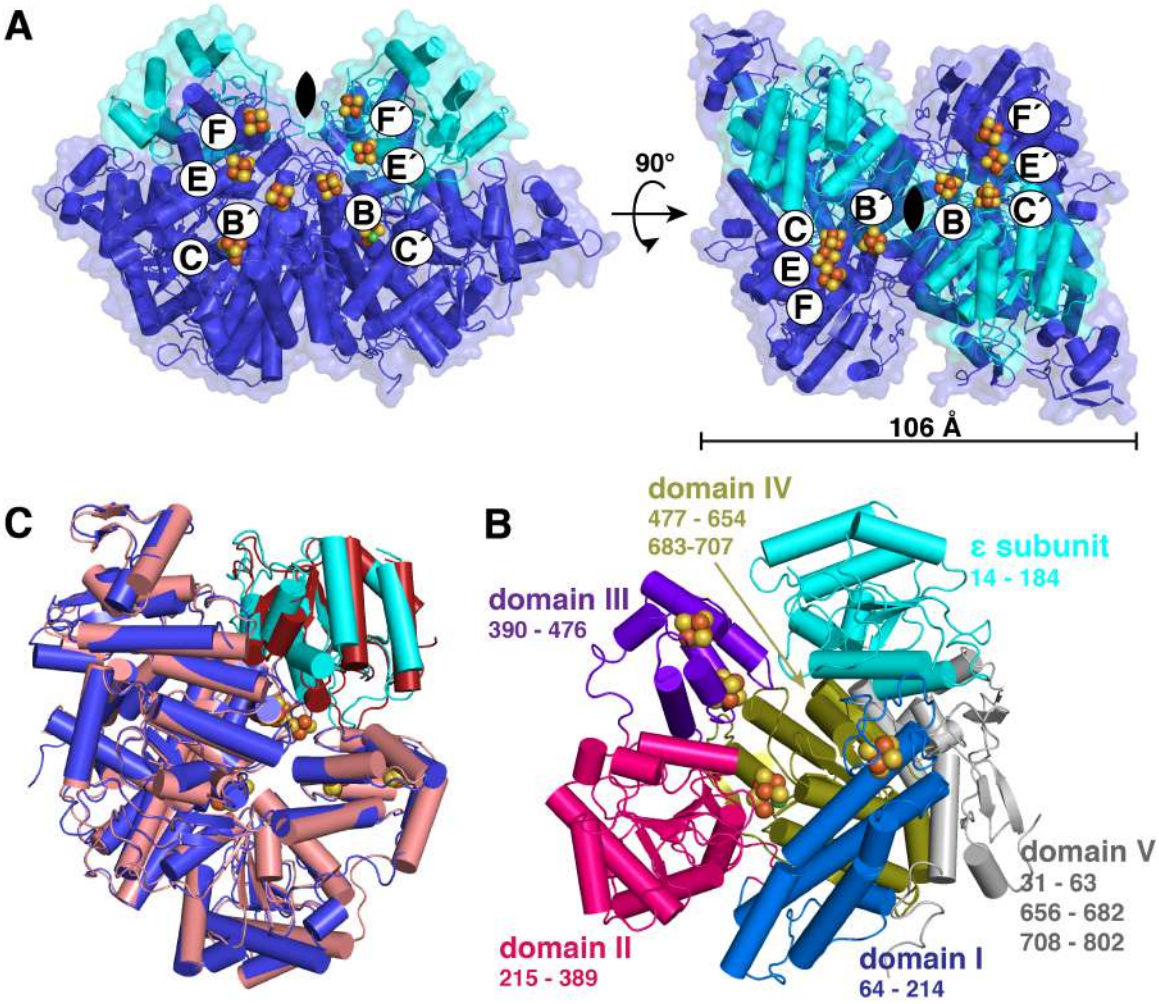

Figure 21. Crystal structure of the *Af*α$_2$ε$_2$-subunit. (A) Side and top views of the *Af*α$_2$ε$_2$-subunit. Protein backbone is shown as ribbon diagram. (B) Structure comparison between *Af*α$_2$ε$_2$- and *Mb*α$_2$ε$_2$-subunits. The α- and ε-subunits of *Af*α$_2$ε$_2$ are colored in navy blue and cyan, respectively. The α- and ε-subunits of *Mb*α$_2$ε$_2$ are colored in salmon and red, respectively. (C) *Af*αε-protomer domains. Numbers indicate the residue position within the protein sequence (Uniprot: AF_1100; AF_1101). Metal clusters are represented as spheres (orange for Fe, yellow for S, green for Ni).

3.3.4.2 HYDROPHOBIC CHANNEL

As shown in surface representation in Figure 22A, the *Af*α$_2$ε$_2$ structure revealed one 25-Å long hydrophobic tunnel, connecting the active site with the protein surface. The channel is formed at the two-fold symmetry axis, producing a hydrophobic bridge between two clusters C within the α$_2$-subunit dimer. Similar channels were also observed in the homologous structure of *Mb*α$_2$ε$_2$ (*18*) and in the monofunctional class IV csCODHs (*41*), but is obstructed in the bifunctional csCODHs of class III (Fig. S11) (*157*). In *Mb*α$_2$ε$_2$ this hydrophobic channel is extended, branching off of the active site and passing through domain IV and the ε-subunit (*18*). The entrance to the putative gas channel in *Af*α$_2$ε$_2$ is

blocked by a short α-helix (Aps488 – Phe500) (Fig. 22B), which is also observed in class IV *Ch*CODH-II (Pro424 – Asn434) (*39*) and *Rr*CODH (Pro429 – Gly440) (*23*). In bacterial CODHs, the channel is open due to a helix shift of 5 Å (Fig. 22C). The structural rearrangement required for channel opening could be achieved in *Af*$\alpha_2\varepsilon_2$, for example by binding of neighboring subunit in the fully-assembled ACDS complex.

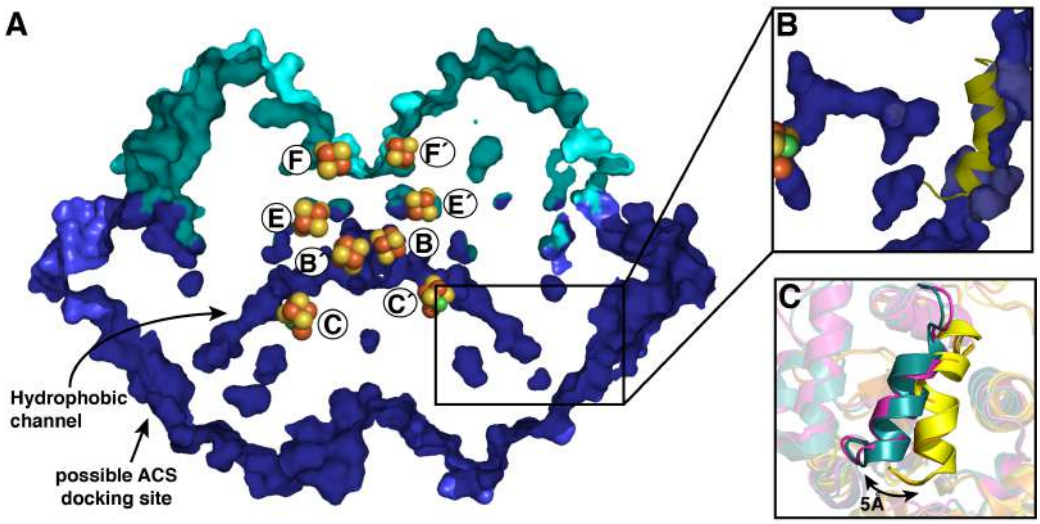

Figure 22. Hydrophobic channel in *Af*$\alpha_2\varepsilon_2$-subunit. (A) A slice through surface of *Af*$\alpha_2\varepsilon_2$ reveals one narrow 25-Å long hydrophobic channel, which enables the access to the active sites. Structures of the α-subunit (blue) and ε-subunit (cyan) are represented as surfaces. Metal clusters are represented as spheres (orange for Fe, yellow for S, green for Ni). (B) and (C) A short α-helix (Aps488 – Phe500; yellow ribbon) blocks the entrance to the hydrophobic channel, which is also observed in *Ch*CODH-II (green ribbon), *Rr*CODH (pink ribbon) and *Mb*$\alpha_2\varepsilon_2$ (orange ribbon).

In a protein complex, the channels are thought to enable the transport of reactive intermediates between multiple active sites (*160*). The most prominent example of channel formation is found in class III *Mt*CODH, where a 67-Å long hydrophobic tunnel facilitates shuttling of CO between the active sites of ACS and CODH (Fig. S11B) (*157*). *In vivo*, *Af*$\alpha_2\varepsilon_2$ exists as a part of a multienzyme complex (*55*). The appearance of the channel in this complex is unconfirmed, as there is no structure of the full complex. A comparison of the acetyl-CoA carbonyl CO/CO_2 exchange rates indicates a tight coupling between the acetyl C-C bond breakage at the cluster A of ACS and the CO oxidation activity at the cluster C of CODH (*161*). The tight coupling requires either the close proximity of the two active sites within the ACDS complex, or the presence of the inter-subunit tunnel enabling substrate transfer between the clusters A and C. From structural data, the active site is buried deep inside the protein scaffold of the *Af*$\alpha_2\varepsilon_2$-subunit,

indicating the necessity for the channel. Thus, the site of the channel opening on the *Af*$\alpha_2\varepsilon_2$-subunit might suggest a place for a possible ACS (ß-subunit) docking site.

3.3.4.3 ELECTRON TRANSFER CHAIN

The *Af*αε heterodimer contains four metal clusters, termed clusters C, B, E and F) (Fig. 22A). Each cluster is located within electron transfer distance to its nearest neighbor, providing a path for the electrons generated during reversible CO oxidation at the cluster C to the terminal electron acceptor (Fig. 23A).

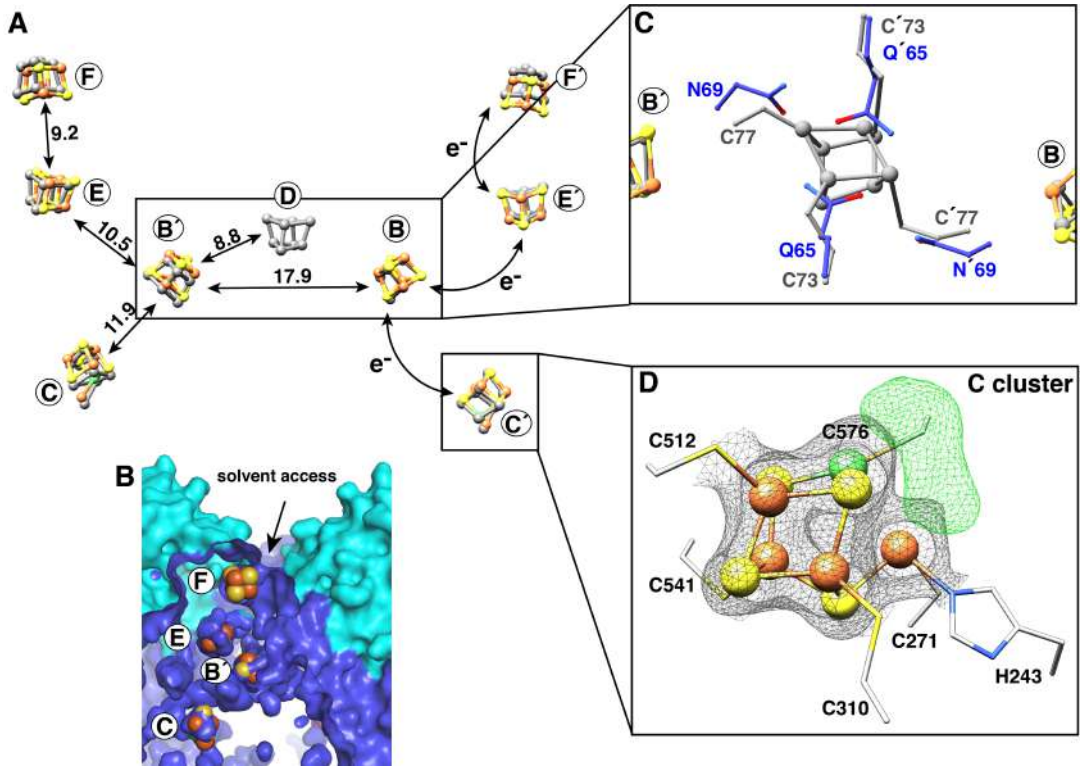

Figure 23. Electron transfer pathway in the *Af*$\alpha_2\varepsilon_2$ structure. (A) Eight metal clusters are arranged in a set of two parallel chains. The chains are composed of three [4Fe4S] clusters (cluters B/B´, E/E´ and F/F´) and one heterometallic [Ni4Fe4S] center (cluster C). (B) Cluster F is solvent accessible, whereas the remaining clusters are buried within the protein scaffold. α- (navy blue) and ε- (cyan) subunits are represented as surfaces. (C) Comparison of the bridging interface. The bridging [4Fe4S] cluster from the *Mb*$\alpha_2\varepsilon_2$-subunit is shown in gray ball-and-stick model. (D) The structure and the first coordination sphere of the cluster C. Unmodeled positive electron density (F_o-F_c) is shown in green mesh with contour level of 4.0 σ between Ni and *exo*-Fe. 2 F_o-F_c map is depicted in gray mesh with contour level of 1.3 σ). Metals clusters are shown as spheres (Fe in orange, S in yellow, Ni in green for *Af*$\alpha_2\varepsilon_2$ and all in gray for *Mb*$\alpha_2\varepsilon_2$). Amino acids are shown as sticks. The distances are shown in Angstrom.

Clusters B, E and F are all-cysteine coordinated cuboidal [4Fe4S] clusters. The active site is a pseudocubane [Ni3Fe4S] cluster bridged to an exogenous Fe atom (*exo*-Fe) and coordinated by highly-conserved five cysteines (Cys512, Cys576, Cys541, Cys310,

Cys271) and one histidine (His243), which shows an equivalent active site geometry as observed in other structurally-characterized csCODHs (*160*) and cdhCODHs (*18*). Cluster F is solvent-accessible and is potentially the terminal member of the electron transfer (ET) pathway between cluster C and the final electron acceptor (Fig. 23B).

Unlike to *Mb*$\alpha_2\varepsilon_2$, the structure of the *Af*$\alpha_2\varepsilon_2$-subunit revealed no covalently bridging [4Fe4S] cluster (cluster D) positioned along the twofold axis between two α-subunits (Fig. 23C). The loss of the bridging cluster is caused by the double exchange of the conserved coordinating cysteines (Cys77 and Cys73 in *Mb*$\alpha_2\varepsilon_2$) to asparagine (Asn69) and glutamine (Gln65) in *Af*$\alpha_2\varepsilon_2$, respectively. It is not clear whether the removal of the bridging cluster will interrupt the electron flow between the two parallel ET chains, since electron transfer can also be facilitated between two neighboring clusters B, located approx. 18 Å apart from each other (*162, 163*). Notably, the structurally characterized csCODHs are homodimers covalently linked by either [4Fe4S] (*20, 23, 39*) or [2Fe2S] (*35*) clusters. However, our data suggests, that the bridging cluster is most probably not required for the dimerization.

A peak in the F_o-F_c omit electron density map has been observed between Ni and the *exo*-Fe atoms after full refinement of the [Ni4Fe4S] cluster (Fig. 23D). The distribution of the positive electron density suggests that a tri-atomic molecule may satisfy the observed electron density between the Ni and Fe atoms. The mechanistic details of reversible CO oxidation have been derived from crystal structures of substrate/product- and inhibitor-bound to cluster C (*39-43*). Refinement with neither a CO_2-bound state nor a Ni-bound formyl- and *exo*-Fe-bound hydroxyl ligand fully explained the electron density. The CO_2 moiety was refined with ca. 72% occupancy for both O1 and O2 atoms, whereas the C atom has only 18% occupancy (Fig. S12A). Low carbon occupancy could indicate catalytic degradation of CO_2 to formyl and hydroxyl compounds. When Ni-bound formyl and Fe-bound hydroxyl were fitted into the F_o-F_c omit electron density map, the former was refined to approx. 50% occupancy, whereas the latter was occupied to 86% (Fig. S12B). Formyl binding geometry (Ni-C-O angle of 151°) differs from the one observed for cyanide inhibition studies (Ni-C-O angle of 165° for *Ch*CODH-II (*42*)), which are used as analogs for CO binding (Fig. S13). A bent Ni-formyl geometry could occur during the initial binding stage and lower the energetic activation barrier for CO oxidation (*42*). However this stage is short-lived and would be impossible to trap in the crystal (*42*). Moreover positive F_o-F_c electron density remained between Ni and O1 atom or between O1 atoms of formyl and O2 atom of hydroxyl, when CO_2 or CO were used as ligands

(Fig. S12). The inconsistency between the experimental observations and the imperfect fit of the respective models are indicative of a mixture of species. This heterogeneity is consistent with CODH structures from *M. barkeri (18)* and *M. thermoacetica (164)*, where various binding geometries for diatomic ligands presumably bound to Ni atom were observed (Fig. S13). Unfortunately, clear distinguishing of different intermediates of substrate binding is a challenging task at a resolution of 1.92 Å. The observed positive F_o-F_c electron density mostly describes two substrate-bound states: ca. 20% of CO_2-bound and ca. 60% of Ni-bound formyl with a hydroxyl group bound to the *exo*-Fe (Fig. S12).

3.3.5 SEQUENCE SIMILARITY NETWORK OF THE CdhA PROTEIN FAMILY

To my knowledge, the *Af*$\alpha_2\varepsilon_2$-subunit is the first Ni-containing CODH missing the bridging iron-sulfur cluster. In order to investigate this unusual feature, 271 CdhA sequences (InterPro ID: IPR004460) were analyzed for the presence of the [2Fe2S] or [4Fe4S] binding motifs for the bridging cluster with Clustal Omega (*165*). Interestingly, CdhA sequences from 31 organisms were identified as missing the conserved Cys required for a bridging cluster coordination, but still contained all Cys residues required for the proper assembly of the remaining metal clusters (hereafter referred to as $CdhA_{\Delta D}$) (Fig. S14). The organisms bearing c*dhA*$_{\Delta D}$ genes are spread across the phyla Euryarchaeata, Thaumarchaeota and Lokiarchaeota. The exchange pattern is poorly conserved among the cluster D depleted CODHs, revealing that the most frequent Cys exchange are to Asp, Thr, Ala, Pro or Ile (Fig. S14).

In order to predict whether the Cys exchange leading to the cluster D elimination, occur in discrete group of closely related proteins (based on the sequence similarity), a sequence similarity network (SSN) for the CdhA protein family (InterPro ID: IPR004460) was generated using the Enzyme Function Initiative-Enzyme Similarity Tool (Fig. 24) (*166*). The SSN showed that CdhA sequences are binned into four groups, denoted as group I, II, III and IV. Each group contains at least one organism with the depleted bridging cluster.

Group I is almost exclusively composed of Methanosarcinaceae family members, whereas seven organisms with $CdhA_{\Delta D}$ belong to members of the nitrate-dependent methanotrophic archaeon *C. Methanoperedens nitroreducens* and several poorly-characterized organisms of Euryarchaeota. Group II includes species found predominantly in the Methanosaetaceae and Archaeoglobacae families, as well as some

uncultured archaeons. Interestingly, this group contains more than 60% of the $CdhA_{\Delta D}$ sequences. Group III is composed of a diverse group of hydrogenotropic organisms from Methanobacteriales, Methanomicrobiales and Methanococcales, some distantly related species of Crenarchaeota, Thaumarchaeota and bacteria. Six miscellaneous organisms of the bacterial domain were identified with the *cdhA* gene: *Firmicutes bacterium* ADurb.Bin419, *C. Desulforudis audaxviator* strain MP104C, *Deltaproteobacteria bacterium RBG_13_52_11*, *Deltaproteobacteria bacterium RBG_16_49_23*, *Chloroflexi bacterium RBG_13_51_36* and *Chloroflexi bacterium RBG_13_50_10*. One organism of the phylum Thaumarchaeota (*Thaumarchaeota archaeon RBG_16_49_8*) contains the C*dhA*$_{\Delta D}$. Most organisms within group IV are members of uncultured archaeons. Sequence analysis of the two organisms from distantly-related Euryarchaeota (*C. Altiarchaeales archaeon WOR_SM1_86-2*) and Lokiarchaeota (*Lokiarchaeota archaeon strain CR_4*) of group IV were identified to be depleted of cluster D.

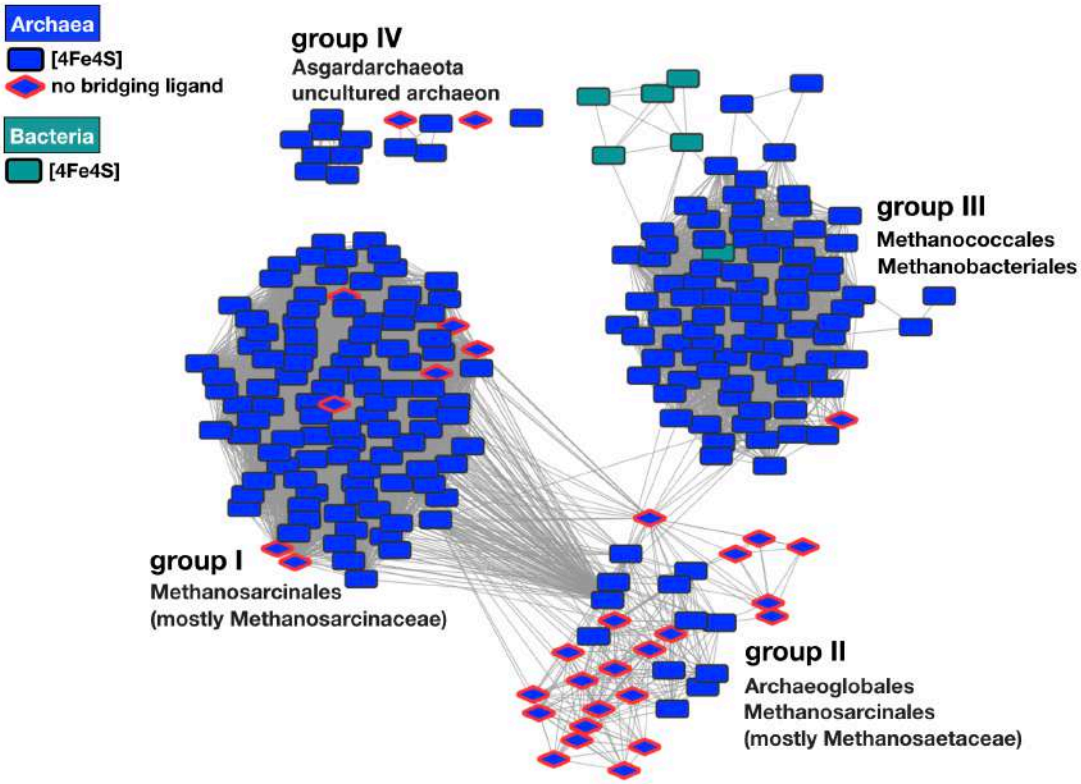

Figure 24. Sequence similarity network of the cdhCODH family enzymes. The $CdhA_{\Delta D}$ sequences are depicted as red-framed rhombs. The CdhA-sequences containing the binding motif for the [4Fe4S] cluster in bacteria and archaea are shown as green or blue rectangles, respectively. 244 nodes represent 271 CdhA sequences (IPR004460) with 8399 pairwise connections (edges in gray line). The SSN was generated using EFI-EST and visualized in Cytoscape (*167*). The alignment score was set to 255. E value was 10^{-5}.

Additionally, the SSN and the sequence comparison between the csCODHs were performed using 1943 protein sequences (InterPro ID: IPR010047) (Fig. S15). In one anaerobic bacterium, *Pseudobacteroides cellulosolvens* ATCC 35603, and thirteen archaea organisms (mostly miscellaneous hydrogenotropic methanogens), the bridging cluster D is depleted (Fig. S16).

3.3.6 PHYLOGENEIC ANALYSIS OF THE CLUSTER D DEPLETED CODHs

Since the analysis of protein sequence similarity does not provide information about the ancestry of cluster D depletion, phylogenetic analysis is a better tool to understand the relationship between the organisms sharing the similar trait. To address this point, thirteen organisms containing c*dhA*$_{\Delta D}$ genes were mapped on a maximum likelihood (ML) phylogenetic tree, generated by Adam *et al.* (*33*)[2]. As shown in Figure 25, the evolutionary lineage could yield the c*dhA*$_{\Delta D}$ gene acquisition in Archaeoglobales (including *cdh*A1 gene in *A. fulgidus* (3.3.2)). The conserved substitution pattern of Pro-XX-Ala and Ser/Gln-XXX-Asn at the site of potential [2Fe2S] or [4Fe4S] bridging clusters supports this assumption (Fig. S14). Interestingly, the *cdhA2* gene of *A. fulgidus* (3.3.2) is more related to the *cdhA* genes of Methanosarcinales order, whereas *cdhA1* gene is aligned with the order Archaeoglobales. The inheritance of the remaining c*dhA*$_{\Delta D}$ genes among distinct phyla (group I, III, IV; Fig. 25) could be explained by either horizontal gene transfer between different lineages or resultant from independent exchange of the coordinating Cys leading to the loss of the bridging ligand.

As observed for Archaeoglobales, the high occurrence of the cluster D depleted *cooS* genes (hereafter referred to as *cooS*$_{\Delta D}$) in the Methanococci class could be explained by vertical gene transfer (Fig. S17), which is supported by the high similarity of the coordinating Cys substitution pattern Cys-XX-Gly and Gly-XXX-Ile/Asn (Fig. S16).

[2] ML phylogenetic tree was obtained with courtesy of Prof. Simonetta Gribaldo (Institut Pasteur, Paris)

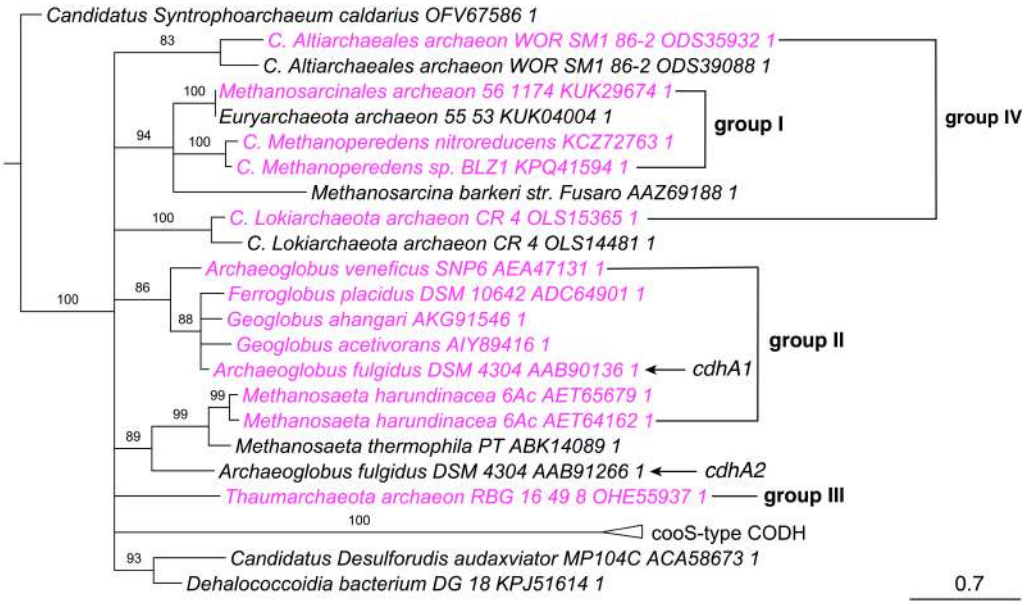

Figure 25. Phylogenetic mapping of cluster D depleted CdhA sequences. Fourteen $cdhA_{\Delta D}$ genes were mapped on the rooted ML phylogenetic tree of CdhA/CooS homologs (*33*) and colored in pink. The *cdhA* genes containing conserved cysteines for [2Fe2S] or [4Fe4S] binding motifs are colored in black. Numbers at nodes indicate the bootstrap values (100 replicates). Branches with support below 80 were collapsed. The scale bar represents the average number of substitutions per site. The figure was prepared in TreeGrap2 (*168*). The tree was rooted with *Candidatus Syntrophoarchaeum caldarius* OFV67586 as an out-group (*169*).

3.3.7 POTENTIAL ROLE OF THE ε-SUBUNIT

Except for Altiarchaeales (*170*), the ε-subunit is ubiquitous and found within all operons encoding for cdhCODHs. The ε-subunit is positioned in close proximity to the solvent-accessible metal clusters (D and F in *Mb*$\alpha_2\varepsilon_2$- and F in *Af*$\alpha_2\varepsilon_2$-subunits) and thus could provide the binding site for the physiological electron donor/acceptor. As previously reported, *Mb*$\alpha_2\varepsilon_2$ is able to reduce FAD, FMN, ferredoxin and MV with CO, but not NAD^+, $NADP^+$ or coenzyme F_{420} (*53*). The ε-subunit is affiliated with the deoxyhypusine synthases (DHS)-like NAD/FAD-binding domain superfamily (*18*), which includes structurally-related thiamine pyrophosphate (TPP)-dependent enzymes (*38, 171*), DHS (*172*) and sirtuins (*173*).

The similarity to the FAD-binding domain prompted an investigation into FAD binding activity with ε-subunit. Neither soaking with crystals nor co-crystallization of the isolated $\alpha_2\varepsilon_2$-subunit with FAD or FMN lead to the resolving of a cofactor binding site. Instead, kinetics studies of flavin binding were performed. Kinetics experiments for *Af*ACDS and *Af*$\alpha_2\varepsilon_2$-subunit were limited by very low yields of protein production, so the FAD and FMN binding kinetics were measured for both *Mb*$\alpha_2\varepsilon_2$-subunit and *Mb*ACDS complexes.

*Af*α$_2$ε$_2$ was only analyzed for FAD binding kinetics. The ε-subunit lacking *Ch*CODH-II was used as a control. To this end, CO-dependent flavin reduction was monitored at 304 nm at different substrate concentrations. In the case of *Mb*α$_2$ε$_2$, both FAD and FMN reduction activity exhibit Michaelis-Menten (MM) type kinetics (Fig. 26A and B). The lower catalytic turnover rates (10.5 s^{-1} for FMN vs. 30.9 s^{-1} for FAD), together with the higher K_M value for FMN reduction (135.9 ± 7.2 µM for FMN vs. 57.7 ± 5.8 µM for FAD) indicate that FAD is a "better" electron acceptor for the *Mb*α$_2$ε$_2$-subunit (Tab. 9). The *Af*α$_2$ε$_2$ showed similar FAD binding kinetics of MM type with the comparable K_M value of 76.2 ± 5.0 µM (Fig. 26B; Tab. 9). Although FAD was identified as one of the electron acceptors in *Ch*CODH-II (*46*), the kinetic data of CO oxidation could not be fit to the MM equation within the employed flavin concentration range, and instead was fit with a linear regression (Fig. 26A).

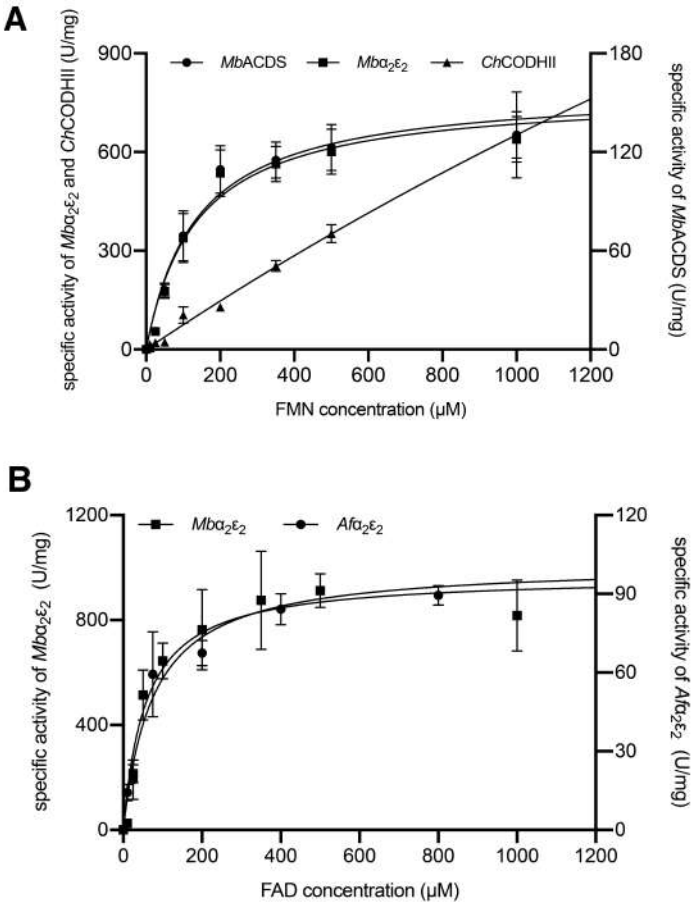

Figure 26. CO-dependent flavin reduction in class II and IV Ni-CODHs. CO-dependent reduction activity with FMN (A) and FAD (B) as an electron acceptor. Activity was measured for *Mb*ACDS, *Mb*α$_2$ε$_2$, *Af*α$_2$ε$_2$ and *Ch*CODH-II at 37°C with a concentration range of 0 to 1 mM for flavins. Except for *Ch*CODH-II, the data were fit to the MM equation using GraphPad Prism (version 8.0.2 for macOS, GraphPad Software, La Jolla California USA, www.graphpad.com). The relevant kinetic constants are reported in Table 9.

These findings indicate that FAD and *Ch*CODH-II do not form a tight protein-substrate complex, unlike FAD and *Mb*$\alpha_2\varepsilon_2$ or *Af*$\alpha_2\varepsilon_2$-subunits. Presumably in csCODHs, the CO-dependent FAD reduction is facilitated by the thermodynamically favorable electron transfer from the difference in redox potential between the electron acceptor (FAD) and donor (reduced [4Fe4S] cluster), as well as their distance, instead of promoting catalysis by stable binding. Consistent with this assumption, the activity of the CO-dependent reduction of MV (1400 U/mg for *Ch*CODH-I and 1000 U/mg for *Ch*CODH-II) and benzyl viologen (BV) (5200 U/mg for *Ch*CODH-I and 3100 U/mg for *Ch*CODH-II) differed significantly from the CO-dependent FAD (104 U/mg for *Ch*CODH-I and 31 U/mg for *Ch*CODH-II) and FMN (104 U/mg for *Ch*CODH-I and 31 U/mg for *Ch*CODH-II) reduction activities (*46*). The isolated *Mb*$\alpha_2\varepsilon_2$-subunit, however, showed similar range of MV (52 ± 3 U/mg) and FMN (200 ± 60 U/mg) CO-dependent reduction activity (this study). Apart from some structural alternations in the protein core (Fig. 3; 1.2.4) (*160*), the major difference between cdh- and csCODHs is the absence of the ε-subunit in the latter. Collectively, these observations contribute to the assumption that ε-subunit indeed provides a scaffold for flavin binding.

Table 9. The Michaelis-Menten kinetic parameters of flavin binding for *Af*$\alpha_2\varepsilon_2$-subunit, *Mb*$\alpha_2\varepsilon_2$-subunit and *Mb*ACDS complex.

	Af$\alpha_2\varepsilon_2$			
	K_M (μM)	V_{max} (U/mg)	k_{cat} (s^{-1})	k_{eff} ($s^{-1}\mu M^{-1}$)
FAD	76.2 ± 5.0	101.5	186.1	2.4
	Mb$\alpha_2\varepsilon_2$			
FAD	57.7 ± 5.8	968.8	1776.1	30.9
FMN	135.9 ± 7.2	778.3	1426.9	10.5
	*Mb*ACDS			
FAD	60.7 ± 7.1	207.2	897.9	14.8
FMN	136.0 ± 7.2	158.9	688.6	5.1

Both FAD and FMN exhibit similar affinity for *Mb*ACDS complex (K_M = 60.7 ± 7.1 μM for FAD (Fig. S18; Tab. 9) and K_M = 136.0 ± 7.2 μM for FMN (Fig. 26A; Tab. 9)) when

compared to the isolated *Mb*$\alpha_2\varepsilon_2$-subunit (K_M = 57.7 ± 5.8 µM for FAD and K_M = 135.9 ± 7.2 µM for FMN). These data could be explained by a peripheral position of the ε-subunit within the fully assembled multimeric protein complex, since the flavin binding was not affected by the steric hindrance of the other ACDS-subunits.

A cavity, observed between the α- and ε-subunits in the crystal structure of *Mb*$\alpha_2\varepsilon_2$ (Fig. 27A), was suggested to facilitate the FAD binding based on the structural homology between the TPP middle domain and the ε-subunit (Fig. 27B) (*18*). Consistent with this hypothesis, the site of the potential FAD binding is in a close proximity (ca. 9 Å) to the clusters F and E (Fig. 27A) and therefore can be a member of the ET chain. The positively charged amino acids lining the predicted binding pocket may contribute to the binding of the negatively charged pyrophosphate group of FAD in *Mb*$\alpha_2\varepsilon_2$ (Fig. 27C). Surprisingly, this cavity is disrupted in the *Af*$\alpha_2\varepsilon_2$-subunit due to some conformational changes of the residues lining the binding pocket (e.g. Phe11 and Leu154 (*Mb*$\alpha_2\varepsilon_2$) → Asp19 and Thr167 (*Af*$\alpha_2\varepsilon_2$) in the ε-subunit, respectively) and several exchange to bulkier amino acids (e.g. Gly142 (*Mb*$\alpha_2\varepsilon_2$) → Phe154 (*Af*$\alpha_2\varepsilon_2$) in the ε-subunit) (Fig. 27D and E). Due to the nonpolar nature of amino acids (Fig. 27F), contributing to the suggested FAD-binding site, in *Af*$\alpha_2\varepsilon_2$ this cavity is likely to remain closed *in vivo* and wont be able to harbor a charged ligand. Thus, the cdhCODHs might accommodate an alternative flavin binding site to the one proposed by Gong *et al.* (*18*).

The catalytic efficiencies for CO-dependent FAD reduction in the *Af*$\alpha_2\varepsilon_2$- and *Mb*$\alpha_2\varepsilon_2$-subunits are similar in the initial step of substrate binding, as supported by comparable K_M values (76.2 ± 5.0 µM for *Af*$\alpha_2\varepsilon_2$ and 57.7 ± 5.8 µM for *Mb*$\alpha_2\varepsilon_2$) (Fig. 26B; Tab. 9). The following product formation step was appr. 13 times slower for *Af*$\alpha_2\varepsilon_2$, as observed from the k_{cat} values (2.3 $s^{-1}\mu M^{-1}$ for *Af*$\alpha_2\varepsilon_2$ and 30.9 $s^{-1}\mu M^{-1}$ for *Mb*$\alpha_2\varepsilon_2$) (Tab.9). There are several explanations for the observed discrepancy. Simplified, the rate of the electron transfer (k_{ET}) drops exponentially with increasing donor-acceptor-distance and is dependent on the thermodynamic driving force (ΔG^0) and the characteristics of the electron propagating medium (e.g. protein matrix, donor-acceptor orientations, ligands rearrangements upon electron transfer) (*163*). As shown for biological, synthetic or semisynthetic reaction centers, modulating the donor-acceptor distance by only 0.5 Å (in e.g. cytochrome *c*) changed the k_{ET} by 3 orders of magnitude. However, very similar k_{ET} values were observed for systems (e.g. porphyrin/quinone) in which donor-accepter distances were altered by approx. 3.5 Å (*163*). Thus, subtle differences in the protein matrix, together with displacements in the [4Fe4S] cluster position could contribute to the

lower k_{cat} value observed in the *Af*$\alpha_2\varepsilon_2$-subunit.

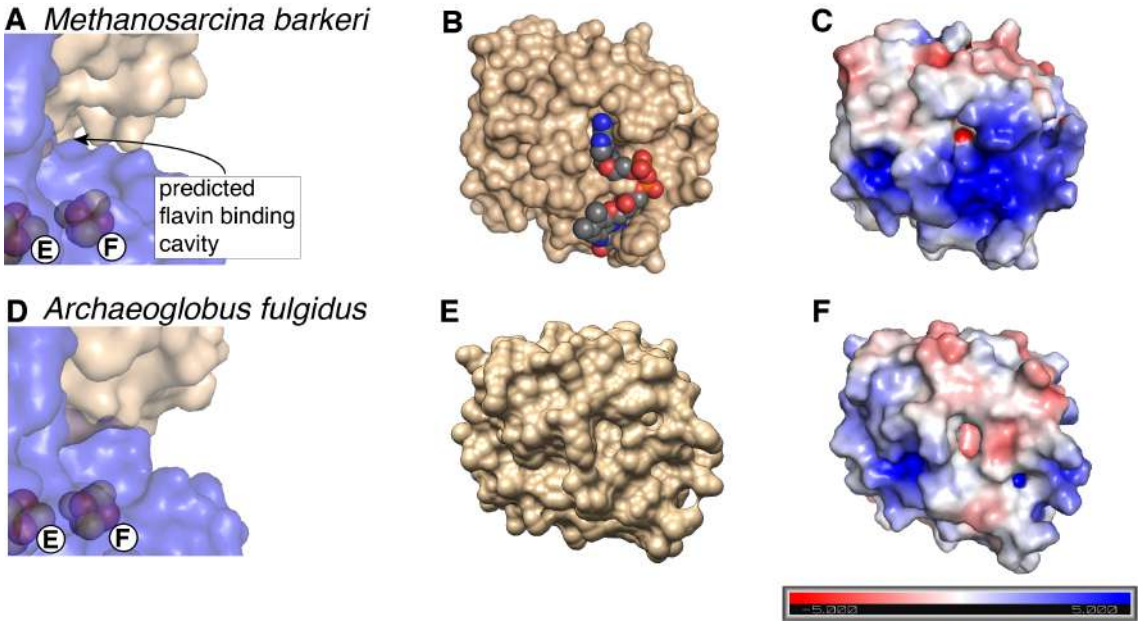

Figure 27. Predicted FAD binding cavity in *Mb*$\alpha_2\varepsilon_2$- and *Af*$\alpha_2\varepsilon_2$-subunits. (A) The proposed FAD binding site in *Mb*$\alpha_2\varepsilon_2$ is located at the interface between the α- and ε-subunits (*18*). (B) Proposed model of FAD bound to ε-subunit (figure obtained from (*18*)). (D) The proposed FAD-binding site is blocked in the *Af*$\alpha_2\varepsilon_2$-subunit. (E) The surface representation of the ε-subunit of the *Af*$\alpha_2\varepsilon_2$. α- (navy blue) and ε- (wheat) subunits are represented as surfaces. Metals clusters are shown as spheres (Fe in orange, S in yellow). Electrostatic potential surfaces of the predicted FAD binding pockets in *M. barkeri* (C) and *A. fulgidus* (F) were calculated in PyMol (red and blue denotes negative and positive charges, respectively)

Since the cluster D depletion did not abort the CO-dependent FAD reduction in *Af*$\alpha_2\varepsilon_2$, its role in electron transfer pathway is questionable also in CODHs with bridging cluster. This hypothesis is consistent with the electronic absorption, magnetic circular dichroism, and RR experiments, indicating that the cluster D remained in a diamagnetic oxidized $[4Fe4S]^{2+}$ state at ≥ -530 mV (*174*), which is below the catalytically relevant potentials of CO/CO_2 interconversion. Thus the C↔B′↔E↔F ET chain in cdhCODHs and C↔B′ ET chain in csCODHs could promote the ET between the terminal electron acceptor (e.g. FAD or ferredoxin (*53*)) and the active site. This assumption is supported by a similar configuration of ferredoxin binding observed in pyruvate ferredoxin oxidoreductase *(18)*, which has high sequence similarity with domain III of the α-subunit. Analogous binding would position the ferredoxin within close proximity to the E and F clusters. Additionally, the 1:1 stoichiometry observed for the *Mt*CODH-ferredoxin complex (*175*) is similar to the dimeric arrangement of both cdh- and csCODHs, supporting the functionality of two C↔B′↔E↔F chains in cdhCODH and C↔B′ in csCODH.

3.4 F_{420}-REDUCING HYDROGENASE FROM *M. BARKERI* MS

3.4.1 PROTEIN PURIFICATION

The F_{420}-reducing hydrogenase from *M. barkeri* (*Mb*FRH) was isolated by anaerobic fractionation of soluble crude cell extract from MeOH-grown cells of *M. barkeri* MS on a preparative Sepharose 6B-CL column. Hydrogenase-containing fractions were identified by measuring H_2-dependent MV reducing activity, which revealed that the active enzyme is distributed in two distinct peaks (Fig. 28).

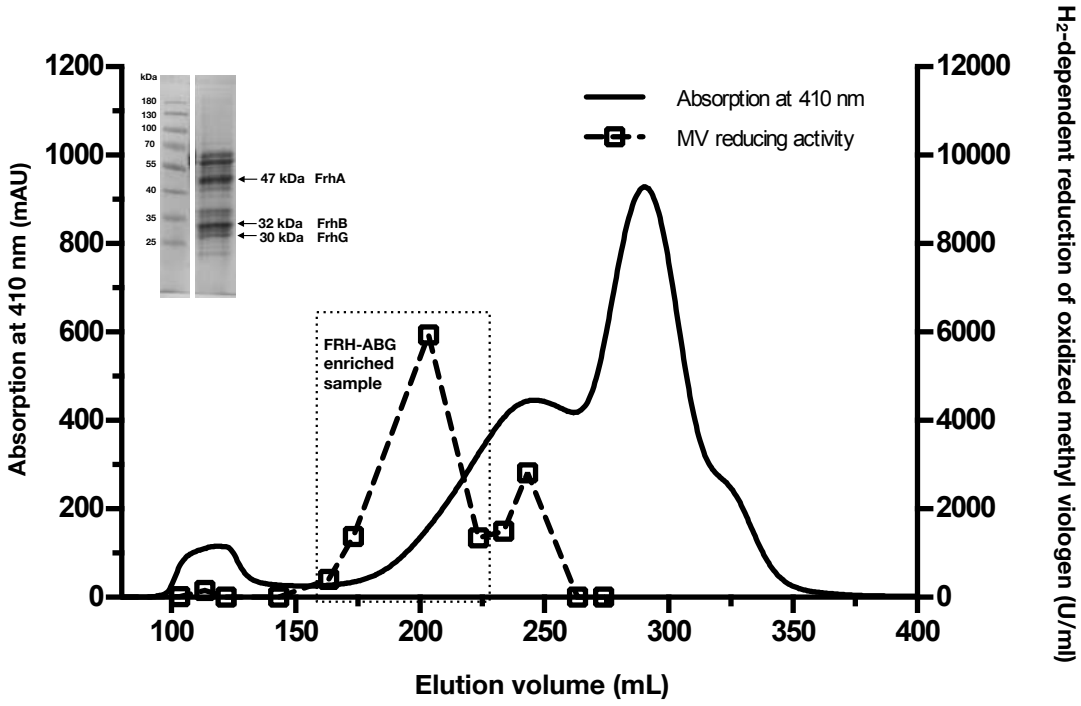

Figure 28. Purification of the *Mb*FRH. The *Mb*FRH sample was enriched by fractionating the soluble crude cell extract on a Sepharose 6B-CL column. Absorption at 410 nm (solid line) and H_2-dependent MV-reduction activity (dashed line) were monitored. 12% SDS-PAGE demonstrates the purity of the FRH-enriched sample (left inset). Arrows indicate the protein bands that presumably correspond to the FRH-A, FRH-B and FRH-G subunits based on their molecular weight.

The catalytically active protein fraction of high molecular weight, eluted between 150 and 220 mL (box with dotted line: Fig. 28), was collected (denoted as the FRH-enriched sample) and used for crystallization experiments. The presence of the other hydrogenases in the soluble crude cell extract could explain the catalytic activity in the protein peak of lower molecular weight, since *M. barkeri* expresses three types of hydrogenases (*176*). The second catalytically active fraction (225 – 260 mL) was not characterized in this study. Homogeneity of the FRH-enriched sample was estimated to be ca. 40% pure, as

determined by comparing the intensity of the hydrogenase subunit bands (47 kDa, 32 kDa, and 30 kDa) to the overall band intensities of all other proteins in the sample from SDS-PAGE (Fig. 28; left inset).

Typically, increasing the duration of the purification has a negative effect on the stability and quality of the protein. Previously isolated FRH from *M. barkeri* and other organisms contained in at least two populations with different molecular weights, in which the catalytic activities and cofactor occupancies varied significantly between these protein forms (*68, 177-180*). This indicates the instability of isolated FRH, which has been purified based on multistep chromatographic purification protocols (*68, 177-181*). Due to high protein symmetry and its ability to crystallize easily from the heterogeneous FRH-enriched sample, the protein purification protocol could be significantly shortened, even if the purity of the sample is compromised.

3.4.2 CRYSTALLIZATION AND *Mb*FRH CRYSTAL STRUCTURE

*Mb*FRH crystallizes out of a sample with approximately 40% protein purity (inset Fig. 28). Brown trigonal pyramidal crystals of differing size appeared within one to seven days in a variety of conditions (ca. 80% hit rate in the JCSG screen). The biggest and best diffracting crystals were obtained in a solution mixture containing Tris-HCl and MPD (Fig. 29). Within 10 days, crystals achieved their largest size of 100 µm along the longest axis. Crystals were formed in the cubic space group *F*23 with unit cell constants of a = b = c = 236 Å. A dataset of the as-isolated state was refined to a maximum resolution of 1.84 Å (resolution cutoff based on $CC_{1/2}$ (*182*)). Derivatized crystals (Xe-pressurized, CO-incubated and H_2-reduced) diffracted to a maximum resolution of 2.28 Å, 1.99 Å, and 1.94 Å, respectively. Data collection and refinement statistics are reported in Table S2 and Table S3.

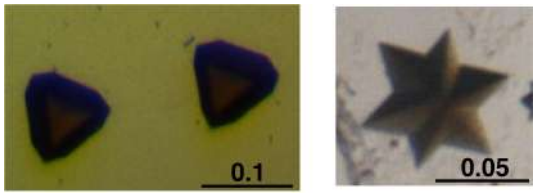

Figure 29. Crystals of *Mb*FRH. *Mb*FRH crystallized in 0.1 M Tris-HCl, pH 7.8 – 8.5, 15 – 40% (v/v) MPD. Scale bar is shown in µm.

The crystal structure of the as-isolated *Mb*FRH was solved by molecular replacement using the homologous *Mm*FRH structure (PDB entry: 4OMF (*77*)) as a search model.

*Mb*FRH and *Mm*FRH share an average sequence identity of 45%. Each asymmetric unit contains one hydrogenase protomer, which is composed of the three subunits: FRH-A, FRH-B and FRH-G (Fig. 30A; Fig. 31A). The crystallographic symmetry generates a dodecameric ball-shaped arrangement with a diameter of ca. 190 Å. The dodecamer is consistent with a mass of approx. 1.2 MDa, which is found for the homologous enzymes from *M. marburgensis (77)*, *M. thermoautotrophicum (178), M. voltae (179), M. jannaschii* (*180*) and *M. formicicum (177)*. The dodecamer interior is solvent-accessible and can be reached through two pores of ca. 3 Å and 9 Å in diameter, which are created at the three-fold axis point of coincidence for the three FRH-A and three FRH-B subunits, respectively (Fig. 30B).

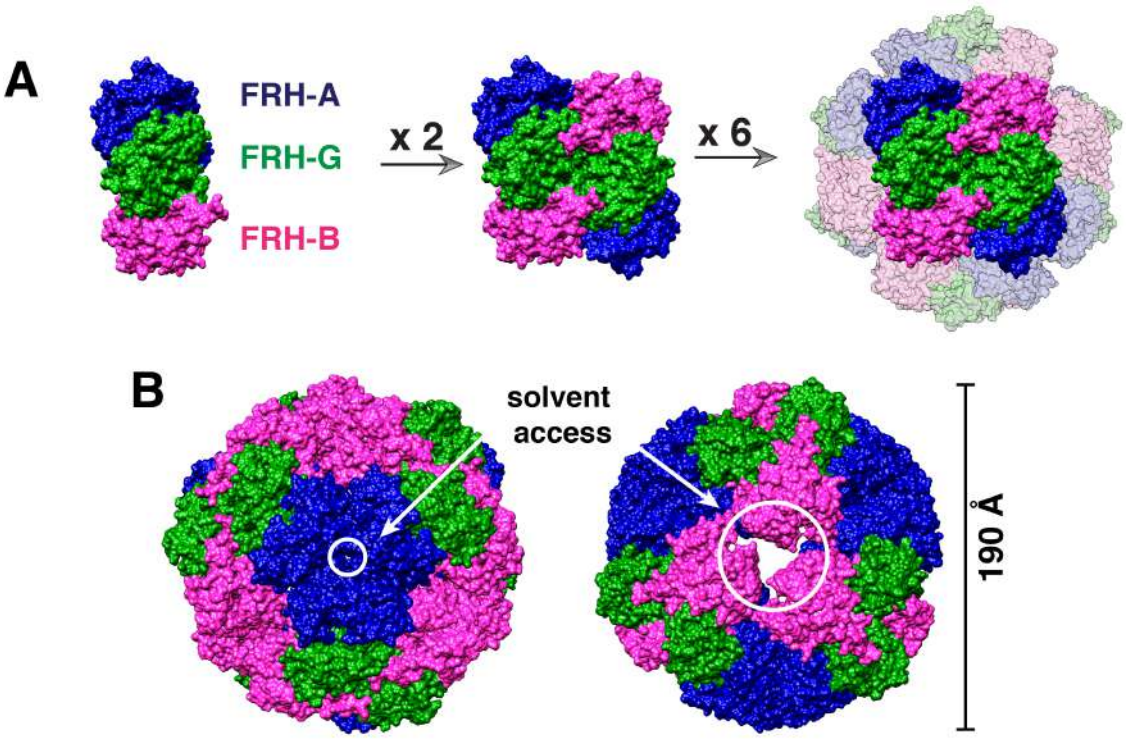

Figure 30. Dodecamer composition of *Mb*FRH. (A) The protomer of *Mb*FRH is a heterotrimer, consisting of the subunits FRH-A, FRH-G and FRH-B, represented as surfaces in navy blue, dark green and violet respectively. (B) Two pores with a diameter of 3 Å (left) and 9 Å (right) are formed at the 3-fold axis, where three FRH-A and three FRH-B subunits assemble, respectively.

FRH-A is homologous to the large subunit of bacterial [NiFe] hydrogenases (*8*) and contains a [NiFe] active site and single octahedrally-coordinated Fe ion (Fig. 31B). FRH-A consists of 456 amino acids, of which 435 residues are resolved in the electron density map. The remaining unresolved 21 residues are located at the C-terminus and cleaved by

an endopeptidase (encoded by *frhD* gene) during maturation (*84, 183*). The structure of the FRH-A subunit can be divided into four tightly interacting domains: the terminal domains I (residues 2 – 38; 402 – 438) and II (residues 39 – 88; 240 – 246; 354 – 401), the four-helix bundle (residues 89 – 211; 328 – 353) and the insertion domain (residues 212 – 239; 246 – 327) (designation as in Vitt *et. al.* (*77*)). Both terminal domains are composed of a β-meander and several α-helices, whereas the insertion domain is mainly composed of structurally disordered regions. Compared to the large subunit of bacterial hydrogenases, FRH-A is ca. 100 residues shorter, which results from deletions scattered throughout the sequences (114 residues short in [NiFeSe] hydrogenases from *D. vulgaris (184)* and 98 residues short in [NiFe] hydrogenase from *D. gigas (185)*). The truncation of the insertion domain as well as a partial deletion of the connecting loop between the helices of the four-helix bundle domain is mostly responsible for shortening of FRH-A sequence.

FRH-G is the smallest of the three subunits and consists of 259 amino acids, of which 253 are defined in the electron density (Fig. 31B). FRH-G contains two domains: the N-terminal domain with a flavodoxin-like fold (residues 18 – 165), harboring the proximal [4Fe4S] cluster, and the C-terminal ferredoxin-like domain (residues 188 – 270), which contains the binding motifs for medial and distal [4Fe4S] clusters, as well as two coordinating cysteines for a [2Fe2S] cluster bound at the interface between two FRH-G subunits.

FRH-B is an iron-sulfur flavoprotein of 291 amino acids, containing a mixed eight-stranded β-sheet flanked by six helices (residues 1 – 140; 206 –253) at its core and carrying a [4Fe4S]-cluster and one FAD molecule (Fig. 31B). All residues were resolved in the electron density. FRH-B is a member of the F_{420}-binding protein family and is typically found in archaea (*84*). FRH-B does not have any identified bacterial homologues.

The fold and arrangement of all three subunits of *Mb*FRH is very similar to the structure of *Mm*FRH (*77*). Major differences are localized to the FRH-A and FRH-G subunits. Two structural elements, comprising two ß-hairpins (residues 208 – 223; 272 – 293), and one disordered loop region (residues 120 – 131), were newly identified in the insertion and four-helix bundle domains of the FRH-A subunit, respectively (Fig. S19A). An additional 15-Å long helix was observed at the C-terminus of the FRH-G subunit (Fig. S19A). All new elements are positioned on the exterior of the dodecamer and do not alter the arrangement of the main chains (Fig. S19B).

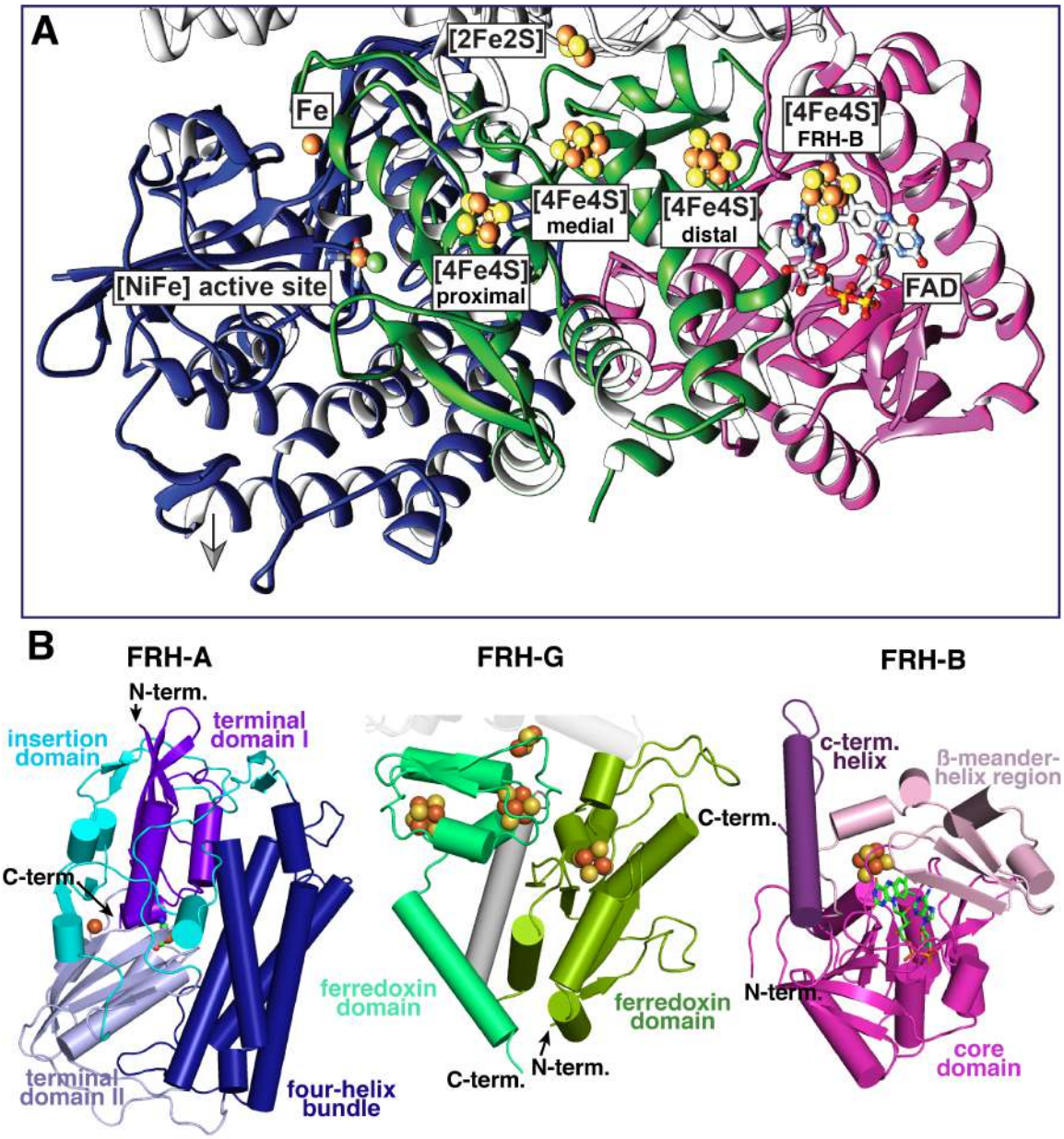

Figure 31. Crystal structure of the *Mb*FRH protomer. (A) Overall structure of the *Mb*FRH protomer. Three subunits are denoted in navy blue, green and violet for FRH-A, FRH-G and FRH-B, respectively. The series of the conventional [4Fe4S] clusters connect the heterobimetallic [NiFe] active site with the FAD molecule. The [2Fe2S] cluster covalently bridges two protomers. (B) Different domains of each subunit are depicted in different colors. The domain naming uses the convention established for *Mm*FRH (*77*). [4Fe4S] and [2Fe2S] clusters, single Fe and [NiFe] active sites are shown as spheres (yellow for S, orange for Fe and green for Ni). The FAD molecule is shown as sticks.

3.4.3 PRODUCT OF THE *frh*ADGB operon

As for most methanogenic archaea (*186, 187*) *M. barkeri* contains two F_{420}-reducing [NiFe] hydrogenases. These structural genes are encoded by two operons (*183*), designated *frh*ADGB (UniProt gene annotations: MSBRM_3020–3017) and *fre*AEGB (UniProt gene annotations: MSBRM_1453–1455), both of which are transcribed during

growth on MeOH (*188*). The corresponding subunits of both operons share over 90% sequence identity. The electron density map of the 1.84 Å crystal structure has sufficient structural detail to distinguish between many amino acid side chains (e.g. between Ser232 and Phe370 in FRH-A; Gly190 and Arg174 in FRH-G; Fig. S20). Furthermore, S-anomalous data collected at a wavelength of 1.900 Å also provided unbiased confirmation of the methionine sulfur positions in the structure. Thus, *Mb*FRH characterized in this work has been undoubtedly identified as a product of the *frh*ADGB operon.

The reported Uniprot sequence for MSBRM_3020 includes 318 amino acids. In the experimental electron density map of FRH-A, an additional 139 N-terminal residues are clearly observed. The erroneous sequence deposition could be the result of the inaccurate identification of the FRH-A start codon in the *frh*ADGB operon open reading frame (*183*).

3.4.4 SUBSTRATE CHANNELING

Hydrophobic gas channels were visualized by Xe derivatization of the *Mb*FRH crystals. The solvent accessible surface of *Mb*FRH contains two channels leading from the enzyme exterior to the [NiFe] active site (Fig. 32A). The first channel (a canonical hydrophobic channel) is 20 Å long and runs along the interface between the FRH-A and FRH-G subunit, which is analogous in position to the gas channels observed in bacterial [NiFe] hydrogenases (*87, 90*) and those proposed for *Mm*FRH *(77)*.

A second gas channel that is 25 Å long and cuts through the FRH-G subunit has been newly identified where all seven Xe molecules were observed. Surprisingly, the unrelated [NiFeSe] hydrogenase from *D. vulgaris* Hildenborough (group 1) (*189*) contains a similar hydrophobic tunnel presumably used for H_2 transfer, but in the homologue *Mm*FRH, the channel is constricted (Fig. 32B). Further structure comparison between *Mm*FRH and *Mb*FRH revealed that amino acids lining the second channel are similar in their hydrophobicity, but not highly conserved (Fig. S21). While the crystal structure represents a static view of a protein state, it is possible that the second channel in *Mb*FRH that was not identified in the previously published structure of *Mm*FRH *(77)* is functional *in vivo*.

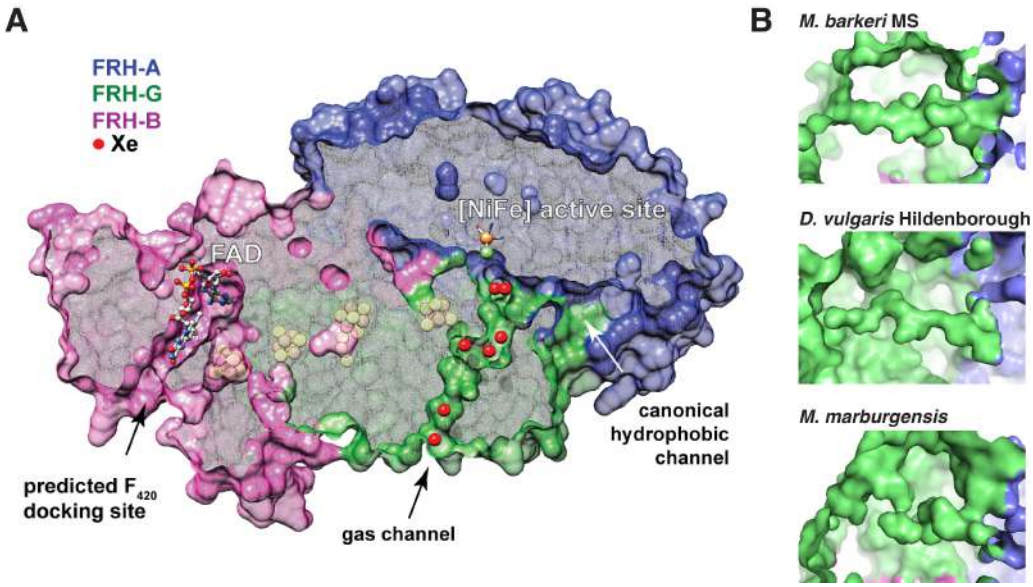

Figure 32. Hydrophobic gas channels. (A) Seven Xe atoms (shown as red spheres) were identified within the 25 Å long narrow channel located within the FRH-G subunit. (B) Comparison of [NiFe] hydrogenases revealed the presence of a similar noncanonical channel in [NiFeSe] hydrogenase from *Desulfovibrio vulgaris* Hildenborough (PDB entry: 3ZEA (*189*)), whereas in *Mm*FRH such a channel may be interrupted (PDB entry: 4OMF (*77*)). FRH-A, FRH-B and FRH-G are represented as surfaces and colored navy blue, violet and green, respectively.

3.4.5 ELECTRON TRANSFER CHAIN

One *Mb*FRH protomer contains seven metal cofactors and one FAD molecule, each located within electron transfer distance to its nearest neighbor (Fig. 33). Five of these metal cofactors are represented by four conventional cysteine-coordinated [4Fe4S] clusters and one heterobimetallic [NiFe] active site. This part of the electron transfer chain is also found in *Mm*FRH (*77*).

In group 3 [NiFe] hydrogenases, FAD interacts directly with coenzyme F_{420} and enables its redox conversion (*181*). *Mb*FRH is a group 3a [NiFe] hydrogenase (*8*) and couples the reversible oxidation of H_2 to the reduction of F_{420} (*190*). This model is also supported by the equivalent forward and backward reaction rates of 225 s^{-1} measured *in vitro (191)*. However, it is anticipated that *in vivo Mb*FRH is skewed towards H_2 production (*176*). Due to the spatial distance of ca. 50 Å between the two reaction centers of F_{420} and H_2 redox conversion, a chain of the redox active metal clusters is needed to mediate intramolecular ET between these two reaction sites.

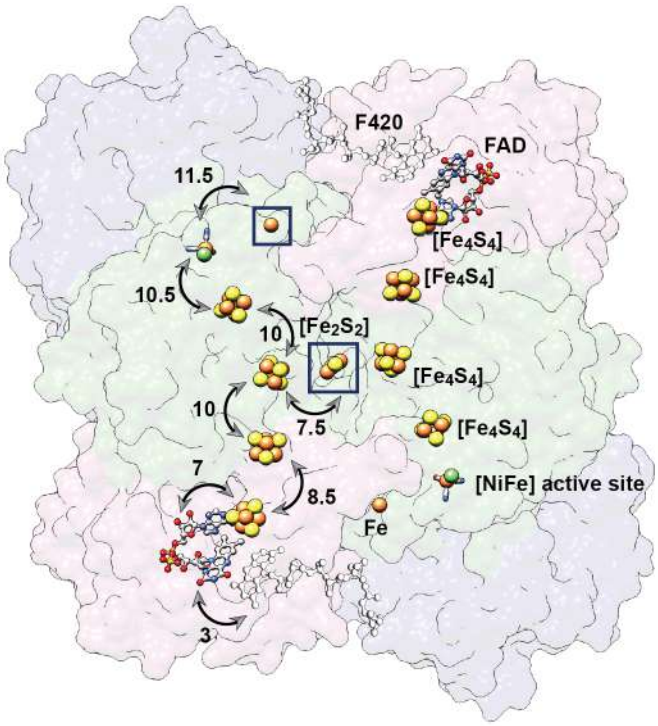

Figure 33. Extended electron transfer pathway. A chain of iron-sulfur clusters facilitates reversible ET (double arrows) between the coenzyme F_{420} and the [NiFe] active. Distances are given in Angstrom. Iron-sulfur clusters and single metals are shown as spheres (Fe in orange, S in yellow, Ni in green). FAD and F_{420} are shown in ball and sticks representation. F_{420} was not observed in the crystal structure and is modeled manually in Coot at the position previously suggested by Vitt et *al. (77)*.

The remaining two metal cofactors identified in *Mb*FRH include a single Fe in a close proximity to the [NiFe] active site, and a [2Fe2S] cluster located at the interface between two FRH-G subunits (Fig. 33). Short Fe-to-Fe distances between the two medial [4Fe4S] clusters (7.5 Å) enable the electron shuttling between individual ET chains of each FRH protomer. Positions of the sulfur and iron atoms were identified by anomalous scattering experiments. In the protein structure of homologous *Mm*FRH, the position of the mononuclear Fe is occupied by a Mg ion and the Fe atoms of the [2Fe2S] cluster are replaced by Zn (*77*). The Cys191-X-Cys193 binding motif for the [2Fe2S] cluster in *Mb*FRH is highly conserved among other [NiFe] hydrogenases of group 3, thus the presence of zinc(II)hydrogensulfide in *Mm*FRH is likely a purification artifact and has no biological significance. Key cofactors in the electron transfer chain will be discussed in further detail in the following chapters.

3.4.5.1 FAD

The FAD molecule is located in the FRH-B subunit in an atypical back-folded

conformation, which positions adenine-C^6 and the isoalloxazine dimethylbenzyl-C^{8M} in close proximity (3.5 Å) (Fig. 34A). FAD is positioned within an efficient electron transfer distance of 7 Å to the nearest [4Fe4S] cluster in FRH-B. An electronic conduit to the [NiFe] active site is formed by the three [4Fe4S] clusters of the FRH-G subunit. The isoalloxazine ring of the FAD is planar and solvent-accessible from the exterior of the spherical dodecamer complex. Similar to the *Mm*FRH structure, (*77*) the *re*-face of FAD seems to be partially shielded by Val215 of the FRH-B subunit, whereas the *si*-face is exposed to solvent and could therefore potentially bind coenzyme F_{420}. Neither co-crystallization nor soaking of crystallized *Mb*FRH with coenzyme F_{420} provided evidence of a F_{420} binding site, indicating a weak or transient interaction of coenzyme F_{420} with the conformation of *Mb*FRH found in the crystal.

Resonance Raman (RR) spectroscopy of single crystals at 80 K exhibit the characteristic signals of the FAD isoalloxazine ring. The spectral signature is very similar to the signals of the oxidized FMN in solution, indicating that FAD is oxidized in the as-isolated state of *Mb*FRH (Fig. 34B). EPR spectra of the FRH-enriched sample revealed a typical isotropic signal of a semiquinone free radical with $g_x = 2.003$, which provides additional support to the FAD assignment (Fig. S22; Table S4).

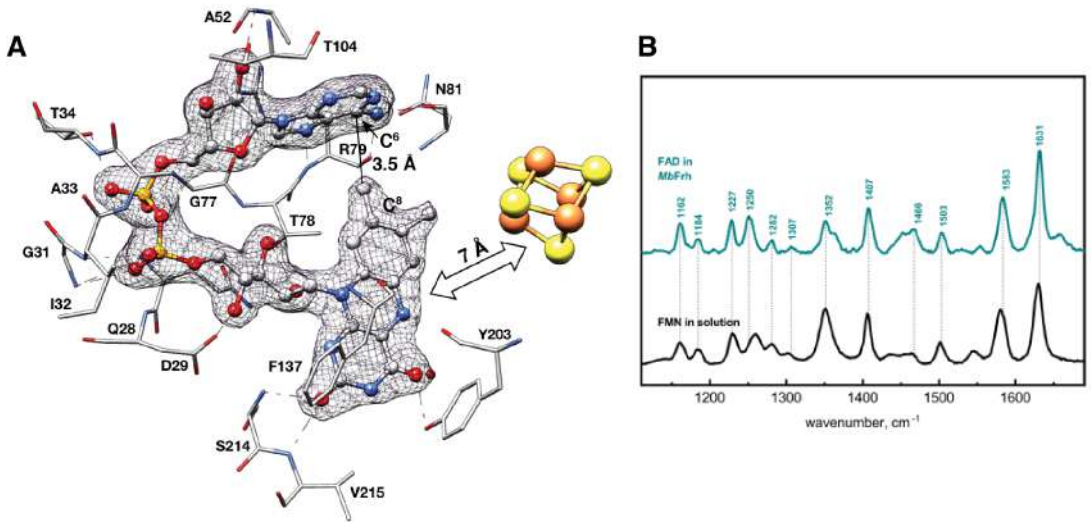

Figure 34. FAD environment. (A) Residues lining the FAD binding pocket are shown as sticks. The $2F_o$-F_c map after full refinement is shown as gray mesh (1.0 σ). (B) RR spectra of *Mb*FRH in the high frequency region (green line) exhibits the characteristic signals of the isoalloxazine motif of FAD in comparison to those of flavin adenine mononucleotide (FMN) in solution (black line). RR spectra were recorded at 80 K using a 458 nm laser excitation by Christian Lohrent (Institut für Chemie, Technische Universität Berlin) and normalized with respect to the most intense signal at 1630/1632 cm^{-1} (*192*). Figure B was obtained by courtesy of Christian Lohrent.

3.4.5.2 [2Fe2S] CLUSTER

The solvent-exposed [2Fe2S]-cluster is observed at the two-fold axis at the interface between two FRH-G subunits and covalently links them (Fig. 35A,B). Each Fe atom of [2Fe2S] cluster is coordinated by two conserved cysteine residues, derived from a Cys191-X-Cys193 motif. In addition to anomalous scattering (Fig. 35C,D), the [2Fe2S] cluster was also detected in solution-phase EPR experiments (Fig. S22; Table S4). The sample exhibited a rhombic EPR signal with $g_x = 2.016$, $g_y = 1.982$ and $g_z = 1.946$, which support the presence of a reduced $[2Fe2S]^+$ cluster in FRH-ABG at the as-isolated state.

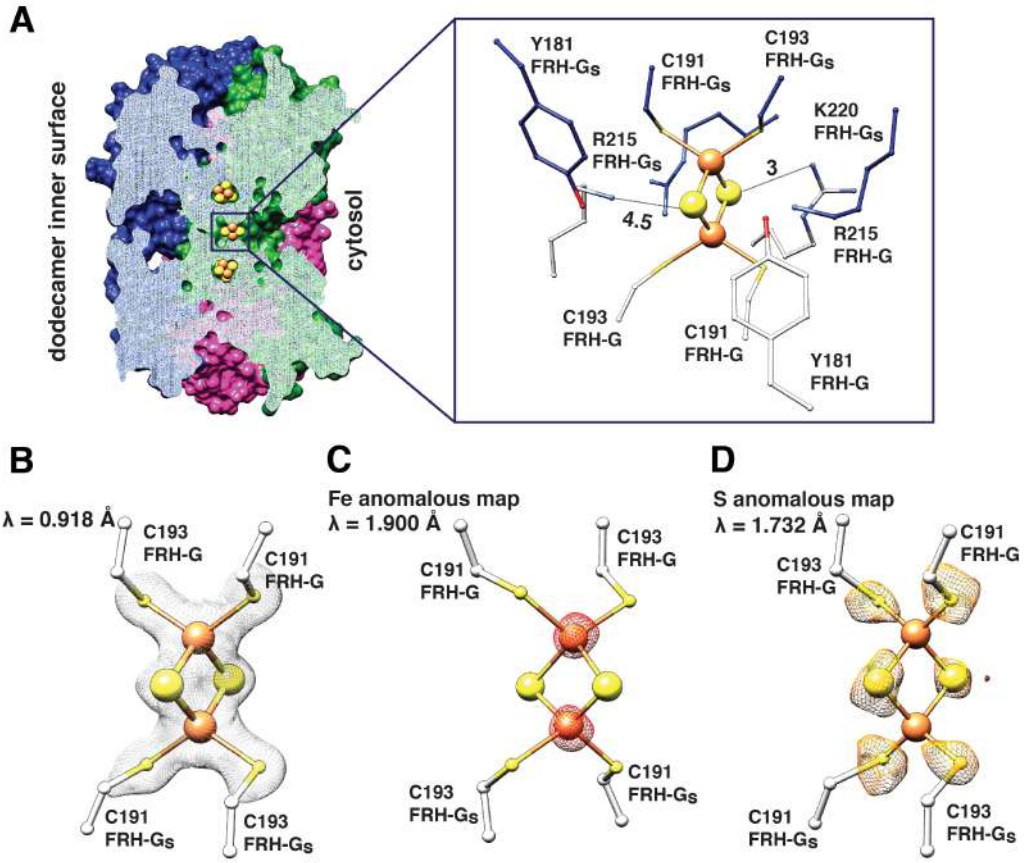

Figure 35. Structure of the bridging [2Fe2S] cluster. (A) The cysteine-coordinated [2Fe2S] cluster is solvent accessible and covalently links two FRH-G subunits at the two-fold symmetry axis of *Mb*FRH protomers. FRH-A (blue), FRH-B (violet), and FRH-G (green) subunits are represented as surfaces. Inset: second coordination sphere of the [2Fe2S] cluster. Fe (yellow) and S (orange) atoms are shown as spheres. Amino acid residues of the different FRH-G subunits (denoted as FRH-G and FRH-G$_S$) are shown as sticks. The electron density maps are shown as mesh: (B) $2F_o$-F_c map after full refinement in gray (1.8 σ), (C) Fe anomalous difference map in orange (7.0 σ) and (D) S anomalous difference map in yellow (3.0 σ)).

The second coordination sphere of the [2Fe2S] cluster is mainly composed of positively charged amino acids, such as Arg215 and Lys220 (Fig. 35A; inset). These positively charged residues at less than 4.5 Å distance likely stabilizes the reduced $[2Fe2S]^{+}$-state of the cluster together with hydrogen bonds.

3.4.5.3 MONONUCLEAR Fe SITE

A single Fe ion was found at a distance of 11.5 Å from the [NiFe] active site (Fig. 36).

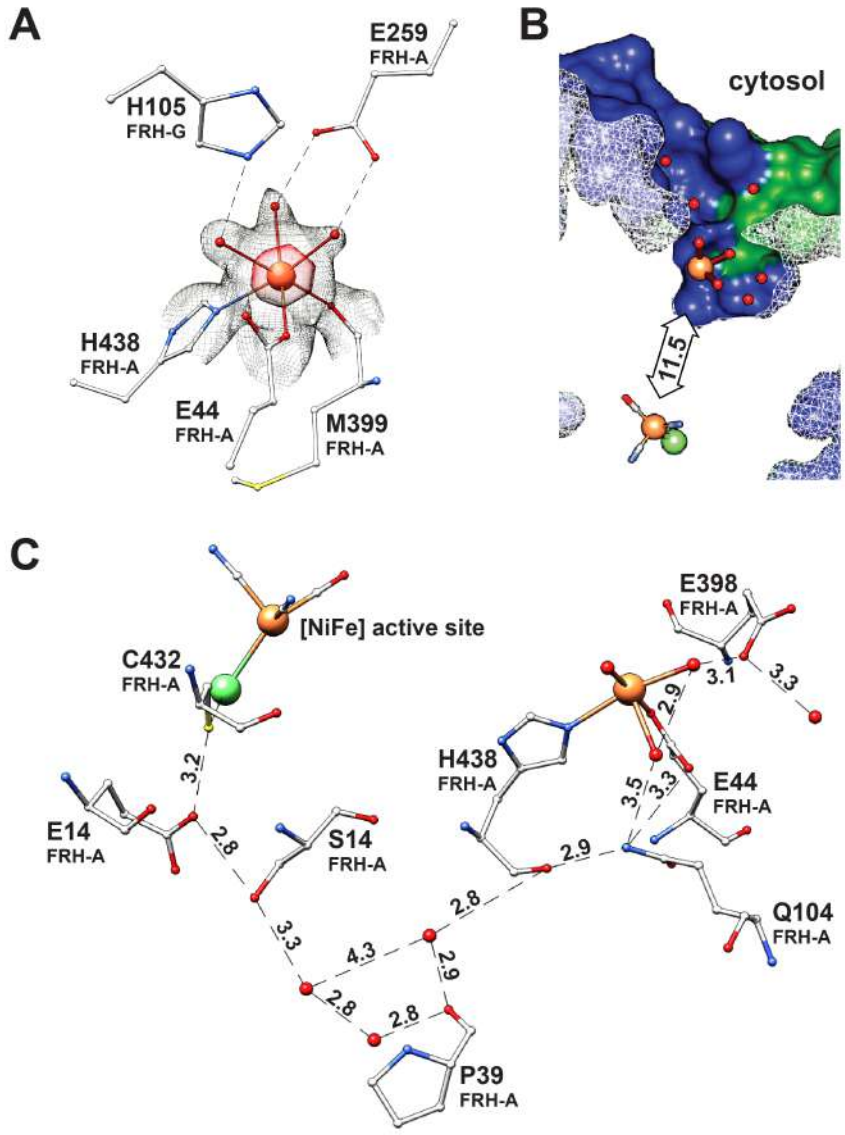

Figure 36. Mononuclear Fe site. (A) Coordination of the single Fe. The $2F_o$-F_c electron density map after full refinement is shown in gray (1.1 σ). The Fe anomalous difference map is shown as a red surface (8.0 σ). (B) The single Fe is located within a hydrophilic channel approximately 11.5 Å from the active site (C) and could play a role in one of the proposed proton transfer pathways in group 1 [NiFe] hydrogenases (*89*). Distances are stated in Angstrom. Metal ions and amino acids are represented as spheres (green for Ni and orange for Fe) and sticks, respectively.

The single Fe ion is octahedrally coordinated by the side chains of Glu44 and His438, the carbonyl-oxygen of Met399 and three water molecules (Fig. 36A). A hydrophilic channel was identified leading to the Fe ion (Fig. 36B). The residues Glu44 and His438 are highly conserved among [NiFe] hydrogenases of different groups (Tab. 3). The position of Fe^{2+} is either occupied by Mg^{2+} in *Mb*FRH (*77, 184*) or a Ca^{2+} ion (*92*) in other [NiFe] hydrogenases. The identities of the mononuclear ions of the so far reported hydrogenase crystal structures are summarized in Table S5. The single ion is hypothesized to stabilize proton transfer pathways (Fig. 36C) (*89*). Interestingly, a single Fe had previously been identified in oxygen-tolerant [NiFeSe]-hydrogenases from *D. baculatum (193)* and *D. vulgaris* Hildenborough *(73)* (Tab. S5). However, the correlation between the presence of the single Fe and oxygen tolerance was not conclusive. In fact, the exposure of the FRH-enriched sample to atmospheric oxygen even for 10 seconds lead to an immediate and complete loss of the H_2-dependent MV-reducing activity, which could be partially recovered (up to 10%) after several hours of incubation under anoxic atmosphere with 2% H_2. Due to its unique proximity to the main ET chain, it is reasonable to assume that the single Fe site could participate in H_2 redox catalysis.

3.4.5.4 [NiFe] ACTIVE SITE

[NiFe] active site found in the as-isolated state contains the consensus structural properties found in other [NiFe] hydrogenases (*8*). The Ni ion is coordinated by four strictly conserved cysteine thiolate groups (Cys63, Cys66, Cys432, Cys435), where Cys66 and Cys435 act as bridging ligands to the Fe ion (*8*) (Fig. 37A). Additionally, the Fe atom is coordinated by three diatomic inorganic ligands assigned to two CN^- and one CO by IR spectroscopy (*72*). No electron density is detected in the third bridging position between Ni and Fe ions in *Mb*FRH (Fig. 37B), which would be indicative of an inactive enzyme state, such as Ni-A or Ni-B states (*8*), at the given resolution of 1.84 Å.

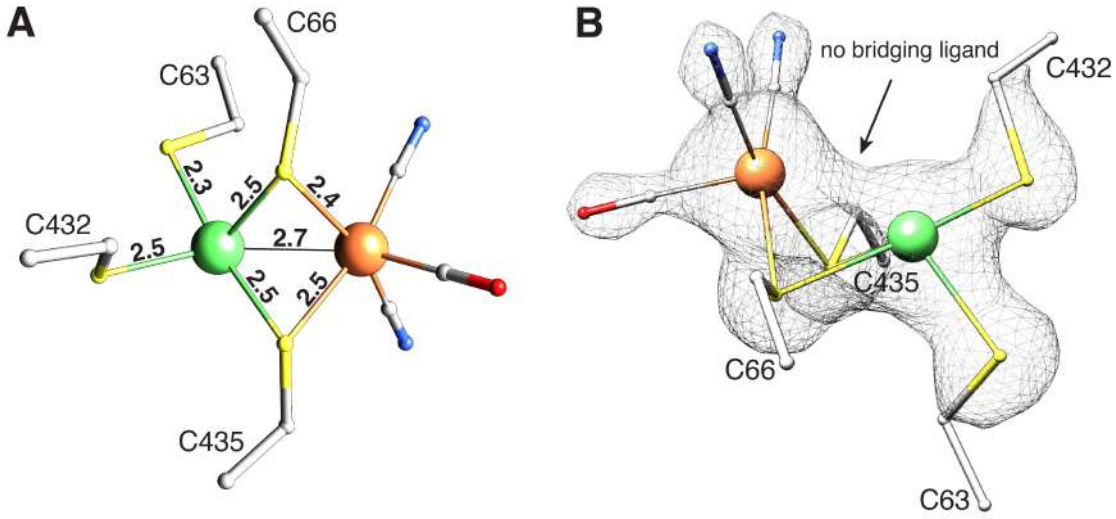

Figure 37. Crystal structure of the [NiFe] active site. (A) The [NiFe] active site is coordinated by four conserved cysteine thiolate groups and three diatomic inorganic ligands (two CN^- and one CO). Interatomic distances are indicated in Angstrom. (B) Vacant coordination site between the Ni and Fe ions was observed. The $2F_o$-F_c electron density map after full refinement is shown as a gray mesh (1.8 σ). Metals and amino acid residues are shown as spheres (Ni in green, Fe in orange (A) and gray (B), S in yellow) and sticks, respectively.

Consistently, the distance between Ni and Fe ions is 2.7 Å, which is shorter than distances found in the bridged unready Ni-A or ready Ni-B states (*8*). Although previous crystal structures of the inactive (Ni-A (*94, 194*) or Ni-B (*75*)) and active (Ni-R (*89*)) states revealed square pyramidal Ni coordination (Fig. 38B-D), the [NiFe] active site in *Mb*FRH exhibits a rather unusual seesaw-shaped geometry with a *trans* S_{Cys435}-Ni-S_{Cys63} angle of 107° and *trans* S_{Cys432}-Ni-S_{Cys64} angle of 171° (Fig. 38A). The vacant bridging position, together with the unusual Ni coordination geometry, suggests that the cluster is in the active Ni-S state. This state is structurally uncharacterized and EPR-silent, as suggested by previous spectroscopic analyses (*8, 100-102*). Stretching vibrations of Fe-coordinating inorganic ligands are highly sensitive towards the electronic changes at the [NiFe] center; so vibrational spectroscopy (e.g. IR and RR) is a very reliable technique for redox state determination as compared to X-ray crystallography. To this end, the spectral fingerprint of the Fe-CO and Fe-CN metal-ligand vibrations in the relevant spectral range was compared to the previously characterized hydrogenase systems of known redox states.

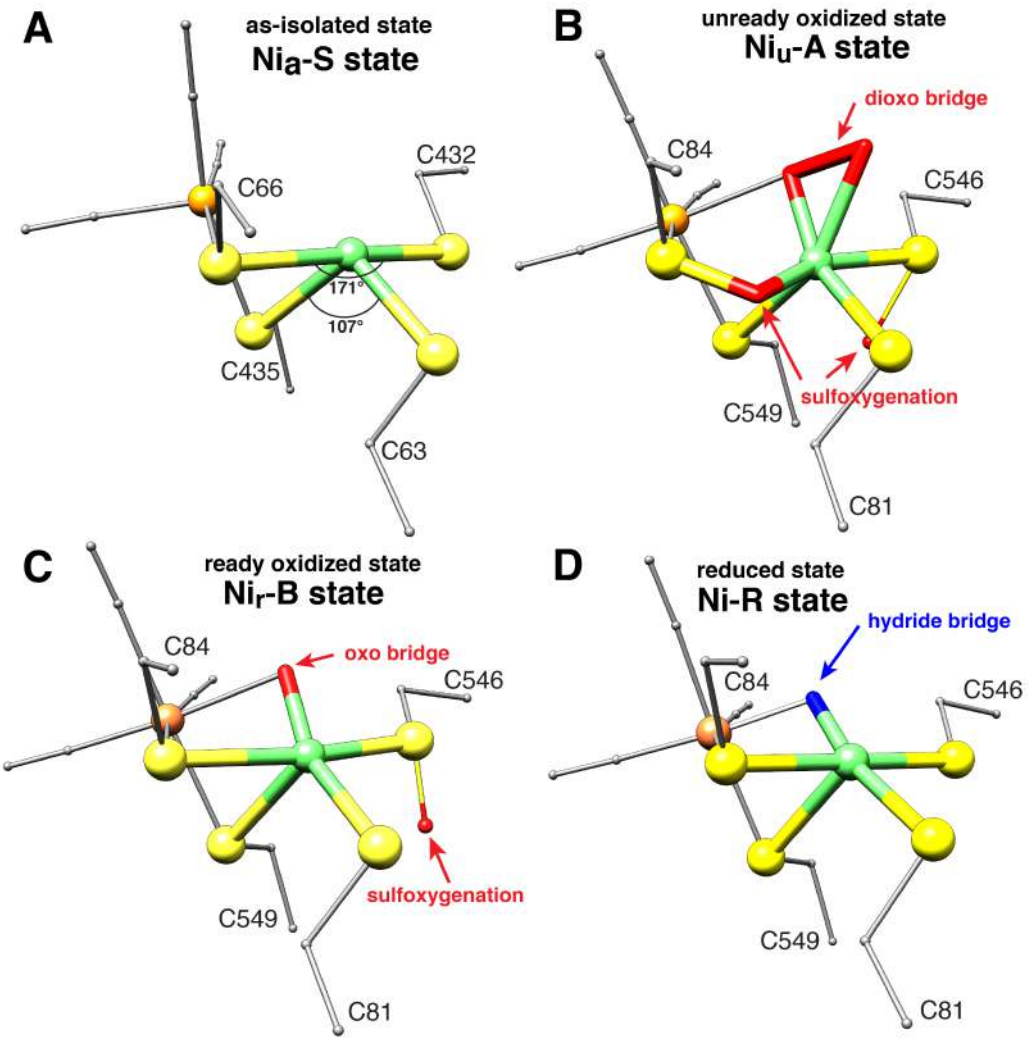

Figure 38. Comparison between crystallographically characterized catalytic states of [NiFe] active site. (A) The Ni_a-S state of the [NiFe] active site exhibits a distorted seesaw coordination geometry with a vacant coordination site between the Ni and Fe ions (this study; Fig. 37B). Square pyramidal Ni coordination is observed in Ni-A (B), Ni-B (C) and reduced Ni-R (D) states, with various bridging ligands between the metal ions. Metals and amino acid residues are shown as spheres (Ni in green, Fe in orange, S in yellow, H^- in blue and O in red) and sticks, respectively. Catalytic states depicted in here were observed in the crystals structures of *Mb*FRH (A) and in the [NiFe] hydrogenase from *D. vulgaris Miyazaki* F (PDB entries: 1WUI (B) (*75*); 1WUJ (C) (*75*); 4U9H (D) (*89*)).

3.4.6 VALIDATION OF Ni_a-S STATE

IR and RR spectroscopic analyses were performed on single *Mb*FRH crystals under anoxic conditions. *Mb*FRH crystals were prepared in a similar manner before harvesting for X-ray crystallographic and vibrational spectroscopic analysis. The principal experiments of IR/RR spectroscopies were conducted and analyzed by the research group of Dr. Ingo Zebger (Institut für Chemie, Technische Universität Berlin).

IR spectra of a single *Mb*FRH crystal recorded at 80 K revealed three characteristic signals at 1945 cm^{-1} and 2065/2080 cm^{-1}, corresponding to the stretching vibrations of CO and vibrationally coupled CN^- stretches, respectively (Fig. 39A). This IR signature strongly resembles the IR fingerprint of the Ni-S state for the as-isolated regulatory hydrogenase from *R. eutropha* (*Re*RH) with absorption maxima of 1943 cm^{-1}, 2072/2081 cm^{-1} (*101*). The Ni-C and Ni-L states can be excluded based on the distinct position of the CO vibration, which shifts higher for the Ni-C state (1961 cm^{-1} for *D. vulgaris* and *R. eutropha*) and lower for the Ni-L state (1911 cm^{-1} for *D. vulgaris;* 1898 cm^{-1} for *A. vinosum*) (*8*). The fully reduced Ni-R state exists in up to three isoelectronic subforms (Ni-R_I, Ni-R_{II} and Ni-R_{III}), each with distinct spectral signatures (*8, 195*).

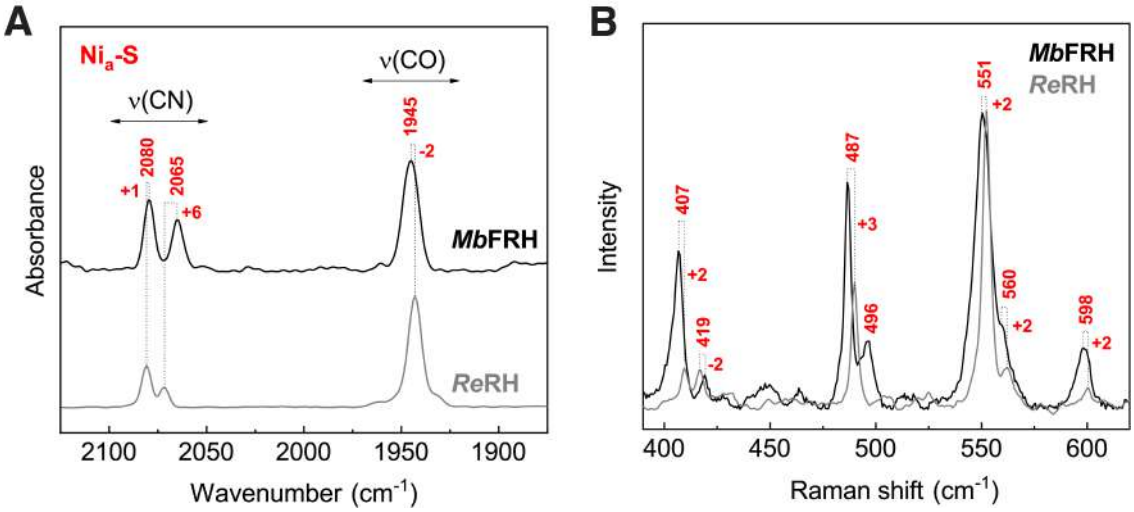

Figure 39. Vibrational spectra of the Ni_a-S state. (A) IR spectra of *Mb*FRH in a single crystal (at 80 K, black) and a protein solution of *Re*RH in the Ni_a-S state (10°C, gray). Spectra were normalized with respect to the CO stretching band intensity. (B) RR spectrum of an *Mb*FRH single crystal (black) compared to the protein solution of *Re*RH at the Ni_a-S state (gray). RR spectra were recorded at 80 K using an 568 nm laser excitation and normalized with respect to the most intense signal at 551/553 cm^{-1}. Spectra were recorded by Christian Lohrent (Institut für Chemie, Technische Universität Berlin). The figure was obtained by courtesy of Christian Lohrent.

The Ni-R_I state stretching frequencies observed in several [NiFe] hydrogenases (e.g. 1948 cm^{-1}, 2061/2074 cm^{-1} in *D. vulgaris*; 1940 cm^{-1}, 2060/2073 cm^{-1} in *D. gigas*) strongly resembles the spectral fingerprint of the Ni-S state (*195*). Thus, the Ni-R state cannot be excluded based on the IR spectroscopic data alone (*8, 195*), but in combination with RR spectroscopic analysis. The RR spectrum of the *Mb*FRH crystal in the as-isolated state exhibits very similar positions for the Fe-CO and Fe-CN stretching frequencies ($\Delta\nu \approx \pm 3$ cm^{-1}) compared to the Ni_a-S state of a *Re*RH and membrane-bound

hydrogenase from *R. eutropha* (*Re*MH) (*102, 196*) (Fig. 39B). The contribution from further-reduced species can be ruled out, since both Ni-R and Ni-C undergo photoconversion to the Ni-L state by the RR beam at 80 K. The spectral signature of *Re*RH at Ni-L state is distinct from the spectrum recorded for *Mb*FRH (*102, 104*).

Further evidence for the Ni-S state comes from structural analysis of single crystal after CO-derivatization. Electron density was observed above the Ni atom upon incubation of the as-isolated *Mb*FRH crystal with pure CO atmosphere for ca. 30 hours (Fig. 40A). The resultant species had a similar CO-binding geometry (Ni-C-O angle of 162°; Fig. S23) to the axial Ni position as was previously observed in CO-inhibited [NiFe] hydrogenase from *D. vulgaris* Miyazaki F (*103*). No significant change in the Ni-Fe distance was observed at the experimental resolution (d_{min} = 1.99 Å) when compared to the Ni-Fe distance in the Ni_a-S state.

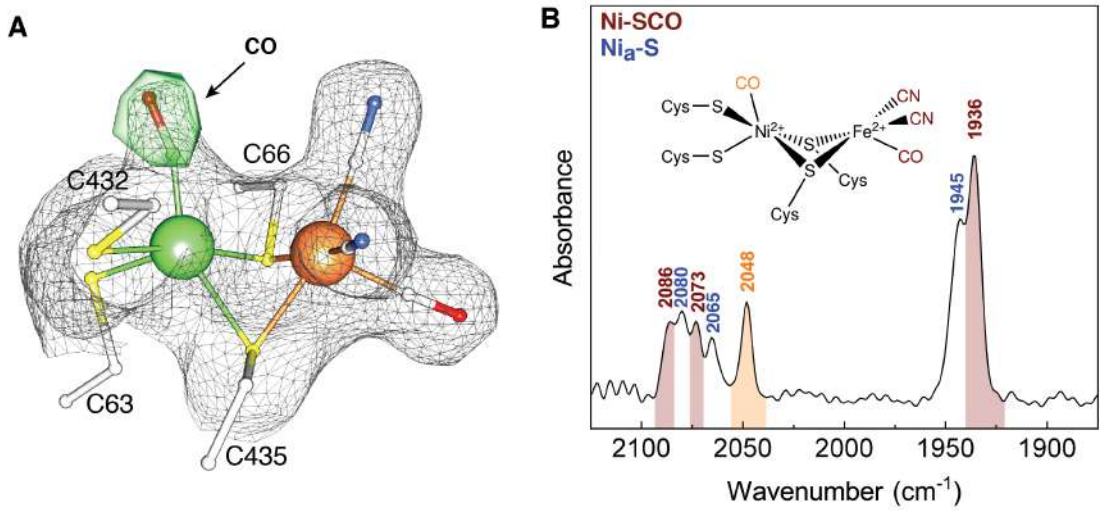

Figure 40. CO inhibition of the [NiFe] active site (d_{min} = 1.99 Å). (A) The $2F_o$-F_c electron density map after full refinement (1 σ) and residual F_o-F_c map (5.5 σ) before CO-modeling are shown as gray mesh and green surface, respectively. Metals and amino acids are shown as spheres (Ni in green, Fe in orange, S in yellow) and ball-and-stick, respectively. (B) IR absorbance spectrum of a *Mb*FRH single crystal was recorded at 80 K by Christian Lohrent (Institut für Chemie, Technische Universität Berlin). Bands corresponding to the intrinsic, Fe-bound diatomic ligands and the extrinsic, Ni-bound CO of the Ni-SCO state are highlighted in brown and orange, respectively. Bands corresponding to the Ni_a-S state are indicated by the stretching frequencies colored in blue. Figure B was obtained by courtesy of Christian Lohrent.

Binding of extrinsic CO to the open Ni coordination site (yielding the EPR silent Ni-SCO state) has been demonstrated in the Ni_a-S state, but binding is prohibited for the reduced, hydride-bridged Ni-R and Ni-C states (*197*). In addition to the X-ray crystallographic evidence, the Ni-SCO state was confirmed by IR spectroscopy. The IR spectrum of the

*Mb*FRH single crystal exhibited a high-frequency CO stretching band at 2048 cm^{-1}, which has also been observed for other [NiFe] hydrogenases in the Ni-SCO state (*197, 198*) (Fig. 40B). The refinement of the [NiFe] active site revealed that the CO-inhibited species are accumulated to ca. 50% (Fig. S23). A similar observation was confirmed by the IR spectroscopic data, revealing comparable signal intensities of the simultaneously detected absorption maxima corresponding to both the Ni_a-S (1945 cm^{-1}, 2065/2080 cm^{-1}) and Ni-SCO (1936 cm^{-1}, 2073/2086 cm^{-1}) states (Fig. 40B).

3.4.7 GENERATION OF DIFFERENT CATALYTIC STATES IN *Mb*FRH CRYSTALS

Structurally characterizing catalytic intermediates is a challenging task due to their transient nature. Notably, the Ni_a-S state is comparatively stable and has been previously characterized spectroscopically in protein solution (*8*). However, it has not been structurally described thus far. Structural constraints enforced by the protein matrix potentially stabilize the unusual seesaw geometry of the active site in the Ni_a-S state. The crystallization process could provide an additional restraints for the given protein conformation and in case of *Mb*FRH, stabilize the isolated catalytic state. However, the stabilization in the crystal allows sufficient freedom for some structural rearrangements necessary to obtain the geometry of other states in the catalytic cycle.

In an attempt to produce the fully-reduced Ni-R state, the as-isolated *Mb*FRH crystals were incubated in 100% H_2 atmosphere in the presence of oxidized MV as redox mediator. The reduction of MV can be detected over time by a characteristic color change from clear to dark blue (Fig. 41A). The MV/H_2-treated *Mb*FRH crystals diffracted to a maximum resolution of 1.94 Å and had the identical cubic spacegroup and similar cell constants observed for the as-isolated (Ni-S) state (Tab. S3), indicating minimal protein scaffold rearrangement. The Ni-R state is characterized by a hydride bridge between Ni and Fe atoms, short Ni-Fe distances (2.57 Å), and a protonation of one of the Ni-coordinating cysteine thiolate groups (*89*). Consistent with the expectations, the Ni−Fe distance reduced from 2.7 Å (observed in Ni-S state) to 2.62 Å. The presence of the H_2-derived ligands could not be observed in the MV/H_2-treated *Mb*FRH crystal structure due to insufficient resolution.

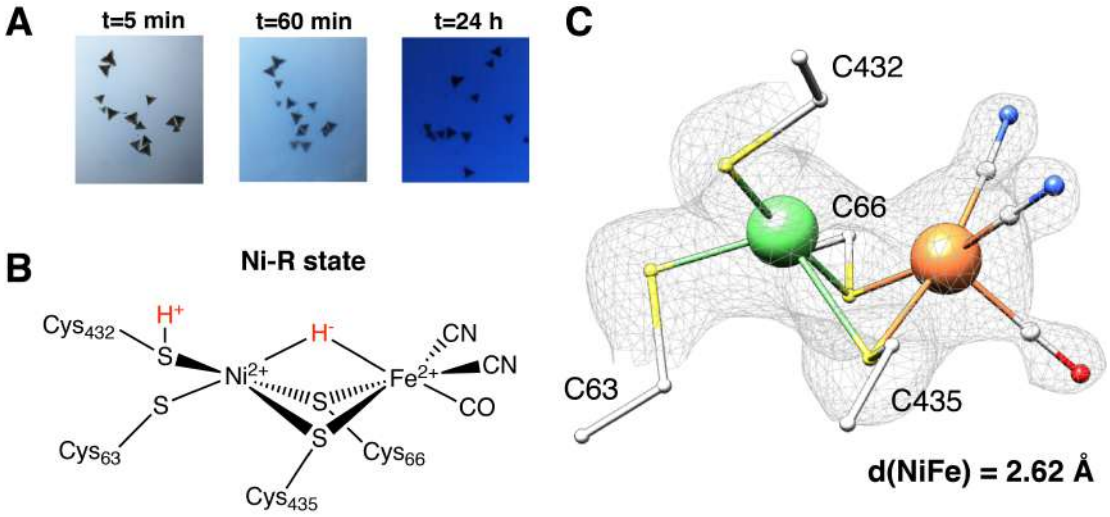

Figure 41. MV-mediated reduction of the *Mb*FRH crystals with H_2 (d_{min} = 1.94 Å). (A) Fully grown *Mb*FRH crystals were placed into a droplet containing reservoir solution supplemented with 10 mM oxidized MV and subsequently incubated in 100% H_2 atmosphere. (B) Representation of the [NiFe] active cite in the fully-reduced Ni-SR state based on the recently-reported high-resolution crystal structure of *D. vulgaris* Miyazaki F (*89*) (C) The X-ray structure of the [NiFe] active site treated with H_2 and MV. The $2F_o$-F_c electron density map (1.5 σ) after full refinement is shown in gray mesh. Metals and amino acids are shown as spheres (Ni in green, Fe in orange, S in yellow) and ball-and-stick, respectively.

Together, these data could indicate the successful conversion to the Ni-R state. However, the estimated overall coordinate error of 0.125 Å based on maximum likelihood places the observed distance change within the standard deviation range (Tab. S3).

Conversion of the Ni-S state to an oxidized state in *Mb*FRH crystals was unsuccessful. In order to oxidize the crystals, potassium hexacyanoferrate(III) ($K_3Fe(CN)_6$) or atmospheric oxygen were used (*99*). Long incubation (up to 2 days) with $K_3Fe(CN)_6$ damaged the crystals, which hindered the interpretation of the electron density and spectra of the active site by X-ray and vibrational spectroscopy, respectively. Short incubation was not sufficient to oxidize the [NiFe] active site, which could be due to slow diffusion of the ferricyanide inside the *Mb*FRH crystals. Similar results were obtained for aerobic inactivation with atmospheric oxygen.

4 SUPPLEMENTARY MATERIAL

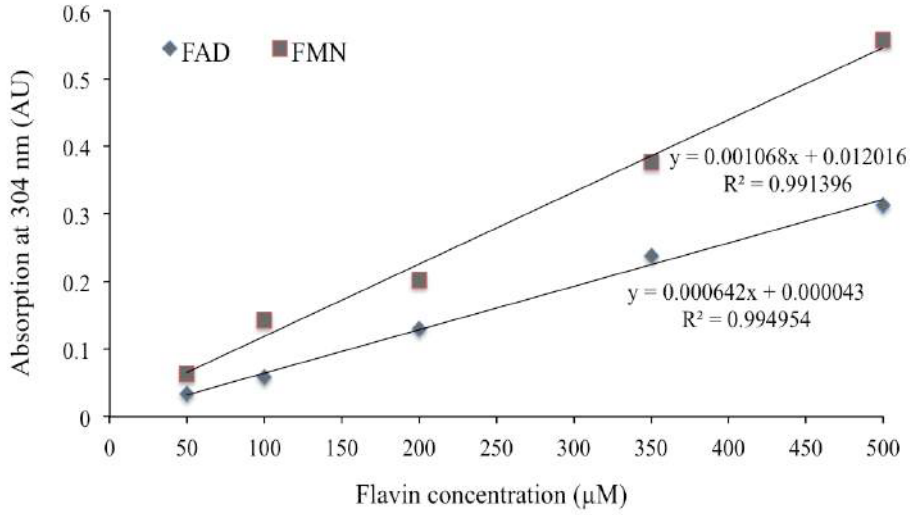

Figure S1. Molar extinction coefficient of FMN and FAD at 304 nm. The measurements were conducted in 50 mM Na-HEPES pH 7.5, 150 mM NaCl at 37°C. The slopes of the Beer´s Law plot indicate the molar extinction coefficients: 642 M^{-1} cm^{-1} for FAD and 1068 M^{-1} cm^{-1} for FMN.

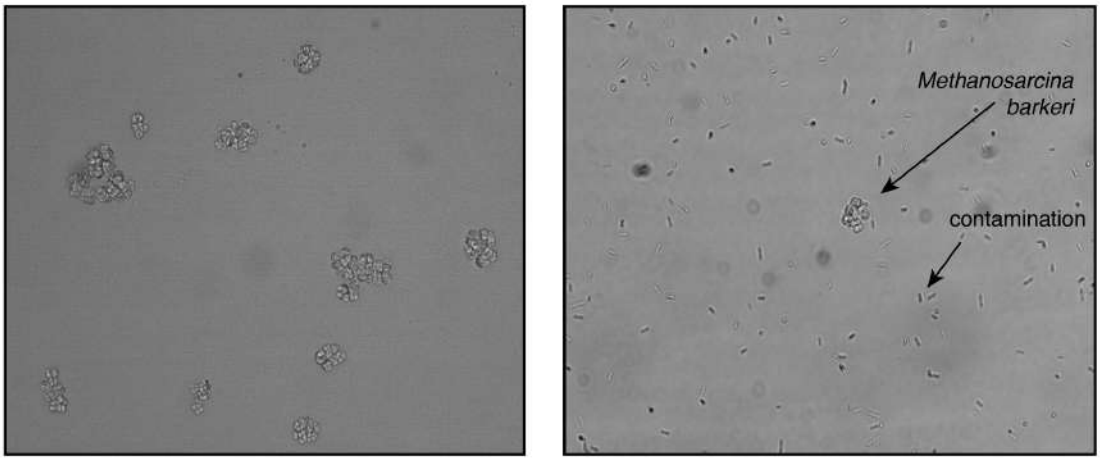

Figure S2. Pure (left) and contaminated (right) cell suspension of *M. barkeri*. 2 µL of cell suspension were placed on a clean microscope slide and covered with a coverslip. The slide was examined at 400 × magnification (Zeiss light microscope).

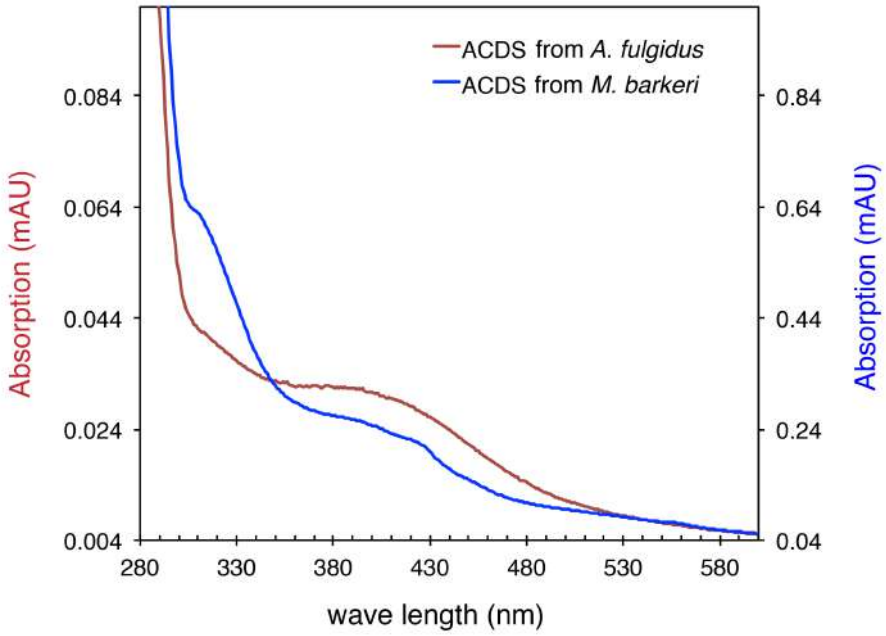

Figure S3. UV-Vis absorption spectra of the purified *Mb*ACDS and *Af*ACDS complexes. Purified *Mb*ACDS (blue line) and *Af*ACDS (red line) complexes were buffered in 50 mM Tris, pH 7.5 and 100 mM NaCl.

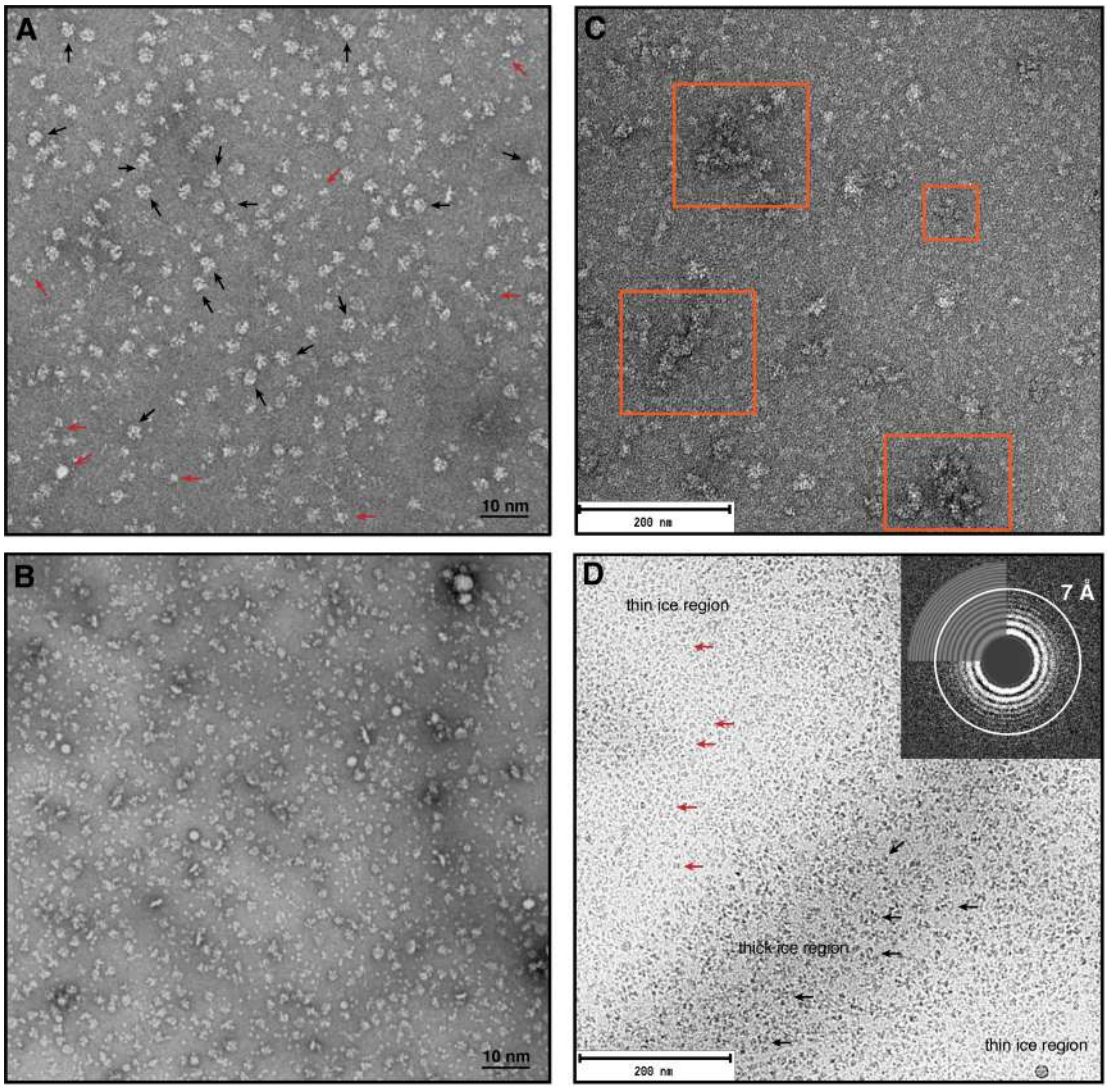

Figure S4. *Af*ACDS complex stability. (A) Protein particles of varying size were observed when freshly purified (never frozen) and stained with 5µL uranyl acetate for 45 sec. (B) Severe decomposition of the ACDS complex was observed when purified protein sample was concentrated in Amicon spin concentrators. (C) Protein aggregates (orange frame) were detected in ca. 20% of all collected data sets independent of the sample preparation. (D) Integer ACDS complex was observed within thick ice region, whereas smaller proteins were accumulated within thin ice regions. NS micrographs are shown in A-C; a representative cryo-electron micrograph is shown in D. Arrows indicate the positions of the protein particles (black for integer ACDS complex; red for the ACDS complex subcomponents).

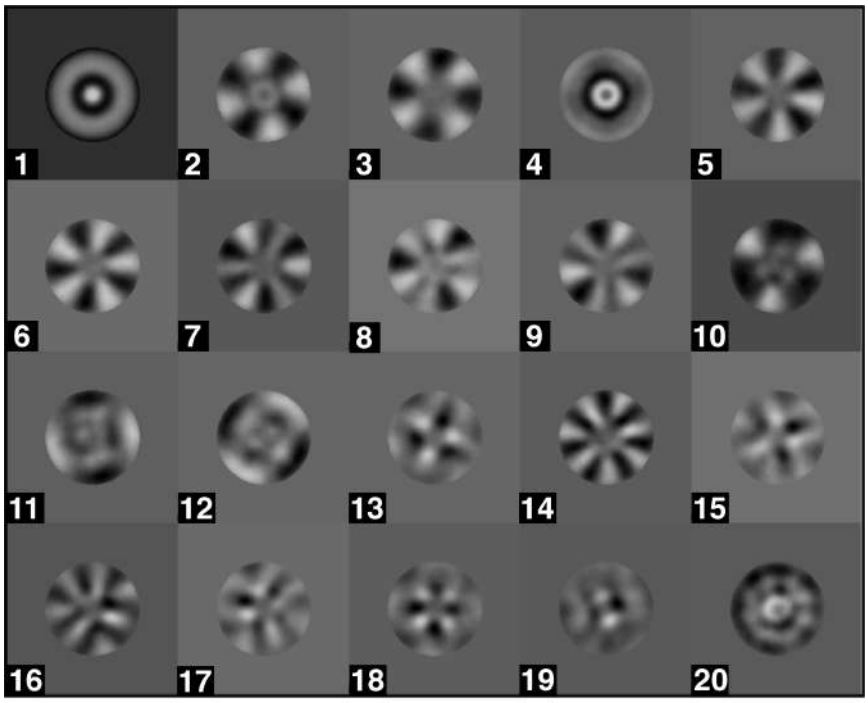

Figure S5. Eigenimages of unaligned negatively stained data set. Eigenimages were generated in IMAGIC with 40 000 unaligned and negatively stained particles. Eigenimage 1 shows the sum of all images. Eigenimages 2-3, 5-6 and 7-10 are indicative of 4-fold, 5-fold and 3-fold symmetries respectively.

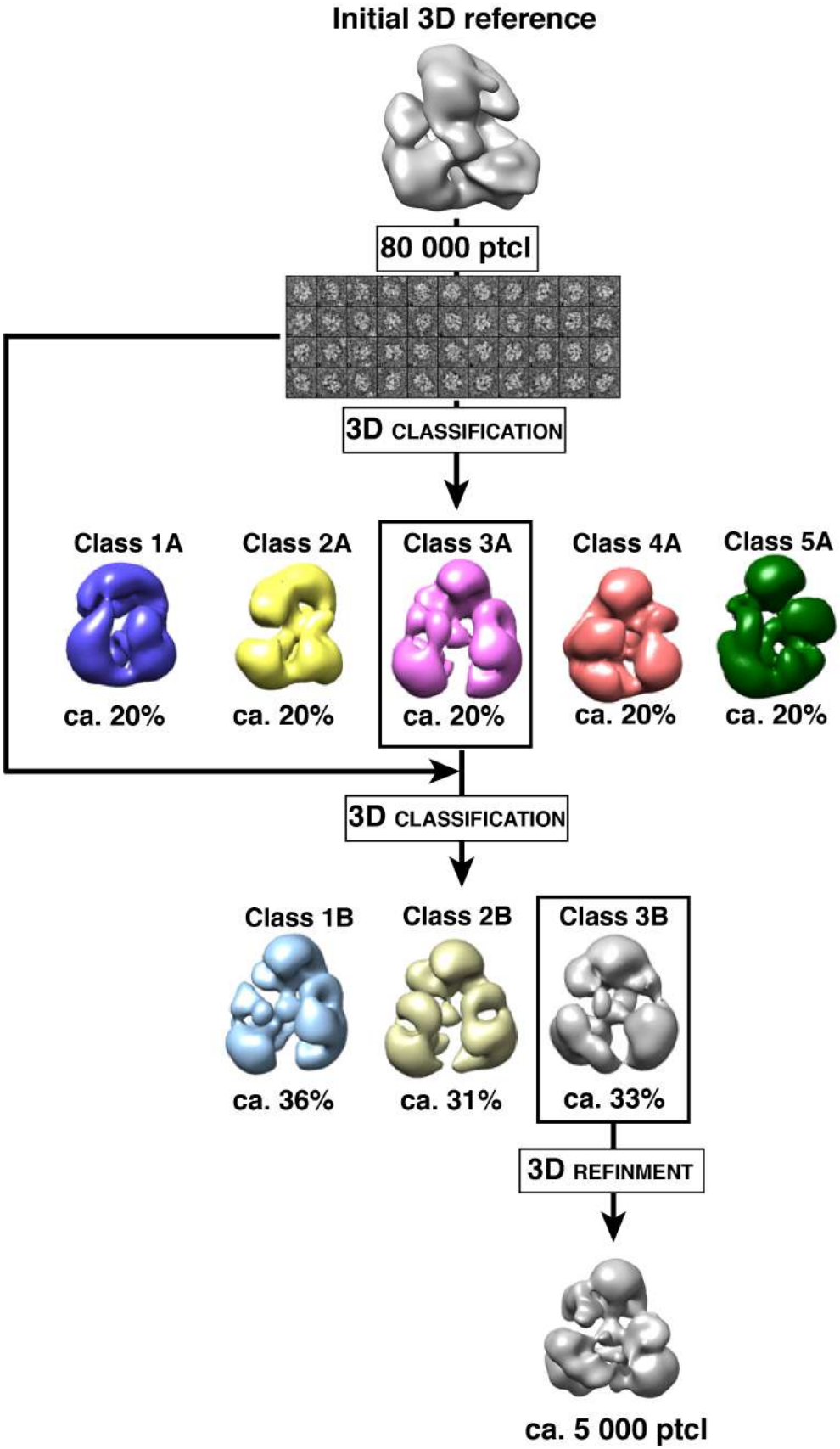

Figure S6. 3D classification of the NS data set in RELION. Detailed description of the data workflow can be found in (3.2.4.2).

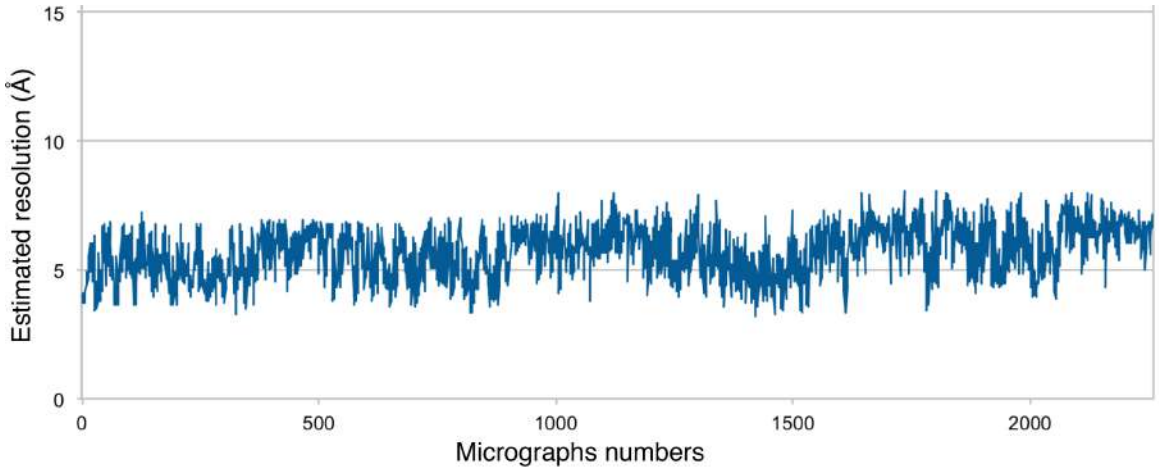

Figure S7. Estimated resolution based on CTF correction.

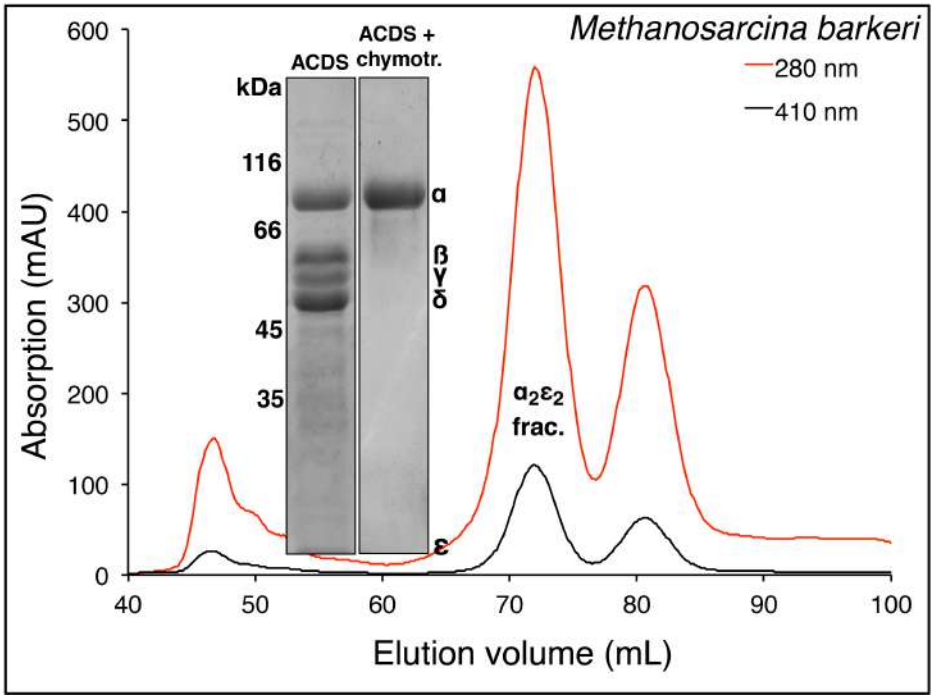

Figure S8. Purification of the *Af*$\alpha_2\varepsilon_2$-subunit. SEC of the α-chymotrypsin digested ACDS-containing sample. The *Mb*$\alpha_2\varepsilon_2$-containing fraction was eluted at 72 mL and was ca. 95% pure. The protein content of the undigested *Mb*ACDS complex and isolated *Mb*$\alpha_2\varepsilon_2$-subunit ($\alpha_2\varepsilon_2$ frac.) were analyzed by 12% SDS-PAGE (inset). Even thought not visualized by SDS-PAGE, the ε-subunit is present in the tryptically digested sample, as observed in crystal structure. The isolated *Mb*$\alpha_2\varepsilon_2$-subunit had a specific CO-oxidation activity of 52 ± 3 U/mg at pH 7.5 using MV as an electron acceptor, which was within range of previously reported activity values for the $\alpha_2\varepsilon_2$-subunit from *M. thermophile* (70 U/mg) (*48*), *M. barkeri* (216 U/mg; 134 U/mg; 75 U/mg) (*17, 47, 53*) and *M. vannielii* (25 U/mg; 190 U/mg) (*49*).

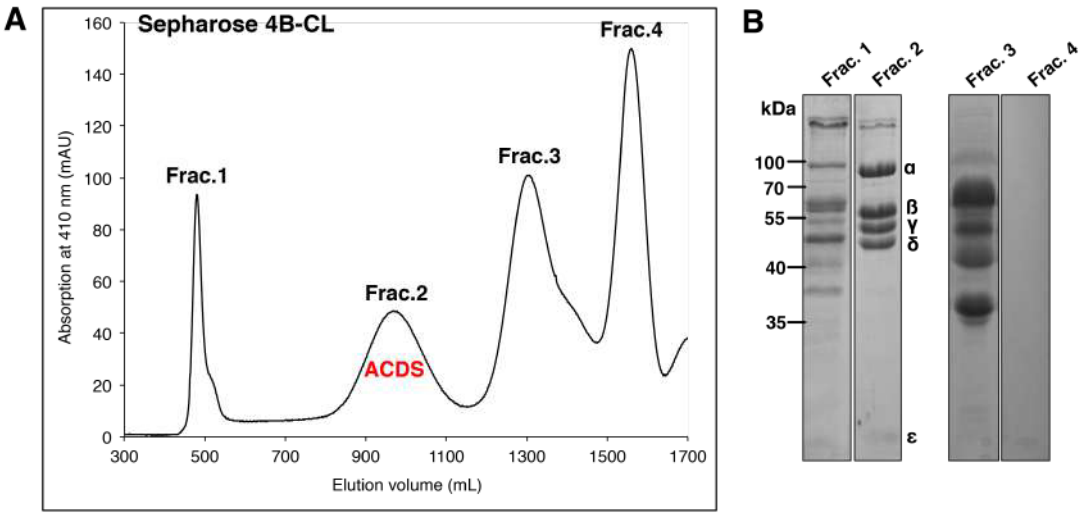

Figure S9. Single-step purification of *Mb*ACDS complex. (A) SEC (solid black line) of the soluble crude cell extract of *M. barkeri* was recorded at 410 nm. The purification protocol was previously described by Grahame *et. al*. (*17*). *Mb*ACDS eluted between 850 and 1100 mL and yielded 20 mg protein per 1 g wet cell paste. (B) SDS-PAGE analysis of each fractions of the SEC. The content of Frac.1 and Frac.4 corresponded to high-molecular-weight aggregates and protein-free cofactors respectively. Frac. 2 contained *Mb*ACDS complex with major bands at 88 kDa, 53 kDa, 51 kDa, 47 kDa and 19 kDa corresponding to α-, ß-, γ-, δ- and ε-subunits respectively. Frac. 3 contained methyl-coenzyme M reductase. The identity of the protein bands was confirmed by PMF analysis.

Figure S10. Sequence alignment between the *cdhA1B1* and *cdhA2B2* operons of *A. fulgidus*. Violet highlighting indicates 100% sequence identity. Based on the observed structural differences between the red-framed amino acids, the sequence from the *cdhA1B1* operon was used for model building into the experimental electron density map at 1.92-Å resolution.

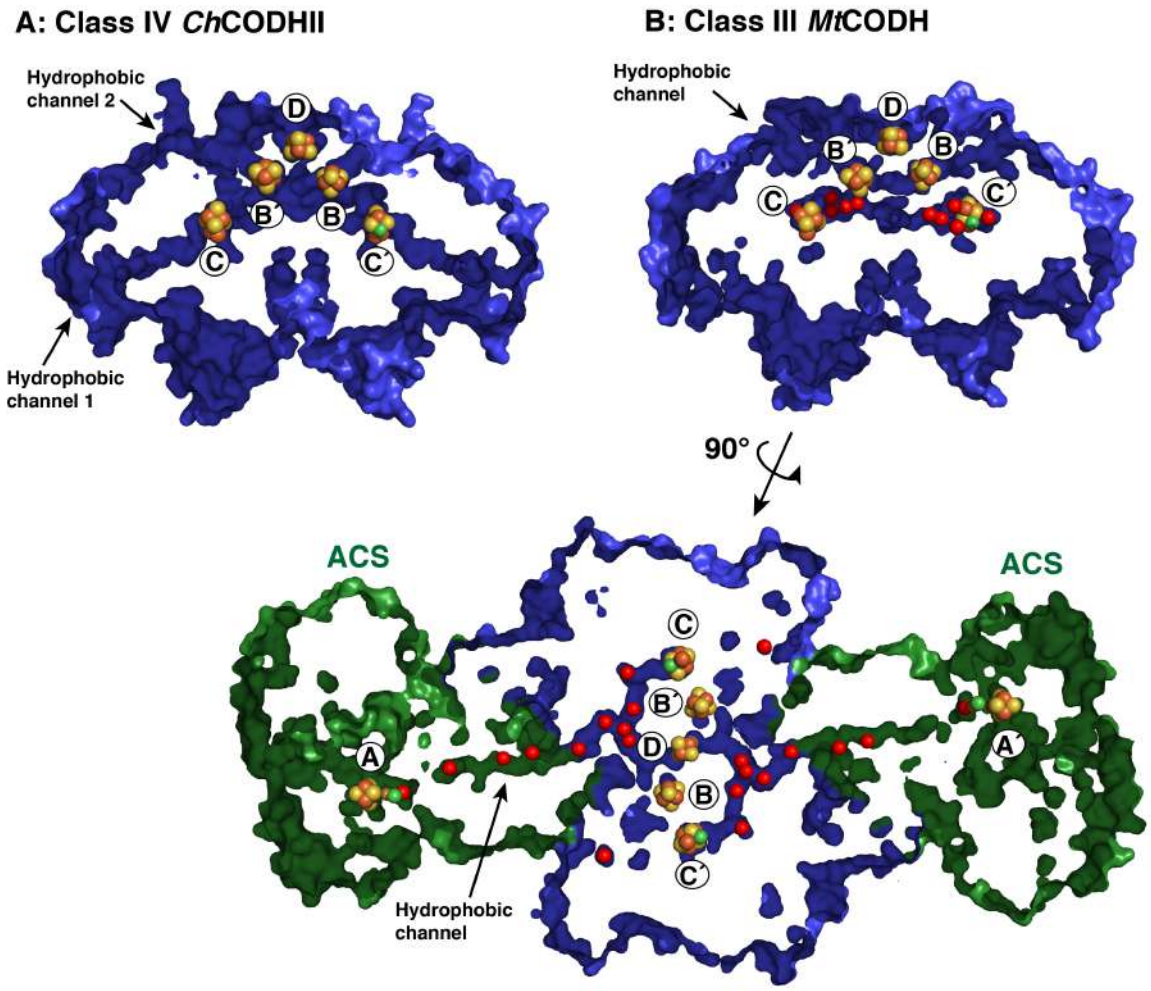

Figure S11. Hydrophobic channels in monofunctional and bifunctional csCODHs. (A) Two hydrophobic channels were observed in *Ch*CODH-II (PDB entry: 2YIV). Hydrophobic channel 1 is unique to the monofunctional csCODHs (*41*). Hydrophobic channel 2 is also observed in bifunctional *Mt*CODH (PDB entry: 1JQK) (B), where the channel is substantially extended to reach the cluster A of ACS (*157*). CODH (blue) and ACS (green) subunits are displayed as surfaces. Metal clusters are represented as spheres (orange for Fe, yellow for S, green for Ni). Xenon molecules are represented as red dots.

A

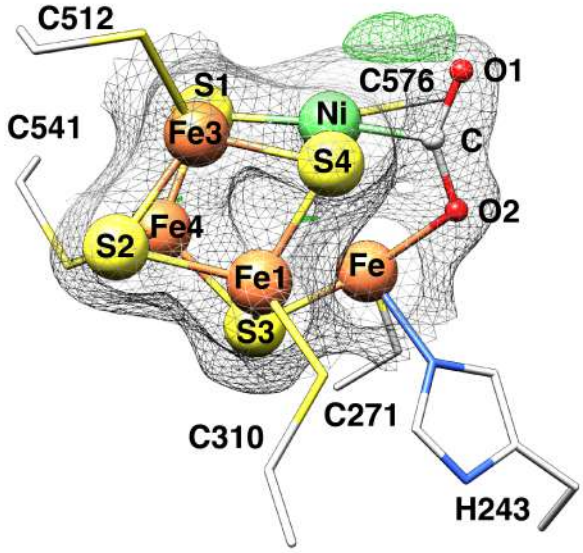

Atom	Occupancy (%)	Temp. factor (Å²)
Fe	0.91	25.16
S3	1.00	24.57
Fe1	1.00	25.83
S2	0.94	23.55
Fe4	0.93	24.65
Fe3	1.00	23.93
S1	1.00	23.13
S4	1.00	24.84
Ni	0.89	25.40
C	0.18	25.10
O1	0.70	26.17
O2	0.75	24.30

B

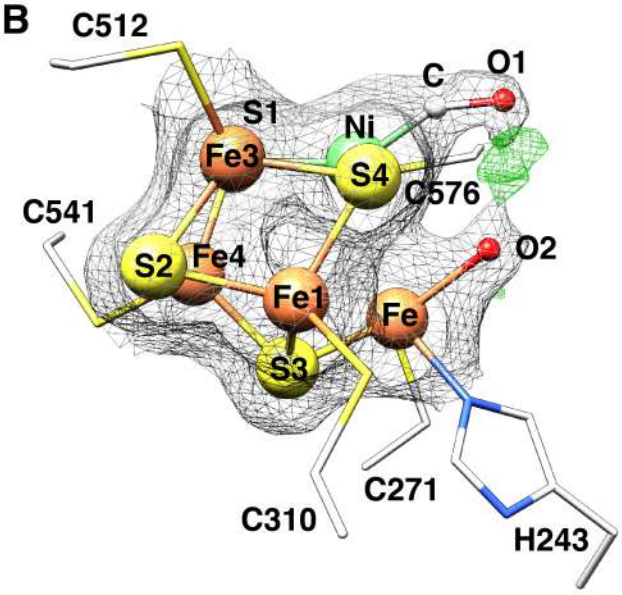

Atom	Occupancy (%)	Temp. factor (Å²)
Fe	0.95	26.14
S3	1.00	24.26
Fe1	1.00	25.87
S2	1.00	24.40
Fe4	0.99	26.14
Fe3	0.96	22.57
S1	1.00	23.02
S4	0.98	24.04
Ni	0.96	27.65
C	0.54	26.04
O1	0.54	25.69
O2	0.86	25.87

Figure S12. Refinements of alternative states of the cluster C in the *Af*$\alpha_2\varepsilon_2$. (A) Occupancies and B-factor values for the CO_2-bound model (Ni-C distance = 1.9 Å; O-C-O angle = 134° and square planar Ni^{2+} coordination upon binding of the η^1-OCO ligand). Remaining positive F_o-F_c electron density (green mesh, 3.1 σ) was observed above Ni atom after full refinement of the cluster C as [Ni4FeS4-CO_2] (gray mesh for 2 F_o-F_c map, 0.5 σ). (B) Occupancies and B-factor values for the formyl bound to Ni atom. A weak positive F_o-F_c electron density (green mesh, 2.7 σ) was observed between the O1 and O2 atoms after full refinement with the [Ni4FeS4-CO-OH_2] model (gray mesh for 2F_o-F_c map, 1.0 σ), which corresponds to the C atom of CO_2 moiety in (A). Metals clusters are shown as spheres (Fe in orange, S in yellow, Ni in green, C in white, O in red). Residues are shown as sticks.

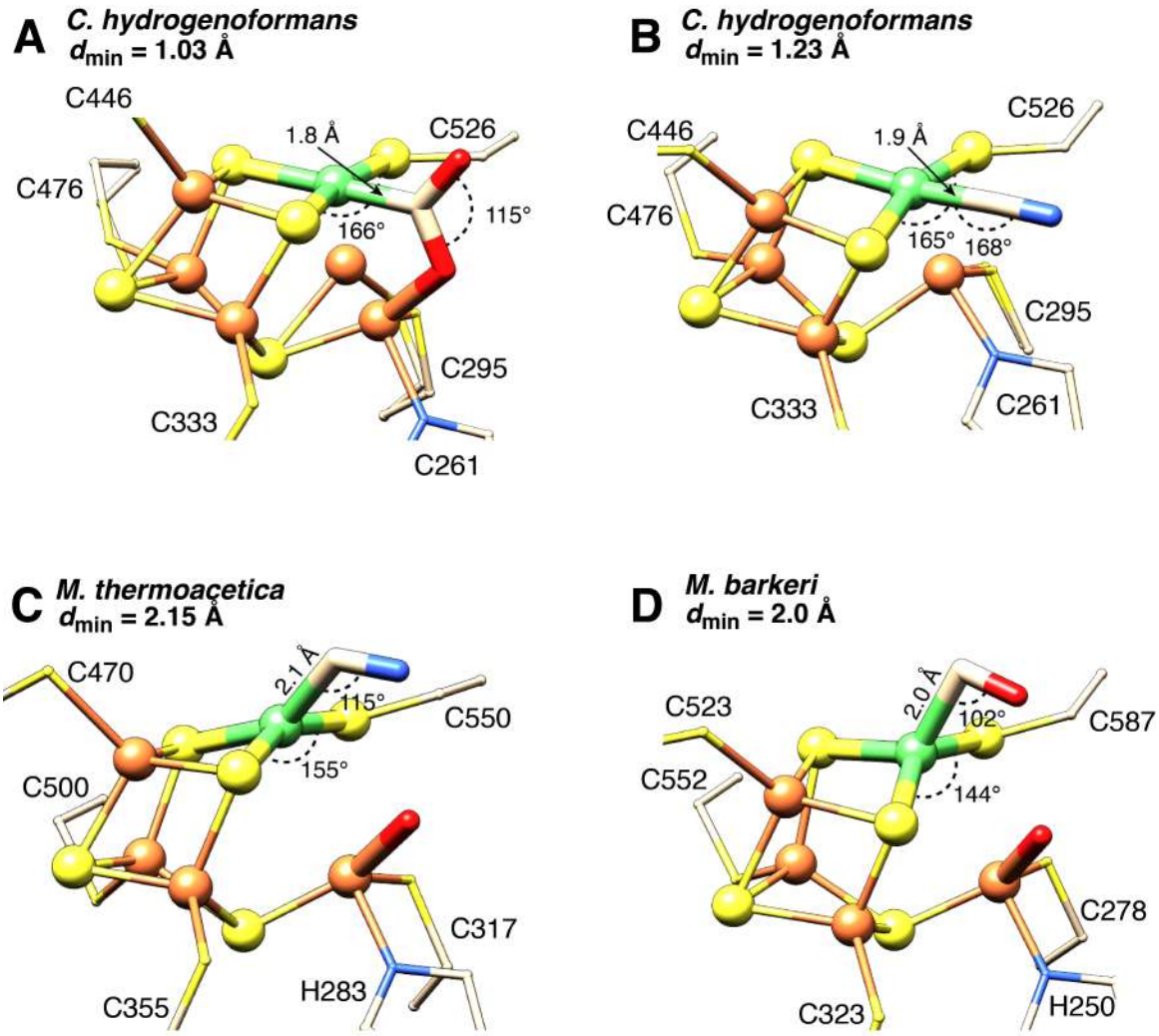

Figure S13. Crystal structures of the active sites of Ni-CODHs with substrates, substrate homologues or unidentified ligands. (A) CO_2-bound *Ch*CODH-II (600 mV) (PDB entry: 4UDX) *(40)*. (B) CN-bound *Ch*CODH-II (320 mV) (PDB entry: 5FLE) *(42)*. (C) Cyanide-bound *Mt*CODH (PDB entry: 3I04) *(21)*. (D) As-isolated *Mb*$\alpha_2\varepsilon_2$-subunit (PDB entry: 3CF4) *(18)*. Metal clusters are shown as spheres (Fe in orange, S in yellow, Ni in green). Coordinating residues are shown as sticks. d_{min} indicates the highest resolution of the X-ray structure.

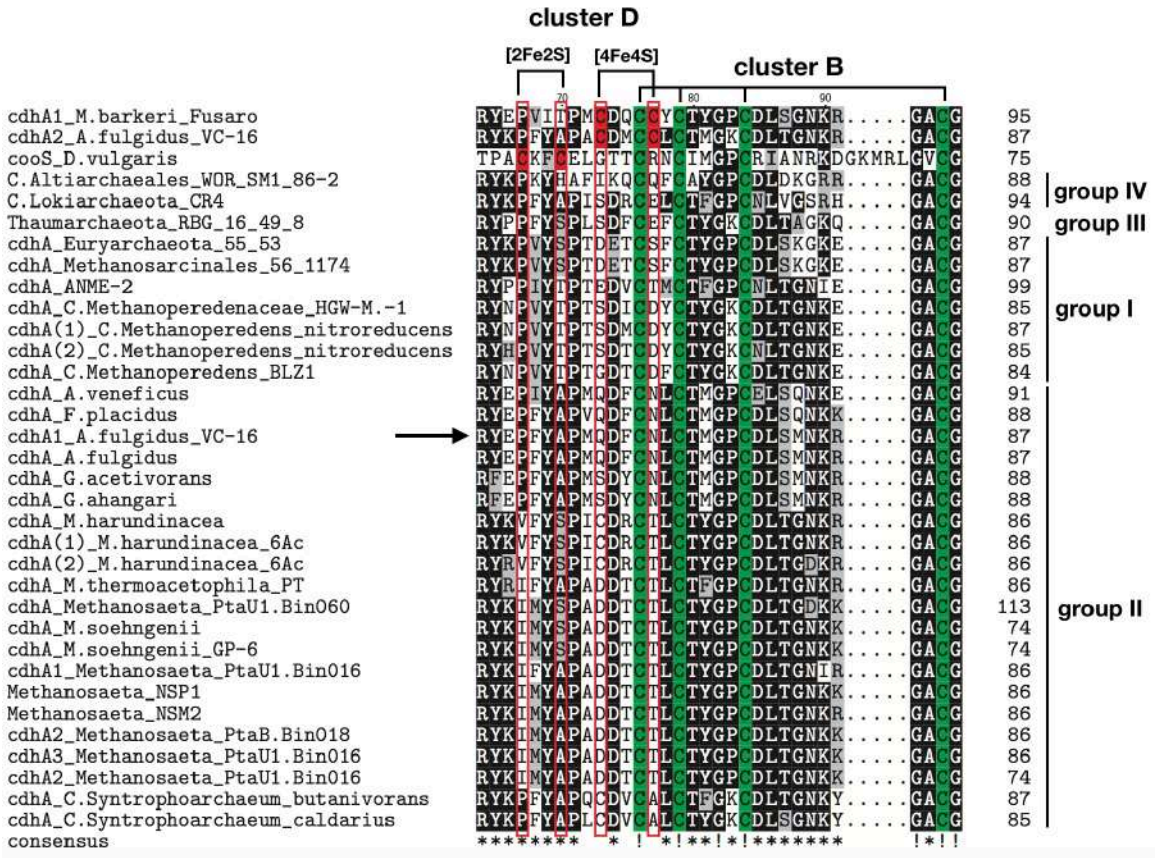

Figure S14. Sequence alignment of the coordinating region of the cluster D depleted cdhCODHs. The positions of the conserved Cys, coordinating the [2Fe2S] or [4Fe4S] bridging cluster, are framed in red. Cluster B coordinating Cys residues are shown in green. Arrow indicates the CdhA1 sequence of the α-subunit in $Af\alpha_2\varepsilon_2$. UniProt entries: Q46G04 (CdhA1 *M. barkeri* str. Fusaro); O30274 (CdhA2 *A. fulgidus* VC-16); Q72A99 (CooS *D. vulgaris*); A0A1D2QXB4 (*C. Altiarchaeales* WOR_SM1_86-2); A0A1Q9MZT4 (*C. Lokiarchaeota* CR4); A0A1G3XU92 (*Thaumarchaeota* RBG_16_49_8); A0A101DW27 (CdhA *Euryarchaeota* 55_53); A0A101F393 (CdhA *Methanosarcinales* 56_1174); A0A2V3JPV2 (CdhA ANME-2); A0A2I0NK21 (*C. Methanoperedenaceae* HGW-M.-1); A0A062V851 (CdhA(1) *C. Methanoperedens nitroreducens*); A0A284VUI8 (CdhA(2) *C. Methanoperedens nitroreducens*); A0A0N8KQA5 (CdhA *C. Methanoperedens* sp. BLZ1); F2KTA1 (CdhA *A. veneficus*); D3RWN8 (CdhA *F. placidus*); O29165 (CdhA1 *A. fulgidus* VC-16); A0A075WD91 (CdhA *A. fulgidus*); A0A0A7GEN2 (CdhA *G. acetivorans*); A0A0F7DBR4 (CdhA *G. ahangari*); E5KJU2 (CdhA M. harundinacea); G7WQP5 (CdhA(1) *M. harundinacea*_6Ac); G7WKX9 (CdhA(2) *M. harundinacea*_6Ac); A0B5W5 (CdhA *M. thermoacetophila*); A0A1V5B3F1 (CdhA *Methanosaeta* sp. PtaU1.Bin060); P26692 (CdhA *M. soehngenii*); F4C0K8 (CdhA *M. soehngenii* GP-6); A0A1V5AQ35 (CdhA1 *Methanosaeta* PtaU1.Bin016); A0A257MIT7 (*Methanosaeta sp*. NSP1); A0A257MUJ3 (*Methanosaeta sp.* NSM2); A0A1V4UPT3 (CdhA2 *Methanosaeta* PtaB.Bin018); A0A1V5AKJ5 (CdhA3 *Methanosaeta* PtaU1.Bin016); A0A1V5APM0 (CdhA2 *Methanosaeta* PtaU1.Bin016); A0A1F2P309 (CdhA *C. Syntrophoarchaeum butanivorans*); A0A1F2P7X1 (CdhA *C. Syntrophoarchaeum caldarius*).

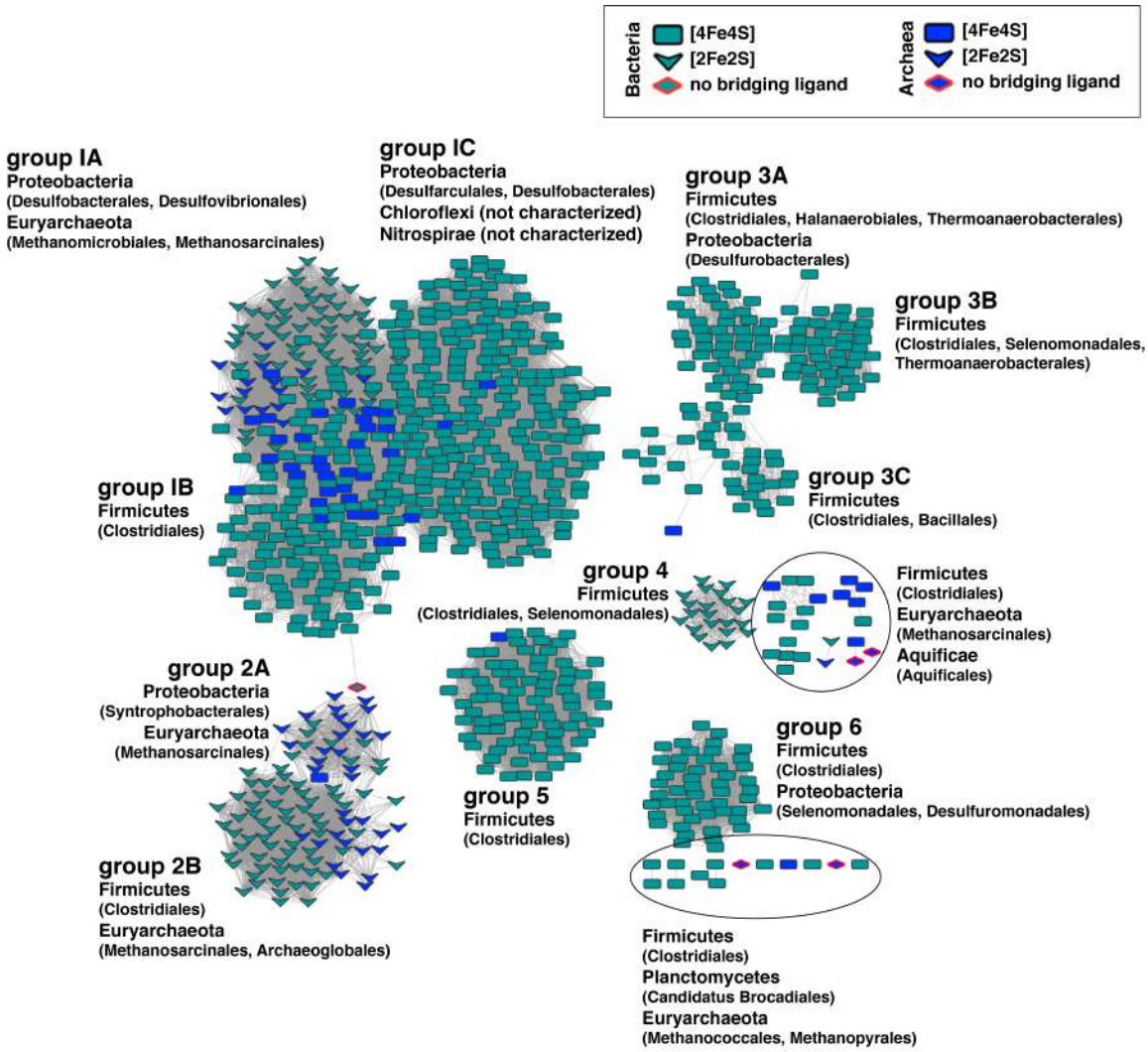

Figure S15. Sequence similarity network of the csCODH family enzymes. The $CooS_{\Delta D}$ sequences are depicted as red-boxed rhombs. The CdhA sequences containing binding motifs for [4Fe4S] or [2Fe2S] clusters in bacteria (green) and archaea (blue) are shown as rectangles and V-shaped elements, respectively. 892 nodes represent 1943 *cooS* sequences (IPR010047) with 31481 pairwise connections. SSN was generated using EFI-EST (*166*) and visualized in Cytoscape (*167*). The alignment score was set to 200. E value was 10^{-5}.

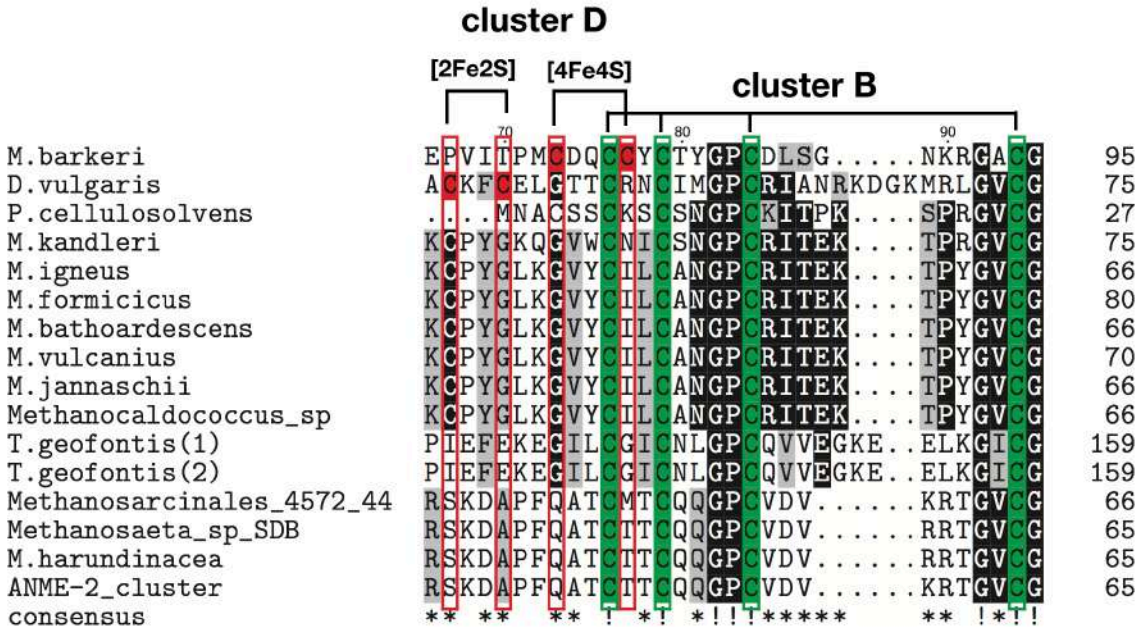

Figure S16. Sequence alignment of the coordinating region of the cluster D depleted csCODHs. The positions of the conserved cysteines, coordinating the [2Fe2S] or [4Fe4S] bridging cluster are framed in red. Cluster B coordinating cysteines are shown in green. UniProt entries: Q46G04 (*M. barkeri*); Q72A99 (CooS from *D. vulgaris*); A0A0L6JKQ4 (CooS from *Pseudobacteroides cellulosolvens*); Q8TXX3 (CooS from *Methanopyrus kandleri*); F6BB28 (CooS from *Methanotorris igneus*); H1L075 (CooS from *Methanotorris formicicus*); A0A076LGK3 (CooS from *Methanocaldococcus bathoardescens*); C9RFY5 (CooS from *Methanocaldococcus vulcanius*); Q58138 (CooS from *Methanocaldococcus jannaschii*); D3S5K4 (CooS from *Methanocaldococcus sp.*); A0A2N7PLW0 (CooS from *Thermodesulfobacterium geofontis* (1)); A0A2N7Q7R0 (CooS from *Thermodesulfobacterium geofontis* (2)); A0A2G1NXG8 (CooS from *Methanosarcinales archaeon* ex4572_44); A0A0Q1AWR1 (CooS from *Methanosaeta* sp. SDB); A0A117LFN7 (CooS from *Methanosaeta harundinacea*); A0A2V3JG14 (CooS from *ANME-2* cluster archaeon).

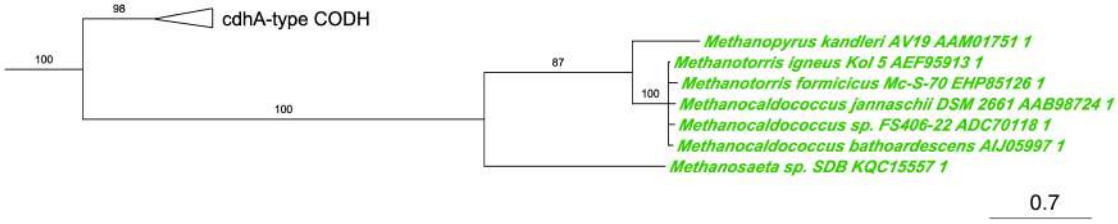

Figure S17. Mapping of $cooS_{\Delta D}$ sequences on the rooted ML phylogenetic tree. Seven $CooS_{\Delta D}$ sequences were mapped on the ML phylogenetic tree of CdhA/CooS homologs (*33*) and are colored in green. Numbers at nodes indicate the bootstrap values (100 replicates). Branches with support below 80 were collapsed. The scale bar represents the average number of substitutions per site. The figure was prepared in TreeGrap2 (*168*). The tree was rooted with *Candidatus Syntrophoarchaeum caldarius* OFV67586 as an out-group (*169*).

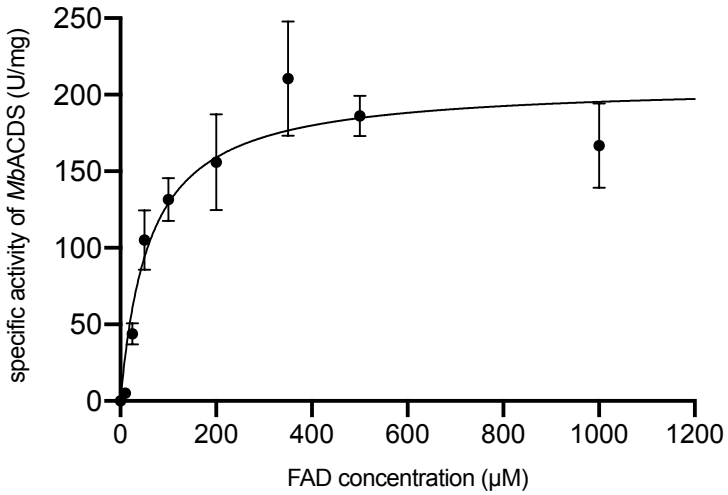

Figure S18. CO-dependent flavin reduction in *Mb*ACDS complex. The activity was measured at 37°C with a concentration range of 0 to 1 mM for FAD. The data was fit to the Michaelis-Menten equation using GraphPad Prism (version 8.0.2 for macOS, GraphPad Software, La Jolla California USA, www.graphpad.com).

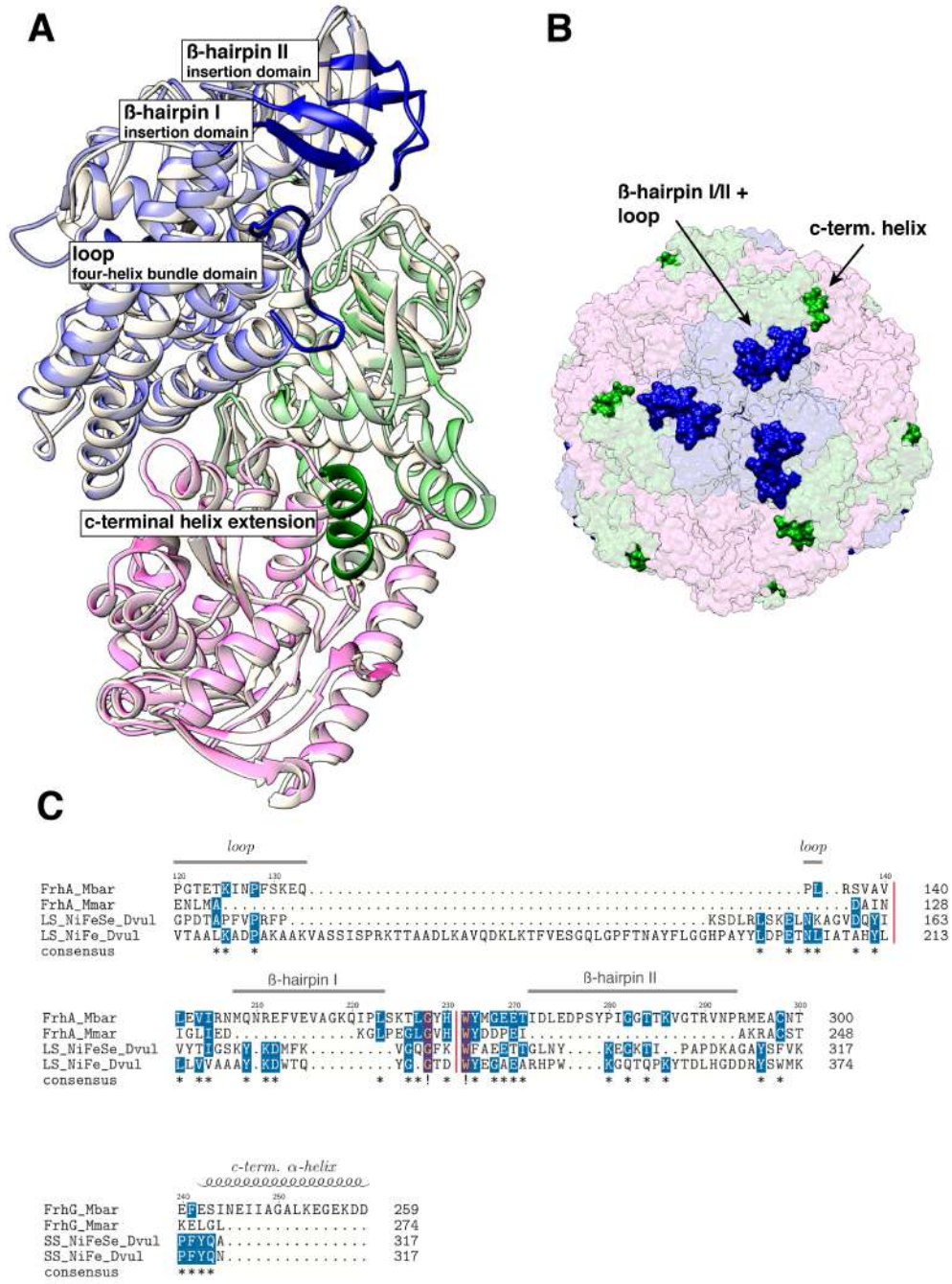

Figure S19. Structural differences between *Mb*FRH and *Mm*FRH. (A) Superposition of the *Mb*FRH and *Mm*FRH protomers. The *Mb*FRH complex is tricolored: FRH-A in navy blue, FRH-B in violet and FRH-G in green. *Mm*FRH is shown in white. Four additional structural elements were found within one *Mb*FRH protomer when compared to its *Mm*FRH homologue: one disordered loop region, two ß-hairpins and a C-terminal α-helix extension. The diverging structural elements between *Mb*FRH and *Mm*FRH dodecamers are depicted as opaque ribbons, while the conserved secondary structure elements are shown with transparency. (B) The structural alternations are located on the surface of the hydrogenase complex and exposed to the cytosol (shown as opaque surface). (C) Sequence alignment of the selected regions corresponding to the alternating structural elements (FrhA/FrhG_Mbar: FRH-A /FRH-G subunits of *Mb*FRH, FrhA/FrhG_Mmar: FRH-A/FRH-G subunits of *Mm*FRH, LS/SS_NiFe_Dvul: large/small subunit of [NiFe] hydrogenase from *D. vulgaris*; LS/SS_NiFeSe_Dvul: large/small subunit of [NiFeSe] hydrogenase from *D. vulgaris*).

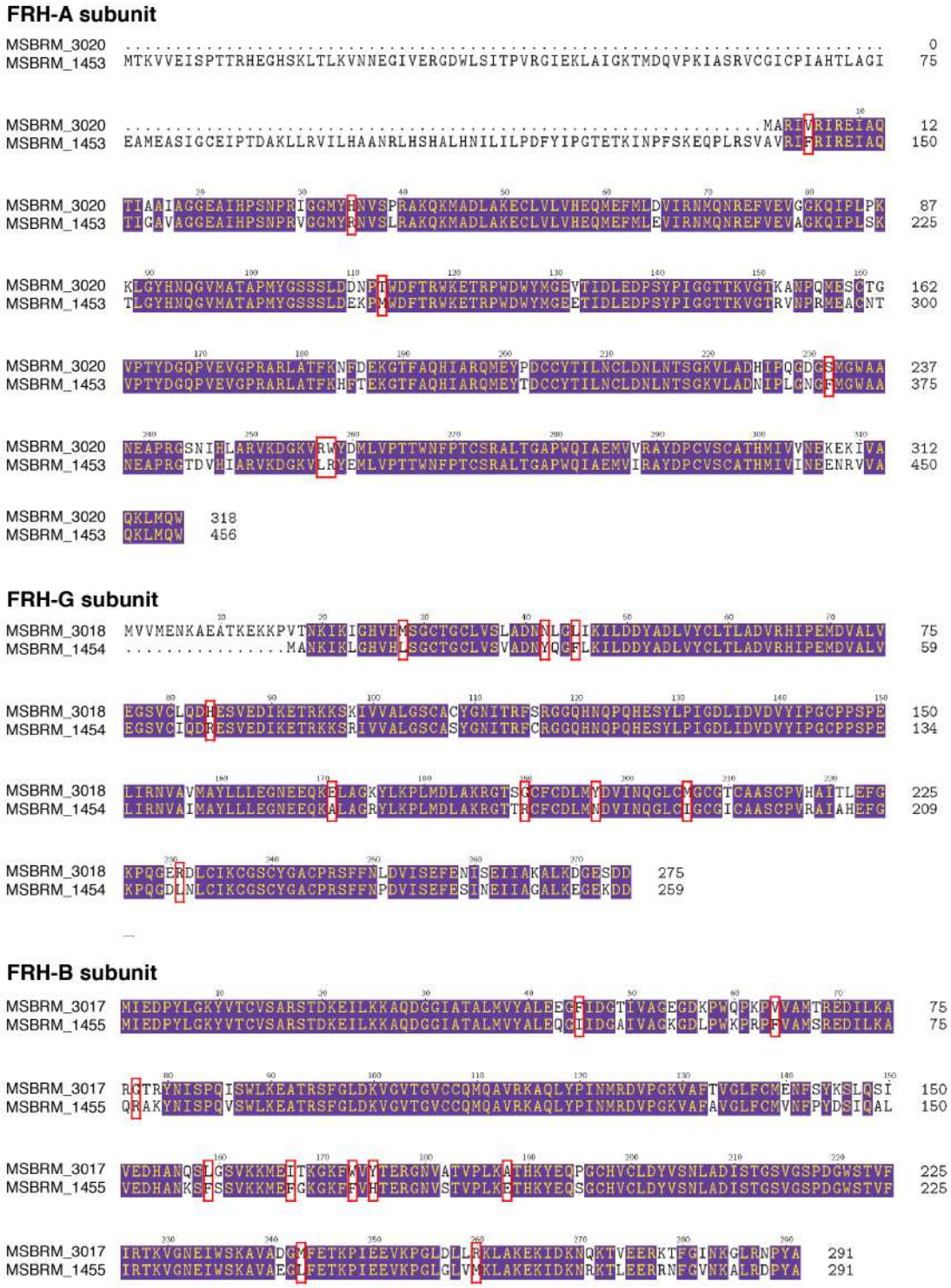

Figure S20. Sequence alignment of three *Mb*FRH-ABG subunits encoded by *frh*ADGB and *fre*AEGB operons of *M. barkeri* MS. Violet highlighting indicates regions of 100% sequence identity between the corresponding FRH subunits. Based on the distinct structural differences of the red framed amino acid side chains, the sequence of the *frh*ADGB operon was fit into the experimental electron density map at a resolution of 1.84 Å.

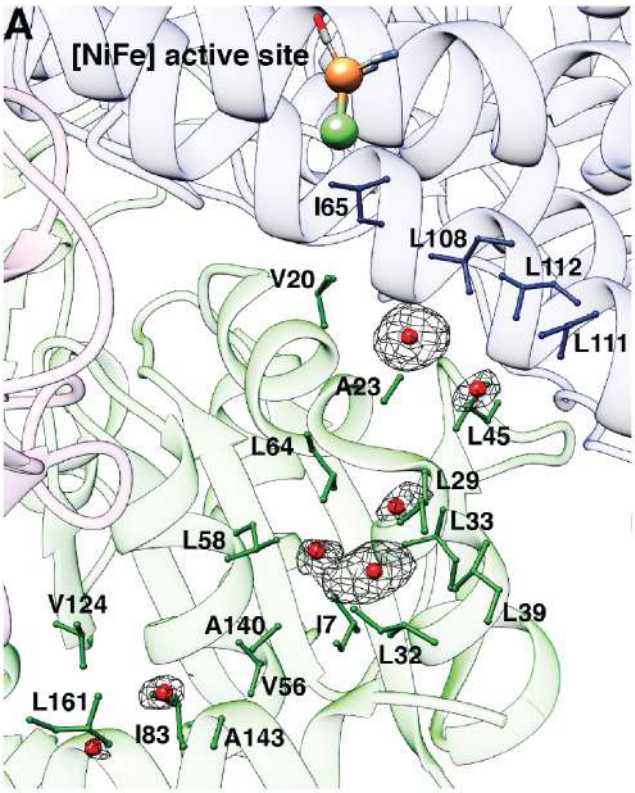

B

	*Mm*FRH	*Mb*FRH
FRH-A	Phe111	Ile111
	Ile108	Leu108
	Leu112	Leu112
	Val65	Ile65
FRH-G	Met62	Val20
	Leu64	Leu22
	Thr65	Ala23
	Leu75	Leu33
	Ile81	Leu39
	Leu87	Leu45
	Ile49	Ile7
	Phe129	Leu87
	Leu74	Ile32
	Leu125	Ile83
	Leu100	Leu58
	Leu98	Val56
	Val182	Ala140
	Leu185	Ala143
	Leu193	Leu161
	Leu166	Val124
	Leu71	Leu29

Figure S21. Detection of the noncanonical hydrophobic channel in *Mb*FRH. (A) Seven Xe atoms (red spheres) were identified within a noncanonical hydrophobic channel in *Mb*FRH. The anomalous difference map for Xe atoms is shown in black mesh at 3.0 σ. (B) Channel lining residues of *Mb*FRH (blue in FRH-A and green in FRH-G) and the corresponding residues in *Mm*FRH.

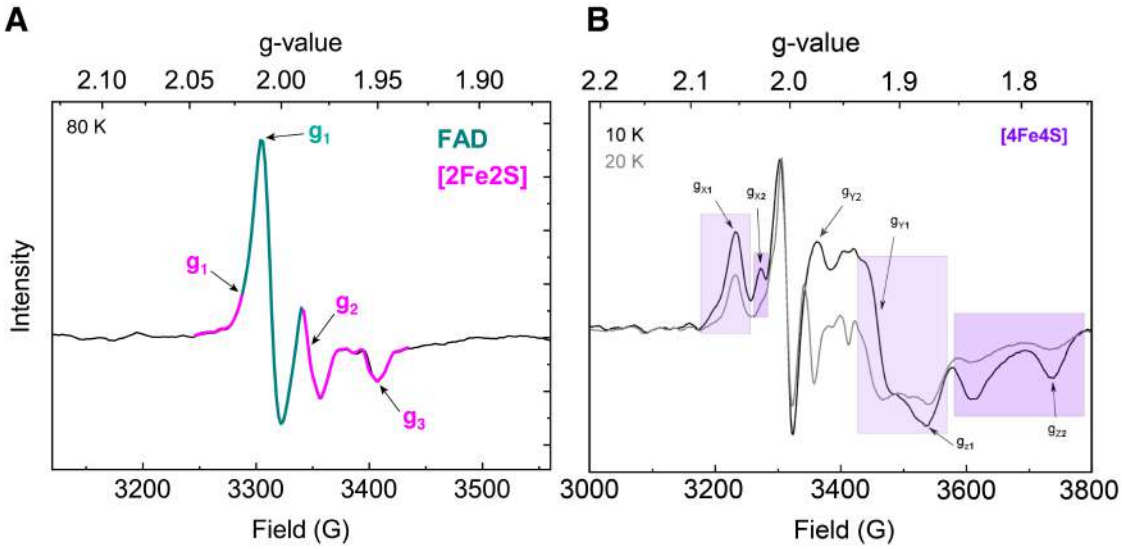

Figure S22. EPR of the FRH-enriched sample. (A) EPR spectra recorded at 80 K. Signals from FAD and a [2Fe2S] cluster are highlighted dark cyan and violet, respectively. (B) EPR spectra recorded at 10 K and 20 K exhibits the typical rhombic signature of at least two different, reduced [4Fe4S] clusters. Corresponding g-values are reported in the Table S3. Spectra were recorded by Christian Lohrent (Institut für Chemie, Technische Universität Berlin). The figure was obtained by courtesy of Christian Lohrent.

A

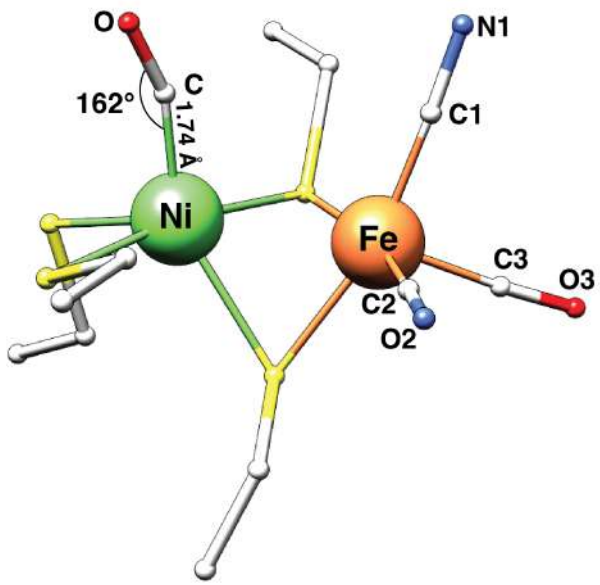

B

Atom	Occupancy (%)	Temp. fact (Å^2)
N2	1.0	33.79
C2	1.0	31.78
FE	1.0	33.25
C3	0.95	37.61
O3	0.9	35.06
C1	0.98	31.13
N1	1.0	31.68
NI	1.0	37.44
C	0.52	36.01
O	0.49	36.47

Figure S23. Refinement of the [NiFe] active site after CO inhibition. (A) CO interacts with the catalytically active Ni_a-S state and binds terminally to the Ni atom at a Ni-C-O angle of 162°. The Ni-C distance is 1.74 Å. Amino acids and metals are depicted as sticks and spheres, respectively. (B) The CO ligand was refined to approx. 50% occupancy. Chemical restraint parameters for the CO-[NiFe] complex were generated by iterative cycles of refinement based on the homologous models of CO-inhibited [NiFe] hydrogenase from *D. vulgaris* Miyazaki F (*103*).

Table S1. Diffraction and refinement statistics for the *Af*$\alpha_2\varepsilon_2$-subunit.

Data collection			
Wavelength (Å)	0.9184		
Resolution range (Å)	50 - 1.92 (1.92 – 2.04)[1]		
Space group	*C*2		
Cell dimensions α, b, c (Å) α, ß ,γ (°)	99.43, 109.00, 94.973 90.00, 119.06, 90.00		
Completeness (%)	98 (96)[1]		
Observed/unique reflections	275883 / 65601 (43142 / 10369)[1]		
$R_{obs.}$ (%)	18.5 (122.4)[1]		
$R_{meas.}$ (%)	21.3 (140.5)[1]		
I / σI	6.10 (1.10)[1]		
CC (1/2)	99.2 (42.0)[1]		
Refinements			
	[Ni4Fe4S]	[Ni4Fe4S-CO_2]	[Ni4Fe4S-CO/OH_2]
R_{work} / R_{free} (%)	0.172 / 0.209	0.169 / 0.205	0.169 / 0.206
Molecules in ASU	2	2	2
Ramachandran statistics (%) preferred / allowed / disallowed	96.62 / 2.59 / 0.79	96.63 / 2.47 / 0.90	96.52 / 2.58 / 0.90
RMS deviation from ideal geometry Bond lengths (Å) Bond angles (°) ESU[2] (Å)	 0.008 1.783 0.149	 0.008 1.813 0.145	 0.008 1.808 0.145

[1] Values in bracket are from the highest resolution shell.

[2] Calculations based on maximum likelihood in Refmac5

Table S2. Diffraction and refinement statistics for *Mb*FRH crystals in the as-isolated state.

	"as-isolated" (native)	"as-isolated" (Fe set)
Data collection		
Wavelength (Å)	0.918	1.732
Resolution range (Å)	50 - 1.84 (1.95 - 1.84)[1]	50 - 2.06 (2.18 - 2.06)[1]
Space group	*F*23	*F*23
Cell dimensions a=b=c (Å) α=ß=γ (°)	 235.83 90	 236.33 90
Completeness (%)	99.6 (99.3)[1]	99.5 (97.8)[1]
Observed/unique reflections	744324 / 183316 (114544 / 29569)[1]	643642 / 131296 (83050 / 20763)[1]
$R_{obs.}$ (%)	18.3 (211.5)[1]	10 (176.7)[1]
$R_{meas.}$ (%)	21.1 (243.9)[1]	11.2 (201.9)[1]
I / σI	6.62 (0.58)[1]	10.51 (0.63)[1]
CC (1/2)	99.3 (20.9)[1]	99.7 (26.7)[1]
Refinement		
R_{work} / R_{free} (%)	0.1753 / 0.2206	0.1935 / 0.2266
Molecules in ASU	1	1
Ramachandran statistics (%) preferred /allowed /disallowed	97.13 / 2.67 / 0.21	96.1 / 3.1 / 0.8
RMS deviation from ideal geometry Bond lengths (Å) Bond angles (°) ESU[2] (Å)	 0.017 1.337 0.14	 0.019 1.859 0.21

[1] Values in bracket are from the highest resolution shell.

[2] Calculations based on maximum likelihood in Refmac5.

Table S3. Diffraction and refinement statistics for derivatized *Mb*FRH crystals.

	Xe and S set	CO	H_2/MV
Data collection			
Wavelength (Å)	1.900	0.918	0.981
Resolution range (Å)	50 - 2.28 (2.42 - 2.28)[1]	50 – 1.99 (2.11 – 1.99)[1]	50 – 1.94 (2.06 – 1.99)[1]
Space group	*F*23	*F*23	*F*23
Cell dimensions a=b=c (Å) α=ß=γ (°)	236.82 90	235.43 90	235.23 90
Completeness (%)	99.8 (99.9)[1]	99.9 (99.3)[1]	100 (99.9)[1]
Observed/unique reflections	1978852 / 97909 (300327 / 15842)[1]	1512394 / 73859 (236179 / 11826)[1]	909535 / 79347 (146868/12745)[1]
$R_{obs.}$ (%)	9.0 (149.4)[1]	23.0 (256.5)[1]	21.3 (174.3)[1]
$R_{meas.}$ (%)	9.3 (153.5)[1]	23.6 (263.2)[1]	22.3 (182.4)[1]
I / σI	23.32 (1.76)[1]	12.73 (1.22)[1]	9.59 (1.34)[1]
CC (1/2)	99.9 (76.3)[1]	99.8 (53.9)[1]	99.7 (54.2)[1]
Refinement			
R_{work} / R_{free} (%)	0.1760 / 0.2270	0.1688 / 0.2092	0.1768 / 0.2187
Molecules in ASU	1	1	1
Ramachandran statistics (%) preferred/allowed/disallowed	95.08 / 4.72 / 0.21	97.02 / 2.87 / 0.1	96.01/ 3.76 /0.23
RMS deviation from ideal geometry Bond lengths (Å) Bond angles (°) ESU[2] (Å)	 0.011 1.143 0.231	 0.013 1.169 0.145	 0.013 1.350 0.125

[1] Values in bracket are from the highest resolution shell.

[2] Calculations based on maximum likelihood in Refmac5.

Table S4. g-Values of paramagnetic *Mb*FRH cofactors derived by EPR spectroscopy. The measurements were conducted by Christian Lohrent (Institut für Chemie, Technische Universität Berlin). The table was obtained by courtesy of Christian Lohrent.

Cofactor	$g_{x/1}$	$g_{y/2}$	$g_{z/3}$
[4Fe4S]	2.054	1.921	1.877
[4Fe4S]	2.029	1.907	1.776
[2Fe2S]	2.016	1.982	1.946
FAD	2.003		

Table S5. Identities of the mononuclear metal ion found in the proximity of the [NiFe] active site. Hydrogenase crystal structures with a single Fe ion are highlighted in red.

Organism	Class	PDB entry code	Resolution (Å)	Metal
Desulfovibrio gigas	[NiFe]	2FRV	2.54	Mg^{2+}
		1YQ9	2.35	Mg^{2+}
Desulfovibrio fructosivorans		1FRF, 1YRQ	2.7, 2.1	Mg^{2+}
		1YQW	1.83	Fe^{2+} (?)[1]
		3CUS	2.2	Mg^{2+}
		3H3X	2.7	Mg^{2+}
		4UPE, 4UPV, 4UQL, 4UQP, 4URH	1.8, 1.5, 1.2, 1.4, 1.4	Mg^{2+}
		4UE2	2.0	Mg^{2+}
		4UCX, 4UCQ, 4UCW	2.0, 2.6, 2.3	Mg^{2+}
Desulfovibrio vulgaris Miyazaka F		1H2A	1.8	Mg^{2+}
		1H2R	1.4	Mg^{2+}
		1UBH, 1UBJ, 1UBK, 1UBL, 1UBM, 1UBO, 1UBR, 1UBT, 1UBU	1.4, 1.4, 1.2, 1.2, 1.4, 1.4, 1.3, 1.3, 1.4	Mg^{2+}
		1WUH	1.2	Mg^{2+}
		1WUI, 1WUJ, 1WUK, 1WUL	1, 1.4, 1.1, 1.5	Mg^{2+}
		4U9H, 4U9I	0.9, 1.0	Mg^{2+}
Escherichia coli		5A4I, 4UE3, 5A4F, 5A4M, 5ADU	1.2, 1.4, 1.3, 1.7, 1.1	Mg^{2+}
		5LRY	1.4	Mg^{2+}
		3USE, 3UQY, 3USC	1.7, 1.5, 2.0	Mg^{2+}
		4GD3	3.3	Mg^{2+}
Desulfovibrio desulfuricans ATCC 27774		1E3D	1.8	Mg^{2+}
Allochromatium vinosum		3MYR	2.1	Mg^{2+}
Salmonella typhimurium		4C3O	3.2	Mg^{2+}
Methanothermococcus thermolithotrophicus		5ODC, 5ODH, 5ODI, 5ODQ, 5ODR	2.3, 2.2, 2.4, 2.2, 2.2	Ca^{2+}/ Fe^{3+}
Hydrogenophilus thermoluteolus		5XF9, 5XFA	2.6, 2.7	Mg^{2+}
Hydrogenovibrio marinus		3AYX, 5Y34, 3AYZ	1.2, 1.3, 1.2	Mg^{2+}
Cupriavidus necator		4IUB, 4IUC, 4IUD	1.6, 1.5, 1.5	Mg^{2+}
		3RGW	1.5	Mg^{2+}
		5D51	1.5	Mg^{2+}
Methanothermobacter marburgensis		4OMF	1.7	Mg^{2+}
		4CI0	3.4	Fe^{2+} (?)[1]
		3ZFS	4.0	Fe^{2+} (?)[1]
Desulfomicrobium baculatum	[NiFeSe]	1CC1	2.2	Fe^{2+}
		4KL8, 4KN9, 4KO1, 4KO2, 4KO3, 4KO4	1.5, 1.4, 1.6, 1.6, 1.7, 2.0	Ca^{+}
Desulfovibrio vulgaris Hildenborough		2WPN	2.0	Fe^{2+}
		3ZE6, 3ZE7, 3ZE8, 3ZE9, 3ZEA	1.5, 2.0, 1.8, 1.3, 1.8	Fe^{2+}
		5JT1, 5JSH, 5JSK, 5JSU, 5JSY	1.4, 1.3, 1.0, 1.4, 1.0	Fe^{2+}
Clostridium pasteurianum	[FeFe]	1HEF	1.6	n.d.
		5LA3	2.3	n.d.
		1FEH	1.8	n.d.
		3C8Y	1.4	n.d.
		4XDC	1.6	n.d.
		5BYQ	1.7	n.d.
Methanocaldococcus jannaschii		3DAG, 3DAF	1.8, 1.8	n.d.
	[Fe]	4YT4, 4YT2, 4YT5, 4YT8	2.2, 1.7, 1.9, 1.9	n.d.

[1] The question mark indicates the structures in which the Fe positions were not confirmed by an orthogonal method, e.g. by anomalous scattering.

5 REFERENCES

1. R. J. Williams, Systems biology of evolution: the involvement of metal ions. *Biometals* **20**, 107-112 (2007).

2. I. Yruela, Transition metals in plant photosynthesis. *Metallomics* **5**, 1090-1109 (2013).

3. A. M. Appel *et al.*, Frontiers, opportunities, and challenges in biochemical and chemical catalysis of CO_2 fixation. *Chem Rev* **113**, 6621-6658 (2013).

4. N. Cox, D. A. Pantazis, F. Neese, W. Lubitz, Biological water oxidation. *Acc Chem Res* **46**, 1588-1596 (2013).

5. G. T. Babcock, How oxygen is activated and reduced in respiration. *Proc Natl Acad Sci U S A* **96**, 12971-12973 (1999).

6. B. Meunier, S. P. de Visser, S. Shaik, Mechanism of oxidation reactions catalyzed by cytochrome p450 enzymes. *Chem Rev* **104**, 3947-3980 (2004).

7. B. M. Hoffman, D. Lukoyanov, Z. Y. Yang, D. R. Dean, L. C. Seefeldt, Mechanism of nitrogen fixation by nitrogenase: the next stage. *Chem Rev* **114**, 4041-4062 (2014).

8. W. Lubitz, H. Ogata, O. Rudiger, E. Reijerse, Hydrogenases. *Chem Rev* **114**, 4081-4148 (2014).

9. G. W. Bartholomew, M. Alexander, Microbial metabolism of carbon monoxide in culture and in soil. *Appl Environ Microbiol* **37**, 932-937 (1979).

10. H. Dobbek, L. Gremer, R. Kiefersauer, R. Huber, O. Meyer, Catalysis at a dinuclear [CuSMo(==O)OH] cluster in a CO dehydrogenase resolved at 1.1-Å resolution. *Proc Natl Acad Sci U S A* **99**, 15971-15976 (2002).

11. D. A. Grahame, E. DeMoll, Substrate and accessory protein requirements and thermodynamics of acetyl-CoA synthesis and cleavage in *Methanosarcina barkeri*. *Biochemistry* **34**, 4617-4624 (1995).

12. G. M. King, C. F. Weber, Distribution, diversity and ecology of aerobic CO-oxidizing bacteria. *Nat Rev Microbiol* **5**, 107-118 (2007).

13. J. G. Ferry, CO dehydrogenase. *Annu Rev Microbiol* **49**, 305-333 (1995).

14. S. M. Techtmann *et al.*, Evidence for horizontal gene transfer of anaerobic carbon monoxide dehydrogenases. *Front Microbiol* **3**, 132 (2012).

15. P. A. Lindahl, B. Chang, The evolution of acetyl-CoA synthase. *Orig Life Evol Biosph* **31**, 403-434 (2001).

16. D. A. Grahame, S. Gencic, E. DeMoll, A single operon-encoded form of the acetyl-CoA decarbonylase/synthase multienzyme complex responsible for synthesis and cleavage of acetyl-CoA in *Methanosarcina thermophila*. *Arch Microbiol* **184**, 32-40 (2005).

17. D. A. Grahame, Catalysis of acetyl-CoA cleavage and tetrahydrosarcinapterin methylation by a carbon monoxide dehydrogenase-corrinoid enzyme complex. *J Biol Chem* **266**, 22227-22233 (1991).

18. W. Gong *et al.*, Structure of the $alpha_2epsilon_2$ Ni-dependent CO dehydrogenase component of the *Methanosarcina barkeri* acetyl-CoA decarbonylase/synthase complex. *Proc Natl Acad Sci U S A* **105**, 9558-9563 (2008).

19. D. A. Grahame, E. DeMoll, Partial reactions catalyzed by protein components of the acetyl-CoA decarbonylase synthase enzyme complex from *Methanosarcina barkeri*. *J Biol Chem* **271**, 8352-8358 (1996).

20. T. I. Doukov, T. M. Iverson, J. Seravalli, S. W. Ragsdale, C. L. Drennan, A Ni-Fe-Cu center in a bifunctional carbon monoxide dehydrogenase/acetyl-CoA synthase. *Science* **298**, 567-572 (2002).

21. Y. Kung *et al.*, Visualizing molecular juggling within a B_{12}-dependent methyltransferase complex. *Nature* **484**, 265-269 (2012).

22. H. Dobbek, V. Svetlitchnyi, L. Gremer, R. Huber, O. Meyer, Crystal structure of a carbon monoxide dehydrogenase reveals a [Ni-4Fe-5S] cluster. *Science* **293**, 1281-1285 (2001).

23. C. L. Drennan, J. Heo, M. D. Sintchak, E. Schreiter, P. W. Ludden, Life on carbon monoxide: X-ray structure of *Rhodospirillum rubrum* Ni-Fe-S carbon monoxide dehydrogenase. *Proc Natl Acad Sci U S A* **98**, 11973-11978 (2001).

24. S. W. Singer, M. B. Hirst, P. W. Ludden, CO-dependent H_2 evolution by *Rhodospirillum rubrum*: role of CODH:CooF complex. *Biochim Biophys Acta* **1757**, 1582-1591 (2006).

25. B. Soboh, D. Linder, R. Hedderich, Purification and catalytic properties of a CO-oxidizing:H_2-evolving enzyme complex from *Carboxydothermus hydrogenoformans*. *Eur J Biochem* **269**, 5712-5721 (2002).

26. D. Chivian *et al.*, Environmental genomics reveals a single-species ecosystem deep within Earth. *Science* **322**, 275-278 (2008).

27. M. Rother, E. Oelgeschlager, W. M. Metcalf, Genetic and proteomic analyses of CO utilization by *Methanosarcina acetivorans*. *Arch Microbiol* **188**, 463-472 (2007).

28. N. Matschiavelli, E. Oelgeschlager, B. Cocchiararo, J. Finke, M. Rother, Function and regulation of isoforms of carbon monoxide dehydrogenase/acetyl coenzyme A synthase in *Methanosarcina acetivorans*. *J Bacteriol* **194**, 5377-5387 (2012).

29. U. Deppenmeier *et al.*, The genome of *Methanosarcina mazei*: evidence for lateral gene transfer between bacteria and archaea. *J Mol Microbiol Biotechnol* **4**, 453-461 (2002).

30. D. L. Maeder *et al.*, The *Methanosarcina barkeri* genome: comparative analysis with *Methanosarcina acetivorans* and *Methanosarcina mazei* reveals extensive rearrangement within methanosarcinal genomes. *J Bacteriol* **188**, 7922-7931 (2006).

31. R. I. Eggen *et al.*, Carbon monoxide dehydrogenase from *Methanosarcina frisia* Go1. Characterization of the enzyme and the regulated expression of two operon-like cdh gene clusters. *J Biol Chem* **271**, 14256-14263 (1996).

32. K. R. Sowers, T. T. Thai, R. P. Gunsalus, Transcriptional regulation of the carbon monoxide dehydrogenase gene (*cdhA*) in *Methanosarcina thermophila*. *J Biol Chem* **268**, 23172-23178 (1993).

33. P. S. Adam, G. Borrel, S. Gribaldo, Evolutionary history of carbon monoxide dehydrogenase/acetyl-CoA synthase, one of the oldest enzymatic complexes. *Proc Natl Acad Sci U S A* **115**, E1166-E1173 (2018).

34. F. L. Sousa, W. F. Martin, Biochemical fossils of the ancient transition from geoenergetics to bioenergetics in prokaryotic one carbon compound metabolism. *Biochim Biophys Acta* **1837**, 964-981 (2014).

35. E. C. Wittenborn *et al.*, Redox-dependent rearrangements of the NiFeS cluster of carbon monoxide dehydrogenase. *Elife* **7**, (2018).

36. J. H. Jeoung, B. M. Martins, H. Dobbek, Carbon Monoxide Dehydrogenases. *Methods Mol Biol* **1876**, 37-54 (2019).

37. S. Gencic, D. A. Grahame, Nickel in subunit beta of the acetyl-CoA decarbonylase/synthase multienzyme complex in methanogens. Catalytic properties and evidence for a binuclear Ni-Ni site. *J Biol Chem* **278**, 6101-6110 (2003).

38. Y. A. Muller, G. E. Schulz, Structure of the thiamine- and flavin-dependent enzyme pyruvate oxidase. *Science* **259**, 965-967 (1993).

39. J. H. Jeoung, H. Dobbek, Carbon dioxide activation at the Ni,Fe-cluster of anaerobic carbon monoxide dehydrogenase. *Science* **318**, 1461-1464 (2007).

40. J. Fesseler, J. H. Jeoung, H. Dobbek, How the [NiFe4S4] Cluster of CO Dehydrogenase Activates CO_2 and NCO^-. *Angew Chem Int Ed Engl* **54**, 8560-8564 (2015).

41. J. H. Jeoung, H. Dobbek, n-Butyl isocyanide oxidation at the [NiFe4S4OH(x)] cluster of CO dehydrogenase. *J Biol Inorg Chem* **17**, 167-173 (2012).

42. A. Ciaccafava *et al.*, When the inhibitor tells more than the substrate: the cyanide-bound state of a carbon monoxide dehydrogenase. *Chem Sci* **7**, 3162-3171 (2016).

43. J. H. Jeoung, H. Dobbek, Structural basis of cyanide inhibition of Ni, Fe-containing carbon monoxide dehydrogenase. *J Am Chem Soc* **131**, 9922-9923 (2009).

44. J. C. Xavier, M. Preiner, W. F. Martin, Something special about CO-dependent CO_2 fixation. *FEBS J* **285**, 4181-4195 (2018).

45. E. J. Kim, J. Feng, M. R. Bramlett, P. A. Lindahl, Evidence for a proton transfer network and a required persulfide-bond-forming cysteine residue in Ni-containing carbon monoxide dehydrogenases. *Biochemistry* **43**, 5728-5734 (2004).

46. V. Svetlitchnyi, C. Peschel, G. Acker, O. Meyer, Two membrane-associated NiFeS-carbon monoxide dehydrogenases from the anaerobic carbon-monoxide-utilizing eubacterium *Carboxydothermus hydrogenoformans*. *J Bacteriol* **183**, 5134-5144 (2001).

47. J. A. Krzycki, J. G. Zeikus, Characterization and purification of carbon monoxide dehydrogenase from *Methanosarcina barkeri*. *J Bacteriol* **158**, 231-237 (1984).

48. K. C. Terlesky, M. J. Nelson, J. G. Ferry, Isolation of an enzyme complex with carbon monoxide dehydrogenase activity containing corrinoid and nickel from acetate-grown *Methanosarcina thermophila*. *J Bacteriol* **168**, 1053-1058 (1986).

49. E. DeMoll, D. A. Grahame, J. M. Harnly, L. Tsai, T. C. Stadtman, Purification and properties of carbon monoxide dehydrogenase from *Methanococcus vannielii. J Bacteriol* **169**, 3916-3920 (1987).

50. J. M. O'Brien, R. H. Wolkin, T. T. Moench, J. B. Morgan, J. G. Zeikus, Association of hydrogen metabolism with unitrophic or mixotrophic growth of *Methanosarcina barkeri* on carbon monoxide. *J Bacteriol* **158**, 373-375 (1984).

51. M. Wu *et al.*, Life in hot carbon monoxide: the complete genome sequence of *Carboxydothermus hydrogenoformans* Z-2901. *PLoS Genet* **1**, e65 (2005).

52. L. Daniels, G. Fuchs, R. K. Thauer, J. G. Zeikus, Carbon monoxide oxidation by methanogenic bacteria. *J Bacteriol* **132**, 118-126 (1977).

53. D. A. Grahame, T. C. Stadtman, Carbon monoxide dehydrogenase from *Methanosarcina barkeri*. Disaggregation, purification, and physicochemical properties of the enzyme. *J Biol Chem* **262**, 3706-3712 (1987).

54. V. Svetlitchnyi *et al.*, A functional Ni-Ni-[4Fe-4S] cluster in the monomeric acetyl-CoA synthase from *Carboxydothermus hydrogenoformans*. *Proc Natl Acad Sci U S A* **101**, 446-451 (2004).

55. Y. R. Dai *et al.*, Acetyl-CoA decarbonylase/synthase complex from *Archaeoglobus fulgidus*. *Arch Microbiol* **169**, 525-529 (1998).

56. P. M. Vignais, B. Billoud, Occurrence, classification, and biological function of hydrogenases: an overview. *Chem Rev* **107**, 4206-4272 (2007).

57. M. Muller, The hydrogenosome. *J Gen Microbiol* **139**, 2879-2889 (1993).

58. J. Appel, R. Schulz, Hydrogen metabolism in organisms with oxygenic photosynthesis: hydrogenases as important regulatory devices for a proper redox poising? *J. Photochem. Photobiol.* **47**, 1-11 (1998).

59. T. Yagi, Y. Higuchi, Studies on hydrogenase. *Proc Jpn Acad Ser B Phys Biol Sci* **89**, 16-33 (2013).

60. C. Greening *et al.*, Genomic and metagenomic surveys of hydrogenase distribution indicate H_2 is a widely utilised energy source for microbial growth and survival. *ISME J* **10**, 761-777 (2016).

61. H. Ogata, W. Lubitz, Y. Higuchi, Structure and function of [NiFe] hydrogenases. *J Biochem* **160**, 251-258 (2016).

62. D. W. Mulder *et al.*, Insights into [FeFe]-hydrogenase structure, mechanism, and maturation. *Structure* **19**, 1038-1052 (2011).

63. S. Shima, R. K. Thauer, A third type of hydrogenase catalyzing H_2 activation. *Chem Rec* **7**, 37-46 (2007).

64. M. W. Adams, The structure and mechanism of iron-hydrogenases. *Biochim Biophys Acta* **1020**, 115-145 (1990).

65. E. C. Hatchikian, M. Bruschi, J. Le Gall, Characterization of the periplasmic hydrogenase from *Desulfovibrio gigas*. *Biochem Biophys Res Commun* **82**, 451-461 (1978).

66. P. P. Liebgott *et al.*, Relating diffusion along the substrate tunnel and oxygen sensitivity in hydrogenase. *Nat Chem Biol* **6**, 63-70 (2010).

67. S. P. Albracht, E. G. Graf, R. K. Thauer, The EPR properties of nickel in hydrogenase from Methanobacterium. *FEBS Lett* **140**, 311-313 (1982).

68. K. Fiebig, B. Friedrich, Purification of the F_{420}-reducing hydrogenase from *Methanosarcina barkeri* (strain Fusaro). *Eur J Biochem* **184**, 79-88 (1989).

69. G. Fauque *et al.*, The three classes of hydrogenases from sulfate-reducing bacteria of the genus Desulfovibrio. *FEMS Microbiol Rev* **4**, 299-344 (1988).

70. E. C. Hatchikian, N. Forget, V. M. Fernandez, R. Williams, R. Cammack, Further characterization of the [Fe]-hydrogenase from *Desulfovibrio desulfuricans* ATCC 7757. *Eur J Biochem* **209**, 357-365 (1992).

71. H. Ogata, W. Lubitz, Y. Higuchi, [NiFe] hydrogenases: structural and spectroscopic studies of the reaction mechanism. *Dalton Trans*, 7577-7587 (2009).

72. R. P. Happe, W. Roseboom, A. J. Pierik, S. P. Albracht, K. A. Bagley, Biological activation of hydrogen. *Nature* **385**, 126 (1997).

73. M. C. Marques *et al.*, The direct role of selenocysteine in [NiFeSe] hydrogenase maturation and catalysis. *Nat Chem Biol* **13**, 544-550 (2017).

74. M. C. Marques, R. Coelho, A. L. De Lacey, I. A. Pereira, P. M. Matias, The three-dimensional structure of [NiFeSe] hydrogenase from *Desulfovibrio vulgaris* Hildenborough: a hydrogenase without a bridging ligand in the active site in its oxidised, "as-isolated" state. *J Mol Biol* **396**, 893-907 (2010).

75. H. Ogata *et al.*, Activation process of [NiFe] hydrogenase elucidated by high-resolution X-ray analyses: conversion of the ready to the unready state. *Structure* **13**, 1635-1642 (2005).

76. L. Bowman *et al.*, How the structure of the large subunit controls function in an oxygen-tolerant [NiFe]-hydrogenase. *Biochem J* **458**, 449-458 (2014).

77. S. Vitt *et al.*, The F(4)(2)(0)-reducing [NiFe]-hydrogenase complex from *Methanothermobacter marburgensis*, the first X-ray structure of a group 3 family member. *J Mol Biol* **426**, 2813-2826 (2014).

78. T. Burgdorf *et al.*, [NiFe]-hydrogenases of *Ralstonia eutropha* H16: modular enzymes for oxygen-tolerant biological hydrogen oxidation. *J Mol Microbiol Biotechnol* **10**, 181-196 (2005).

79. T. Buhrke, O. Lenz, N. Krauss, B. Friedrich, Oxygen tolerance of the H_2-sensing [NiFe] hydrogenase from *Ralstonia eutropha* H16 is based on limited access of oxygen to the active site. *J Biol Chem* **280**, 23791-23796 (2005).

80. M. M. Roessler, R. M. Evans, R. A. Davies, J. Harmer, F. A. Armstrong, EPR spectroscopic studies of the Fe-S clusters in the O_2-tolerant [NiFe]-hydrogenase Hyd-1 from *Escherichia coli* and characterization of the unique [4Fe-3S] cluster by HYSCORE. *J Am Chem Soc* **134**, 15581-15594 (2012).

81. A. Adamska *et al.*, Identification and characterization of the "super-reduced" state of the H-cluster in [FeFe] hydrogenase: a new building block for the catalytic cycle? *Angew Chem Int Ed Engl* **51**, 11458-11462 (2012).

82. S. T. Stripp *et al.*, How oxygen attacks [FeFe] hydrogenases from photosynthetic organisms. *Proc Natl Acad Sci U S A* **106**, 17331-17336 (2009).

83. C. Afting, E. Kremmer, C. Brucker, A. Hochheimer, R. K. Thauer, Regulation of the synthesis of H_2-forming methylenetetrahydromethanopterin dehydrogenase (Hmd) and of HmdII and HmdIII in *Methanothermobacter marburgensis*. *Arch Microbiol* **174**, 225-232 (2000).

84. R. K. Thauer *et al.*, Hydrogenases from methanogenic archaea, nickel, a novel cofactor, and H_2 storage. *Annu Rev Biochem* **79**, 507-536 (2010).

85. Y. Nicolet, C. Piras, P. Legrand, C. E. Hatchikian, J. C. Fontecilla-Camps, *Desulfovibrio desulfuricans* iron hydrogenase: the structure shows unusual coordination to an active site Fe binuclear center. *Structure* **7**, 13-23 (1999).

86. T. Hiromoto, E. Warkentin, J. Moll, U. Ermler, S. Shima, The crystal structure of an [Fe]-hydrogenase-substrate complex reveals the framework for H_2 activation. *Angew Chem Int Ed Engl* **48**, 6457-6460 (2009).

87. J. Kalms *et al.*, Krypton derivatization of an O_2-tolerant membrane-bound [NiFe] hydrogenase reveals a hydrophobic tunnel network for gas transport. *Angew Chem Int Ed Engl* **55**, 5586-5590 (2016).

88. Y. Higuchi, T. Yagi, N. Yasuoka, Unusual ligand structure in Ni–Fe active center and an additional Mg site in hydrogenase revealed by high resolution X-ray structure analysis. *Structure* **5**, 1671-1680 (1997).

89. H. Ogata, K. Nishikawa, W. Lubitz, Hydrogens detected by subatomic resolution protein crystallography in a [NiFe] hydrogenase. *Nature* **520**, 571-574 (2015).

90. Y. Montet *et al.*, Gas access to the active site of Ni-Fe hydrogenases probed by X-ray crystallography and molecular dynamics. *Nat Struct Biol* **4**, 523-526 (1997).

91. Y. Shomura *et al.*, Structural basis of the redox switches in the NAD^+-reducing soluble [NiFe]-hydrogenase. *Science* **357**, 928-932 (2017).

92. T. Wagner, J. Koch, U. Ermler, S. Shima, Methanogenic heterodisulfide reductase (HdrABC-MvhAGD) uses two noncubane [4Fe-4S] clusters for reduction. *Science* **357**, 699-703 (2017).

93. A. Volbeda *et al.*, Structural differences between the ready and unready oxidized states of [NiFe] hydrogenases. *J Biol Inorg Chem* **10**, 239-249 (2005).

94. A. Volbeda *et al.*, Crystallographic studies of [NiFe]-hydrogenase mutants: towards consensus structures for the elusive unready oxidized states. *J Biol Inorg Chem* **20**, 11-22 (2015).

95. Y. Higuchi, T. Yagi, Liberation of hydrogen sulfide during the catalytic action of *Desulfovibrio hydrogenase* under the atmosphere of hydrogen. *Biochem Biophys Res Commun* **255**, 295-299 (1999).

96. Y. Higuchi, H. Ogata, K. Miki, N. Yasuoka, T. Yagi, Removal of the bridging ligand atom at the Ni-Fe active site of [NiFe] hydrogenase upon reduction with H_2, as revealed by X-ray structure analysis at 1.4 A resolution. *Structure* **7**, 549-556 (1999).

97. H. Osuka *et al.*, Photosensitivity of the Ni-A state of [NiFe] hydrogenase from *Desulfovibrio vulgaris* Miyazaki F with visible light. *Biochem Biophys Res Commun* **430**, 284-288 (2013).

98. M. van Gastel *et al.*, A single-crystal ENDOR and density functional theory study of the oxidized states of the [NiFe] hydrogenase from *Desulfovibrio vulgaris* Miyazaki F. *J Biol Inorg Chem* **11**, 41-51 (2006).

99. A. Abou Hamdan *et al.*, O_2-independent formation of the inactive states of NiFe hydrogenase. *Nat Chem Biol* **9**, 15-17 (2013).

100. B. Bleijlevens *et al.*, The activation of the [NiFe]-hydrogenase from *Allochromatium vinosum*. An infrared spectro-electrochemical study. *J Biol Inorg Chem* **9**, 743-752 (2004).

101. F. Roncaroli *et al.*, Cofactor composition and function of a H_2-sensing regulatory hydrogenase as revealed by Mossbauer and EPR spectroscopy. *Chem Sci* **6**, 4495-4507 (2015).

102. M. Horch *et al.*, Resonance Raman spectroscopy on [NiFe] hydrogenase provides structural insights into catalytic intermediates and reactions. *J Am Chem Soc* **136**, 9870-9873 (2014).

103. H. Ogata *et al.*, Structural studies of the carbon monoxide complex of [NiFe]hydrogenase from *Desulfovibrio vulgaris* Miyazaki F: suggestion for the initial activation site for dihydrogen. *J Am Chem Soc* **124**, 11628-11635 (2002).

104. E. Siebert *et al.*, Resonance Raman spectroscopy as a tool to monitor the active site of hydrogenases. *Angew Chem Int Ed Engl* **52**, 5162-5165 (2013).

105. H. Tai, K. Nishikawa, M. Suzuki, Y. Higuchi, S. Hirota, Control of the transition between Ni-C and Ni_a-SI states by the redox state of the proximal Fe-S cluster in the catalytic cycle of [NiFe] hydrogenase. *Angew Chem Int Ed Engl* **53**, 13817-13820 (2014).

106. U. K. Laemmli, Cleavage of structural proteins during the assembly of the head of bacteriophage T4. *Nature* **227**, 680-685 (1970).

107. U. Mueller *et al.*, The macromolecular crystallography beamlines at BESSY II of the Helmholtz-Zentrum Berlin: Current status and perspectives. *The European Physical Journal Plus* **130:140**, (2015).

108. W. Kabsch, Xds. *Acta Crystallogr D Biol Crystallogr* **66**, 125-132 (2010).

109. P. H. Zwart *et al.*, Automated structure solution with the PHENIX suite. *Methods Mol Biol* **426**, 419-435 (2008).

110. P. Emsley, K. Cowtan, Coot: model-building tools for molecular graphics. *Acta Crystallogr D Biol Crystallogr* **60**, 2126-2132 (2004).

111. P. D. Adams *et al.*, PHENIX: a comprehensive Python-based system for macromolecular structure solution. *Acta Crystallogr D Biol Crystallogr* **66**, 213-221 (2010).

112. G. N. Murshudov *et al.*, REFMAC5 for the refinement of macromolecular crystal structures. *Acta Crystallogr D Biol Crystallogr* **67**, 355-367 (2011).

113. E. F. Pettersen *et al.*, UCSF Chimera: a visualization system for exploratory research and analysis. *J Comput Chem* **25**, 1605-1612 (2004).

114. C. Suloway *et al.*, Automated molecular microscopy: the new Leginon system. *J Struct Biol* **151**, 41-60 (2005).

115. S. H. Scheres, RELION: implementation of a Bayesian approach to cryo-EM structure determination. *J Struct Biol* **180**, 519-530 (2012).

116. M. van Heel, G. Harauz, E. V. Orlova, R. Schmidt, M. Schatz, A new generation of the IMAGIC image processing system. *J Struct Biol* **116**, 17-24 (1996).

117. G. Tang *et al.*, EMAN2: an extensible image processing suite for electron microscopy. *J Struct Biol* **157**, 38-46 (2007).

118. J. A. Mindell, N. Grigorieff, Accurate determination of local defocus and specimen tilt in electron microscopy. *J Struct Biol* **142**, 334-347 (2003).

119. X. Li *et al.*, Electron counting and beam-induced motion correction enable near-atomic-resolution single-particle cryo-EM. *Nat Methods* **10**, 584-590 (2013).

120. S. H. Scheres, Semi-automated selection of cryo-EM particles in RELION-1.3. *J Struct Biol* **189**, 114-122 (2015).

121. H. Hippe, D. Caspari, K. Fiebig, G. Gottschalk, Utilization of trimethylamine and other N-methyl compounds for growth and methane formation by *Methanosarcina barkeri*. *Proc. Natl. Acad. Sci. USA* **76**, 494-498 (1978).

122. Q. Lin *et al.*, Different substrate regimes determine transcriptional profiles and gene co-expression in *Methanosarcina barkeri* (DSM 800). *Appl Microbiol Biotechnol* **101**, 7303-7316 (2017).

123. T. J. Hutten, H. C. Bongaerts, C. van der Drift, G. D. Vogels, Acetate, methanol and carbon dioxide as substrates for growth of Methanosarcina barkeri. *Antonie Van Leeuwenhoek* **46**, 601-610 (1980).

124. R. A. Mah, M. R. Smith, L. Baresi, Studies on an acetate-fermenting strain of *Methanosarcina*. *Appl Environ Microbiol* **35**, 1174-1184 (1978).

125. B. Sander, M. M. Golas, Visualization of bionanostructures using transmission electron microscopical techniques. *Microsc Res Tech* **74**, 642-663 (2011).

126. S. De Carlo, J. R. Harris, Negative staining and cryo-negative staining of macromolecules and viruses for TEM. *Micron* **42**, 117-131 (2011).

127. J. Dubochet *et al.*, Cryo-electron microscopy of vitrified specimens. *Q Rev Biophys* **21**, 129-228 (1988).

128. R. M. Glaeser, B. G. Han, Opinion: hazards faced by macromolecules when confined to thin aqueous films. *Biophys Rep* **3**, 1-7 (2017).

129. R. M. Oliver, Negative stain electron microscopy of protein macromolecules. *Methods Enzymol* **27**, 616-672 (1973).

130. S. Woeste, P. Demchick, New version of the negative stain. *Appl Environ Microbiol* **57**, 1858-1859 (1991).

131. J. E. Mellema, E. F. van Bruggen, An assessment of negative staining in the electron microscopy of low molecular weight proteins. *J Mol Biol* **31**, 75-82 (1968).

132. J. R. Harris, Transmission electron microscopy in molecular structural biology: A historical survey. *Arch Biochem Biophys* **581**, 3-18 (2015).

133. J. Lepault, F. P. Booy, J. Dubochet, Electron microscopy of frozen biological suspensions. *J Microsc* **129**, 89-102 (1983).

134. A. J. Noble *et al.*, Routine single particle cryo-EM sample and grid characterization by tomography. *Elife* **7**, (2018).

135. L. A. Baker, J. L. Rubinstein, Radiation damage in electron cryomicroscopy. *Methods Enzymol* **481**, 371-388 (2010).

136. S. A. Arnold *et al.*, Blotting-free and lossless cryo-electron microscopy grid preparation from nanoliter-sized protein samples and single-cell extracts. *J Struct Biol* **197**, 220-226 (2017).

137. B. Kastner *et al.*, GraFix: sample preparation for single-particle electron cryomicroscopy. *Nat Methods* **5**, 53-55 (2008).

138. J. Frank *et al.*, A model of protein synthesis based on cryo-electron microscopy of the *E. coli* ribosome. *Nature* **376**, 441-444 (1995).

139. A. Doerr, Single-particle cryo-electron microscopy. *Nat Methods* **13**, 23 (2016).

140. J. Frank, Single-particle reconstruction of biological macromolecules in electron microscopy--30 years. *Q Rev Biophys* **42**, 139-158 (2009).

141. M. Van Heel, Angular reconstitution: a posteriori assignment of projection directions for 3D reconstruction. *Ultramicroscopy* **21**, 111-123 (1987).

142. P. A. Penczek, R. A. Grassucci, J. Frank, The ribosome at improved resolution: new techniques for merging and orientation refinement in 3D cryo-electron microscopy of biological particles. *Ultramicroscopy* **53**, 251-270 (1994).

143. H. Y. Liao, J. Frank, Definition and estimation of resolution in single-particle reconstructions. *Structure* **18**, 768-775 (2010).

144. K. Naydenova, C. J. Russo, Measuring the effects of particle orientation to improve the efficiency of electron cryomicroscopy. *Nat Commun* **8**, 629 (2017).

145. M. Ohi, Y. Li, Y. Cheng, T. Walz, Negative staining and image classification - powerful tools in modern electron microscopy. *Biol Proced Online* **6**, 23-34 (2004).

146. E. Nogales, S. H. Scheres, Cryo-EM: A unique tool for the visualization of macromolecular complexity. *Mol Cell* **58**, 677-689 (2015).

147. F. J. Sigworth, A maximum-likelihood approach to single-particle image refinement. *J Struct Biol* **122**, 328-339 (1998).

148. R. Langer, J. Frank, A. Feltynowski, W. Hoppe, Application of the image subtraction method to study structural changes in thin carbon films. *Berichte der Bunsen-Gesellschaft für Physikalische Chemie* **74**, 1120-1126 (1970).

149. H. E. White, A. Ignatiou, D. K. Clare, E. V. Orlova, Structural study of heterogeneous biological samples by cryoelectron microscopy and image processing. *Biomed Res Int* **2017**, 1032432 (2017).

150. J. Loerke, J. Giesebrecht, C. M. Spahn, Multiparticle cryo-EM of ribosomes. *Methods Enzymol* **483**, 161-177 (2010).

151. H. Y. Liao, J. Frank, Classification by bootstrapping in single particle methods. *Proc IEEE Int Symp Biomed Imaging* **2010**, 169-172 (2010).

152. R. Henderson, Avoiding the pitfalls of single particle cryo-electron microscopy: Einstein from noise. *Proc Natl Acad Sci U S A* **110**, 18037-18041 (2013).

153. M. Radermacher, T. Wagenknecht, A. Verschoor, J. Frank, Three-dimensional reconstruction from a single-exposure, random conical tilt series applied to the 50S ribosomal subunit of *Escherichia coli*. *J Microsc* **146**, 113-136 (1987).

154. A. E. Leschziner, E. Nogales, The orthogonal tilt reconstruction method: an approach to generating single-class volumes with no missing cone for ab initio reconstruction of asymmetric particles. *J Struct Biol* **153**, 284-299 (2006).

155. V. Lucic, F. Forster, W. Baumeister, Structural studies by electron tomography: from cells to molecules. *Annu Rev Biochem* **74**, 833-865 (2005).

156. T. Svetlitchnaia, V. Svetlitchnyi, O. Meyer, H. Dobbek, Structural insights into methyltransfer reactions of a corrinoid iron-sulfur protein involved in acetyl-CoA synthesis. *Proc Natl Acad Sci U S A* **103**, 14331-14336 (2006).

157. T. I. Doukov, L. C. Blasiak, J. Seravalli, S. W. Ragsdale, C. L. Drennan, Xenon in and at the end of the tunnel of bifunctional carbon monoxide dehydrogenase/acetyl-CoA synthase. *Biochemistry* **47**, 3474-3483 (2008).

158. C. Darnault *et al.*, Ni-Zn-[Fe4-S4] and Ni-Ni-[Fe4-S4] clusters in closed and open subunits of acetyl-CoA synthase/carbon monoxide dehydrogenase. *Nat Struct Biol* **10**, 271-279 (2003).

159. H. P. Klenk *et al.*, The complete genome sequence of the hyperthermophilic, sulphate-reducing archaeon *Archaeoglobus fulgidus*. *Nature* **390**, 364-370 (1997).

160. M. Can, F. A. Armstrong, S. W. Ragsdale, Structure, function, and mechanism of the nickel metalloenzymes, CO dehydrogenase, and acetyl-CoA synthase. *Chem Rev* **114**, 4149-4174 (2014).

161. S. Gencic, E. C. Duin, D. A. Grahame, Tight coupling of partial reactions in the acetyl-CoA decarbonylase/synthase (ACDS) multienzyme complex from *Methanosarcina thermophila*: acetyl C-C bond fragmentation at the a cluster promoted by protein conformational changes. *J Biol Chem* **285**, 15450-15463 (2010).

162. S. L. Mayo, W. R. Ellis, Jr., R. J. Crutchley, H. B. Gray, Long-range electron transfer in heme proteins. *Science* **233**, 948-952 (1986).

163. C. C. Moser, J. M. Keske, K. Warncke, R. S. Farid, P. L. Dutton, Nature of biological electron transfer. *Nature* **355**, 796-802 (1992).

164. Y. Kung, T. I. Doukov, J. Seravalli, S. W. Ragsdale, C. L. Drennan, Crystallographic snapshots of cyanide- and water-bound C-clusters from bifunctional carbon monoxide dehydrogenase/acetyl-CoA synthase. *Biochemistry* **48**, 7432-7440 (2009).

165. F. Sievers *et al.*, Fast, scalable generation of high-quality protein multiple sequence alignments using Clustal Omega. *Mol Syst Biol* **7**, 539 (2011).

166. J. A. Gerlt *et al.*, Enzyme Function Initiative-Enzyme Similarity Tool (EFI-EST): A web tool for generating protein sequence similarity networks. *Biochim Biophys Acta* **1854**, 1019-1037 (2015).

167. M. E. Smoot, K. Ono, J. Ruscheinski, P. L. Wang, T. Ideker, Cytoscape 2.8: new features for data integration and network visualization. *Bioinformatics* **27**, 431-432 (2011).

168. B. C. Stover, K. F. Muller, TreeGraph 2: combining and visualizing evidence from different phylogenetic analyses. *BMC Bioinformatics* **11**, 7 (2010).

169. K. Raymann, C. Brochier-Armanet, S. Gribaldo, The two-domain tree of life is linked to a new root for the Archaea. *Proc Natl Acad Sci U S A* **112**, 6670-6675 (2015).

170. A. J. Probst *et al.*, Biology of a widespread uncultivated archaeon that contributes to carbon fixation in the subsurface. *Nat Commun* **5**, 5497 (2014).

171. S. S. Pang, R. G. Duggleby, R. L. Schowen, L. W. Guddat, The crystal structures of Klebsiella pneumoniae acetolactate synthase with enzyme-bound cofactor and with an unusual intermediate. *J Biol Chem* **279**, 2242-2253 (2004).

172. T. C. Umland, E. C. Wolff, M. H. Park, D. R. Davies, A new crystal structure of deoxyhypusine synthase reveals the configuration of the active enzyme and of an enzyme NAD^+-inhibitor ternary complex. *J Biol Chem* **279**, 28697-28705 (2004).

173. M. S. Cosgrove *et al.*, The structural basis of sirtuin substrate affinity. *Biochemistry* **45**, 7511-7521 (2006).

174. J. L. Craft, P. W. Ludden, T. C. Brunold, Spectroscopic studies of nickel-deficient carbon monoxide dehydrogenase from *Rhodospirillum rubrum*: nature of the iron-sulfur clusters. *Biochemistry* **41**, 1681-1688 (2002).

175. T. Shanmugasundaram, H. G. Wood, Interaction of ferredoxin with carbon monoxide dehydrogenase from *Clostridium thermoaceticum*. *J Biol Chem* **267**, 897-900 (1992).

176. G. Kulkarni, D. M. Kridelbaugh, A. M. Guss, W. W. Metcalf, Hydrogen is a preferred intermediate in the energy-conserving electron transport chain of *Methanosarcina barkeri*. *Proc Natl Acad Sci U S A* **106**, 15915-15920 (2009).

177. S. F. Baron, J. G. Ferry, Purification and properties of the membrane-associated coenzyme F_{420}-reducing hydrogenase from *Methanobacterium formicicum*. *JOURNAL OF BACTERIOLOGY* **171**, 3846-3853 (1989).

178. J. A. Fox, D. J. Livingston, W. H. Orme-Johnson, C. T. Walsh, 8-Hydroxy-5-deazaflavin-reducing hydrogenase from *Methanobacterium thermoautotrophicum*: 1. Purification and characterization. *Biochemistry* **26**, 4219-4227 (1987).

179. E. Muth, E. Morschel, A. Klein, Purification and characterization of an 8-hydroxy-5-deazaflavin-reducing hydrogenase from the archaebacterium *Methanococcus voltae*. *Eur J Biochem* **169**, 571-577 (1987).

180. N. N. Shah, D. S. Clark, Partial purification and characterization of two hydrogenases from the extreme thermophile *Methanococcus jannaschii*. *Appllied and Environmental Microbiology* **56**, 858-863 (1990).

181. R. Michel, C. Massanz, S. Kostka, M. Richter, K. Fiebig, Biochemical characterization of the 8-hydroxy-5-deazaflavin-reactive hydrogenase from *Methanosarcina barkeri* Fusaro. *Eur J Biochem* **233**, 727-735 (1995).

182. P. A. Karplus, K. Diederichs, Linking crystallographic model and data quality. *Science* **336**, 1030-1033 (2012).

183. M. Vaupel, R. K. Thauer, Two F_{420}-reducing hydrogenases in *Methanosarcina barkeri*. *Arch Microbiol* **169**, 201-205 (1998).

184. Y. Higuchi, T. Yagi, N. Yasuoka, Unusual ligand structure in Ni-Fe active center and an additional Mg site in hydrogenase revealed by high resolution X-ray structure analysis. *Structure* **5**, 1671-1680 (1997).

185. A. Volbeda *et al.*, Crystal structure of the nickel-iron hydrogenase from *Desulfovibrio gigas*. *Nature* **373**, 580-587 (1995).

186. S. Halboth, A. Klein, *Methanococcus voltae* harbors four gene clusters potentially encoding two [NiFe] and two [NiFeSe] hydrogenases, each of the cofactor F_{420}-reducing or F_{420}-non-reducing types. *Mol Gen Genet* **233**, 217-224 (1992).

187. C. J. Bult *et al.*, Complete genome sequence of the methanogenic archaeon, *Methanococcus jannaschii*. *Science* **273**, 1058-1073 (1996).

188. A. M. Guss, G. Kulkarni, W. W. Metcalf, Differences in hydrogenase gene expression between *Methanosarcina acetivorans* and *Methanosarcina barkeri*. *J Bacteriol* **191**, 2826-2833 (2009).

189. M. C. Marques, R. Coelho, I. A. C. Pereira, P. M. Matias, Redox state-dependent changes in the crystal structure of [NiFeSe] hydrogenase from *Desulfovibrio vulgaris* Hildenborough. *Int.J.Hydrogen Energy* **38**, 8664-8682 (2013).

190. F. S. Jacobson, L. Daniels, J. A. Fox, C. T. Walsh, W. H. Orme-Johnson, Purification and properties of an 8-hydroxy-5-deazaflavin-reducing hydrogenase from *Methanobacterium thermoautotrophicum*. *J Biol Chem* **257**, 3385-3388 (1982).

191. D. J. Livingston, J. A. Fox, W. H. Orme-Johnson, C. T. Walsh, 8-Hydroxy-5-deazaflavin-reducing hydrogenase from *Methanobacterium thermoautotrophicum*: 2. Kinetic and hydrogen-transfer studies. *Biochemistry* **26**, 4228-4237 (1987).

192. J. P. M. Schelvis, D. Pun, N. Goyal, O. Sokolova, Resonance Raman spectra of the neutral and anionicradical semiquinones of flavin adenine dinucleotide inglucose oxidase revisited. *Journal of Raman Spectroscopy* **37**, 822–829 (2006).

193. E. Garcin *et al.*, The crystal structure of a reduced [NiFeSe] hydrogenase provides an image of the activated catalytic center. *Structure* **7**, 557-566 (1999).

194. H. Ogata, P. Kellers, W. Lubitz, The crystal structure of the [NiFe] hydrogenase from the photosynthetic bacterium *Allochromatium vinosum*: characterization of the oxidized enzyme (Ni-A state). *J Mol Biol* **402**, 428-444 (2010).

195. A. L. De Lacey, V. M. Fernandez, M. Rousset, R. Cammack, Activation and inactivation of hydrogenase function and the catalytic cycle: spectroelectrochemical studies. *Chem Rev* **107**, 4304-4330 (2007).

196. E. Siebert *et al.*, Resonance Raman spectroscopic analysis of the [NiFe] active site and the proximal [4Fe-3S] cluster of an O_2-tolerant membrane-bound hydrogenase in the crystalline state. *J Phys Chem B* **119**, 13785-13796 (2015).

197. M. E. Pandelia, H. Ogata, L. J. Currell, M. Flores, W. Lubitz, Inhibition of the [NiFe] hydrogenase from *Desulfovibrio vulgaris* Miyazaki F by carbon monoxide: an FTIR and EPR spectroscopic study. *Biochim Biophys Acta* **1797**, 304-313 (2010).

198. K. A. Bagley *et al.*, Infrared studies on the interaction of carbon monoxide with divalent nickel in hydrogenase from *Chromatium vinosum*. *Biochemistry* **33**, 9229-9236 (1994).

6 LIST OF FIGURES

7 LIST OF TABLES

8 DECLARATION

Hier miterkläre ich, dass ich die vorliegende Arbeit selbstständig verfasst und keine weiteren als die angegebenen Hilfsmittel verwendet habe.

I hereby declare that I have prepared this work independently, using only references and resources, which are marked as such.

Berlin, den 10.04.2019 Yulia Ilina